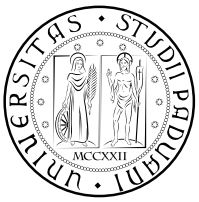

UNIVERSITÀ DEGLI STUDI DI PADOVA

Sede Amministrativa: Università degli Studi di Padova

Dipartimento di Ingegneria Idraulica, Marittima, Ambientale e Geotecnica

SCUOLA DI DOTTORATO DI RICERCA IN
SCIENZE DELL'INGEGNERIA CIVILE E AMBIENTALE

CICLO XXV

TRANSPORT PROCESSES AND OPTIMIZATION STRATEGIES IN WETLAND DESIGN

Direttore della Scuola: Ch.mo. Prof. Stefano Lanzoni

Supervisore: Ch.mo. Prof. Andrea Marion

Co-supervisore: Ing. Andrea Bottacin Busolin

Dottorando: Tommaso Musner

31 Gennaio 2013

Sommario

Le zone di transizione tra entroterra e mare costituiscono una porzione di territorio molto importante dal punto di vista ambientale e naturalistico. Esse rappresentano un naturale filtro per tutte quelle specie chimiche che sono prodotte da fonti di inquinamento diffuse (dilavamento di suoli agricoli) o occulte (scarichi non collettati o irregolari) che possono creare, se non opportunamente trattate, problemi di eutrofizzazione e di qualità delle acque lungo le coste. I tradizionali metodi di depurazione si rivelano poco efficaci nel trattare questo tipo di effluenti, per le grandi portate da gestire e per le relativamente basse concentrazioni di inquinanti. Risulta importante quindi, nell'impossibilità di impiegare i tradizionali impianti di depurazione, comprendere le dinamiche di trasporto negli ambienti naturali (fiumi e aree umide) e i meccanismi di rimozione degli inquinanti in tali zone, in modo da poterle utilizzare per riassorbire, in modo sostenibile e naturale, il carico di inquinanti che altrimenti raggiungerebbe direttamente le coste. A questo scopo é necessario focalizzare l'attenzione sui processi di ritenzione e sulla formulazione di appropriati strumenti modellistici che consentano ai tecnici e ai modellisti una comprensione sufficientemente ampia dei fenomeni e forniscano loro degli strumenti pratici che aiutino nella gestione e riprogettazione di queste aree tampone.

Nel Capitolo 1 viene analizzato il ruolo di differenti processi di trasporto focalizzando l'attenzione su diverse scale spaziali e temporali di analisi e descrivendo i principali approcci modellistici utilizzati per trattare ciascun fenomeno. E' evi-

denziato il contributo di ciascun termine al bilancio di massa e sono prese in considerazione le chiusure modellistiche più classiche oggi adottate.

Nel Capitolo 2 si analizzano le caratteristiche dei processi di ritenzione in tre diversi corsi d'acqua mettendo in relazione le diverse chiusure modellistiche adottate in funzione delle caratteristiche planimetriche degli alvei, della loro composizione vegetazionale e delle caratteristiche di permeabilità del fondo. L'analisi é eseguita utilizzando il modello di trasporto monodimensionale STIR (Solute Transport In Rivers) che si presta a descrivere le curve di concentrazione implementando una vasta gamma di fenomeni di ritenzione a diverse scale temporali, descritte da specifiche distribuzioni dei tempi di residenza del soluto in ciascun comparto di ritenzione. L'accordo dei dati sperimentali con le curve di concentrazione mostra come si possa, tramite analisi inversa, caratterizzare un fiume dal punto di vista della ritenzione.

Il Capitolo 3 prende in considerazione un'area umida bidimensionale di cui si risolvono, con un approccio modellistico alle acque basse, l'idrodinamica e il trasporto di massa. Una opportuna procedura di analisi dei risultati numerici é utilizzata per determinare le distribuzioni dei tempi di residenza dell'area umida in funzione di una particolare distribuzione di vegetazione che riproduce un canale principale delimitato da due zone laterali a maggiore densità di vegetazione. A diversi rapporti di densità corrisponde una specifica forma della distribuzione che presenta, al di sotto di uno specifico valore di soglia, una evidente bimodalità. Per rappresentare opportunamente tale fenomeno, comune negli ambienti naturali, con un approccio modellistico mono-dimensionale di più semplice utilizzo, é proposta in questo capitolo, una nuova versione del modello STIR denominata STIR-DTD.

Il Capitolo 4 presenta un approccio innovativo di ottimizzazione alla progettazione di un'area umida. La risoluzione numerica di un modello bidimensionale alle acque basse tramite il modello TELEMAC2D é integrata infatti con un algo-

ritmo evolutivo di ottimizzazione. Allo stadio iniziale dell'evoluzione, é definita, in modo casuale, una popolazione di individui (ciascun individuo rappresenta una specifica distribuzione di zone vegetate) di cui il modello valuta l'efficienza depurativa. A partire dal livello di efficienza depurativa dimostrata da ciascuna distribuzione, l'algoritmo evolutivo, tramite specifici operatori genetici che mimano i processi di selezione naturali, evolve la popolazione verso la distribuzione di vegetazione che massimizza l'abbattimento di inquinanti. I test effettuati mostrano come la distribuzione ottimale evolva verso configurazioni che tendono a coprire tutta l'area vegetata disponibile o, qualora questa sia fissata, a prolungare il più possibile i percorsi di flusso all'interno delle aree vegetate.

Il Capitolo 5 riporta i risultati di una prima analisi eseguita su campi random di vegetazione, descritti da una opportuna funzione densità di probabilità spaziale (Gaussiana). La risoluzione tramite un modello bidimensionale accoppiato ad uno di trasporto e decadimento mostra come l'efficienza depurativa e la portata siano correlabili con i parametri (densità media, varianza e lunghezza di correlazione) che caratterizzano la particolare distribuzione statistica di vegetazione adottata.

Abstract

Transitional areas, between inland and coastal environments, represent an important habitat for their environmental and natural value. They act as a natural buffer for all those chemicals which are produced by diffused sources of pollutants (run-off rain water from agriculture) or from hidden sources (sewers not connected to a wastewater treatment plant). Pollutants produced by this type of sources can lead, if not conveniently treated, to eutrophication and to other water quality problems along coastal areas. Traditional wastewater treatment methods appear to be not effective in these conditions because of the big volumes of water and the relatively low concentration of dissolved pollutants to be treated. Since traditional wastewater treatment plants can not be used, it becomes important to better understand transport phenomena in transitional environments (rivers and wetlands) and all the removal processes in such zones in order to manage them to treat all the chemicals before they arrive to the coastal areas. Particular attention must be therefore stressed on retention processes and on the formulation of predictive models which allow scientists and engineers to better manage and design these buffer areas.

In Chapter 1, the role of different transport processes is analyzed focusing the attention on different spatial and temporal scales. Principal modeling approaches are discussed underlining the role of each term on the mass balance equation and the most classical model closures are described in this chapter.

In Chapter 2, retention characteristics of three different rivers are analyzed,

relating different model closures with planimetric features of the rivers, their vegetational cover and bottom permeability. The analysis is carried on using STIR (Solute Transport In Rivers) model, a one-dimensional solute transport model that describes concentration breakthrough curves implementing a wide set of retention phenomena characterized by different time scales, represented by a specific residence time distribution in each retention domain. Comparison of modeling results and experimental data shows the capability of the model to characterize, with an inverse analysis, retention processes that occur in a river.

In Chapter 3 a two-dimensional schematic wetland is studied with a numerical model that solves, with a shallow water approach, hydrodynamic and mass transport equations. A specific processing of the numerical results is used to determine numerical residence time distributions of the wetland as a function of a particular vegetation distribution that reproduces a central channel delimited by two lateral, more densely vegetated, banks. To each different density ratio it corresponds a specific shape of the residence time distribution, that present a clear bimodality below a critical value. To model this specific phenomenon, typical in natural environments, a simple and a more easy to use one-dimensional model approach is implemented in the former STIR model. The new version is called STIR-DTD.

In Chapter 4 a new innovative optimization approach to wetland design is defined. Numerical solution of a two-dimensional shallow water model using the open-source suite TELEMAC2D, is integrated with an evolutionary optimization algorithm. At the initial stage of the evolution strategy, the removal efficiency of a random population of individuals (each individual represents a specific distribution of vegetated patches over the wetland domain) is evaluated numerically solving a shallow water hydrodynamic model coupled with a solute transport model. Once the removal efficiency is known, the evolutionary algorithm, using a wide range of selection operators that mimic natural evolution, evolve the

initial population to an individual that maximizes the pollutant mass removal. Performed tests show how the optimized distribution tends to cover the maximum wetland available area or, if a maximum vegetated area is kept fixed, how the distribution tends to lengthen the flow paths between the inlet and the outlet section of the wetland.

Chapter 5 shows results of a preliminary analysis on the removal efficiency of randomly distributed vegetation characterized by a Gaussian spatial probability density function. Vegetation density is treated as a random variable characterized by a mean, a variance and an homogeneous correlation length. The effect of each distribution on the removal efficiency is numerically evaluated by a coupled hydrodynamic and solute transport that accounts for the pollutant decay. Results show how removal efficiency is correlated with the statistical parameters of the space probability density function used to generate the random filed.

Contents

Chapter 1

Physical transport processes in natural environments

1.1 Introduction

This chapter presents an overview of the transport processes in natural environments. Main equations are derived and described showing the most common model closures used to treat spatial and temporal irregularities of the main variables with a particular attention on mixing processes over two dimensional domains. At the end of the chapter, a brief description of transient storage processes and modeling of reactive solutes is presented.

1.2 Combined advection-diffusion processes

In transport processes, the quantity of interest is the mass of a dissolved substance subject to advection and diffusion. Advection is the process by which a conserved quantity is transported in a fluid in motion whereas diffusion is the process by which matter is transported from one part of the domain to another as a result of random molecular motions. Fluid motion is characterized by the velocity vector field $\mathbf{u} = (u, v, w)$ and the mass of a dissolved substance per unit volume is described by a concentration c [ML^{-3}]. The mass flux, that account for both diffusion and advection processes, can be written as:

$$\mathbf{\Phi} = \mathbf{u}c - D_m \nabla c, \tag{1.1}$$

First term $\mathbf{u}c$ represents the convective component of the mass flux and the second term $-D_m \nabla c$ represents the diffusive component written as proposed by *Fick* (1855). Fick's approach describes the net mass flux of solute as the product of the concentration gradient and the molecular diffusion coefficient D_m $[\mathrm{L}^2\,\mathrm{T}^{-1}]$. Negative sign accounts for the direction of the flux from higher concentrations to lower concentrations. To note that molecular diffusion does not exist as a physical phenomenon but represents only an ensamble behavior of solute particles. Indeed, each single particle does not feel the effect of the concentration gradient but moves following the Brownian motion: only at a larger scale small Brownian movements produce, under probabilistic point of view, a mass transport from zones characterized by high concentrations to zones characterized by low concentrations of solute.

The net flux $\mathbf{\Phi}$ can be coupled with the mass balance equation to model diffusion and transport processes of solutes in fluids. The mass balance equation can be written as:

$$\frac{\partial c}{\partial t} = -\nabla \cdot (c\mathbf{u} - D_m \nabla c). \tag{1.2}$$

Molecular diffusion coefficient D_m $[\mathrm{L}^2\,\mathrm{T}^{-1}]$ can be regarded as a constant and depends on solute and solvent characteristics. In water environments, molecular diffusion is of the order of $10^{-8} \div 10^{-10}\,\mathrm{m}^2\,\mathrm{s}^{-1}$ depending on whether the solute molecules are polar or not. If we develop the previous equation, for isotropic molecular diffusion and an incompressible fluid ($\nabla \cdot \mathbf{u} = 0$), equation (1.2) becomes:

$$\frac{\partial c}{\partial t} + \mathbf{u} \cdot \nabla c = D_m \nabla^2 c \tag{1.3}$$

that is, in extended notation:

$$\frac{\partial c}{\partial t} + u\frac{\partial c}{\partial x} + v\frac{\partial c}{\partial y} + w\frac{\partial c}{\partial z} = D_m \left[\frac{\partial^2 c}{\partial x^2} + \frac{\partial^2 c}{\partial y^2} + \frac{\partial^2 c}{\partial z^2} \right]. \tag{1.4}$$

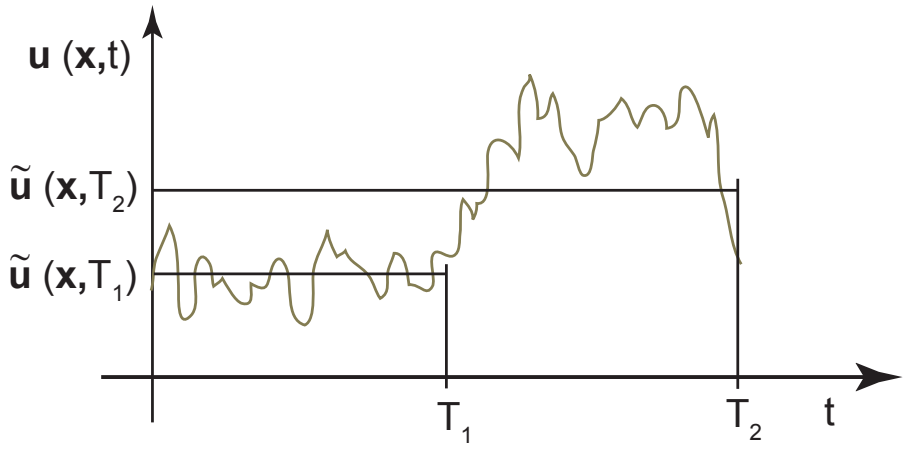

Figure 1.1. Reynolds time-averaging procedure: average of an erratic signal of velocity over two different time scales. The choice of the time step for the average can change averaging results

Equation (1.4) is valid for conservative solutes (no mass consumption or production of solute) and neutral solutes (not affected by gravity forces). The structure of this latter equation is similar to the Navier-Stokes equations, for which the transported variable is the momentum and the kinematic viscosity ν replaces the molecular diffusion coefficient. Kinematic viscosity ν $[L^2 T^{-1}]$ has indeed the same role of molecular diffusion coefficient D_m in momentum diffusion process.

1.3 Turbulent diffusion

Equation (1.4), which is the exact equation for instantaneous motions of flow and solute, cannot be solved directly in most cases, because of limited computer capacity. In mixing process, relevant variables (u, v, w and c) have a fluctuating behavior in time (turbulent flow) that acts at a scale often not relevant for practical engineering problems. Nevertheless, these fluctuations are important to explain why experimentally observed diffusivity values are higher than molecular ones. As proposed by Osborne Reynolds, a general variable χ can be divided into mean

and fluctuating quantities as described in Figure 1.1.

$$\chi(\mathbf{x},t) = \widetilde{\chi}(\mathbf{x},T_a) + \chi'(\mathbf{x},t) \tag{1.5}$$

where $\widetilde{\chi}(\mathbf{x},T_a) = \frac{1}{T_a}\int_{T_a}\chi(\mathbf{x},t)\,\mathrm{d}t$ is the average value related to the averaging time scale T_a and $\chi'(\mathbf{x},t)$ is the fluctuating component related to the average value $\widetilde{\chi}(\mathbf{x},T_a)$. It is interesting to note that, for time intervals smaller than the time scale used for the average, the term $\widetilde{\chi}(\mathbf{x},T_a)$ is a constant value whereas for time scales larger than the time scale T_a, $\widetilde{\chi}(\mathbf{x},T_a)$ can have different values in time. Each mixing process has its specific time scale and thus a specific time interval for the average. Rewriting each variable as described in equation (1.5), the advection-diffusion equation becomes:

$$\begin{aligned}\frac{\partial(\widetilde{c}+c')}{\partial t} + (\widetilde{u}+u')\frac{\partial(\widetilde{c}+c')}{\partial x} + (\widetilde{v}+v')\frac{\partial(\widetilde{c}+c')}{\partial y} + (\widetilde{w}+w')\frac{\partial(\widetilde{c}+c')}{\partial z} = \\ D\left(\frac{\partial^2(\widetilde{c}+c')}{\partial x^2} + \frac{\partial^2(\widetilde{c}+c')}{\partial y^2} + \frac{\partial^2(\widetilde{c}+c')}{\partial z^2}\right)\end{aligned} \tag{1.6}$$

If we now average each term over the time scale interval T_a and remember the following properties of the averaging procedure and of incompressible fluids:

- $\frac{1}{T_a}\int_{T_a}(\chi_1+\chi_2)\,\mathrm{d}t = \frac{1}{T_a}\int_{T_a}\chi_1\,\mathrm{d}t + \frac{1}{T_a}\int_{T_a}\chi_2\,\mathrm{d}t$
- $\frac{\partial}{\partial x}\left(\frac{1}{T_a}\int_{T_a}\chi\,\mathrm{d}t\right) = \frac{1}{T_a}\int_{T_a}\frac{\partial\chi}{\partial x}\,\mathrm{d}t\right)$
- $\frac{1}{T_a}\int_{T_a}\chi'\,\mathrm{d}t = 0$
- $\frac{\partial u}{\partial x} + \frac{\partial v}{\partial y} + \frac{\partial w}{\partial z} = \frac{\partial u'}{\partial x} + \frac{\partial v'}{\partial y} + \frac{\partial w'}{\partial z} = 0$

We thus obtain:

$$\frac{\partial\widetilde{c}}{\partial T_a} + \widetilde{u}\frac{\partial\widetilde{c}}{\partial x} + \widetilde{v}\frac{\partial\widetilde{c}}{\partial y} + \widetilde{w}\frac{\partial\widetilde{c}}{\partial z} = D_m\left[\frac{\partial^2\widetilde{c}}{\partial x^2} + \frac{\partial^2\widetilde{c}}{\partial y^2} + \frac{\partial^2\widetilde{c}}{\partial z^2}\right] - \left[\frac{\widetilde{\partial(u'c')}}{\partial x} + \frac{\widetilde{\partial(v'c')}}{\partial y} + \frac{\widetilde{\partial(w'c')}}{\partial z}\right] \tag{1.7}$$

Equation (1.7) is the equivalent of equation (1.4) for the time-averaged quantities with the addition of a specific term which is a result of the averaging procedure and is a measure of the transport process caused by turbulent fluctuations of $\mathbf{u}$ and c. Boussinesq proposed a closure model that assumes, in analogy with molecular diffusion, a direct proportionality between turbulent mass fluxes and the opposite of the concentration gradient:

$$\widetilde{\mathbf{u}'c'} = (\widetilde{u'c'}\,\widetilde{v'c'}\,\widetilde{w'c'})^T = -D_{ii}\frac{\partial \widetilde{c}}{\partial x_i} \tag{1.8}$$

where D_{ii} are the eddy diffusion coefficients in the three spatial directions x, y and z, respectively. If velocity and concentration fluctuations were statistically independent, then these terms would produce no net diffusive mass fluxes. It turns out instead that velocity and concentration irregularities are correlated and that the integral effect over time of turbulent fluxes is always much higher than the fluxes induced by Brownian motion. The time-averaged mass transport equation becomes:

$$\begin{aligned} &\frac{\partial \widetilde{c}}{\partial T_a} + \widetilde{u}\frac{\partial \widetilde{c}}{\partial x} + \widetilde{v}\frac{\partial \widetilde{c}}{\partial y} + \widetilde{w}\frac{\partial \widetilde{c}}{\partial z} = \\ &\frac{\partial}{\partial x}\left[(D_m + D_{xx})\frac{\partial \widetilde{c}}{\partial x}\right] + \frac{\partial}{\partial y}\left[(D_m + D_{yy})\frac{\partial \widetilde{c}}{\partial y}\right] + \frac{\partial}{\partial z}\left[(D_m + D_{zz})\frac{\partial \widetilde{c}}{\partial z}\right] \end{aligned} \tag{1.9}$$

Usually the mixing processes caused by turbulence are more important than molecular diffusion processes and thus molecular diffusion coefficient D_m can be neglected. Two main differences characterize equation (1.9) from equation (1.4): the first one is that D_{ii} are determined by the flow regime (in particular by the turbulence intensity) while D_m does not depend on flow regime but only on solute-solvent properties. If, for example, Reynolds number of the flow tends to small values, turbulence has a secondary role in mixing process and the fate of solute is determined mainly by molecular diffusion. If, in contrast, Reynolds number

is high, the turbulence of the flow field is the prevalent mixing mechanism. The second difference is that eddy diffusivities are scale dependent (i.e. the characteristic time scale chosen of the time-averaging procedure can vary in relation to the size of eddies that come into play). The size of the eddies is controlled by the size of the flow domain thus, in deep water bodies such as sea or lakes, diffusion processes involve several different time scales whereas in rivers, in which eddy size is controlled by depth and width, the diffusivities are not controlled by the scale of the process. Mean vertical eddy diffusivity $\overline{D_{zz}}$ in rivers can be calculated using the logarithmic velocity profile:

$$\overline{D}_{zz} = 0.067 u_* h, \tag{1.10}$$

where h is the water depth and u_* is the shear velocity. An approximate expression of the coefficient D_{yy} valid for uniform straight channels was empirically derived by *Fischer et al.* (1979) based on laboratory and field experiments:

$$D_{yy} = 0.15 u_* h. \tag{1.11}$$

In natural streams, characterized by variations of both flow depth and width (presence of meanders for example), enhances transverse mixing. Under these conditions, *Fischer et al.* (1979) suggested the following relationship:

$$D_{yy} = 0.6 u_* h\,. \tag{1.12}$$

For longitudinal mixing it can be often assumed that $D_{xx} = D_{yy}$.

1.4 Dispersion

Dispersion is the mixing process that arises from advection and diffusion in presence of velocity gradients. Role of velocity gradients becomes clear if, after the

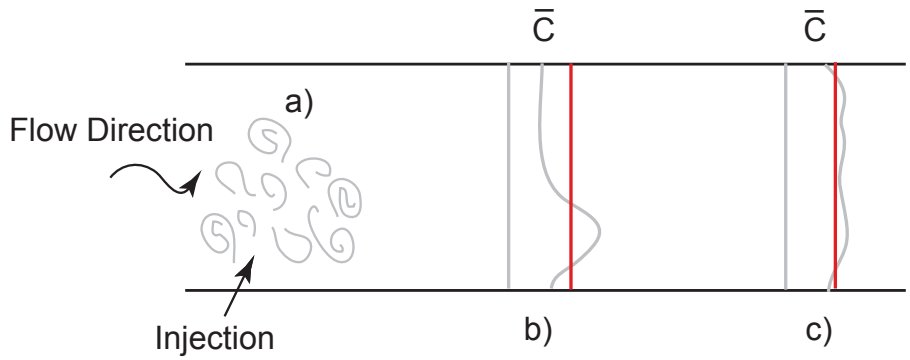

Figure 1.2. Example of the three mixing zones in a river. Near the injection (a) there is a strongly three dimensional process whereas further downstream the concentration has only an evident transversal gradient (b). When transversal concentration gradients are averaged by lateral mixing, only longitudinal gradients are relevant (c). The averaging process over the transversal area, typical of a one-dimensional models, can give good approximation of the real process only in (c) whereas other more complex models should be applied to model zones (a, b).

time-averaging procedure described in § 1.3, also a spatial-averaging procedure is performed. A spatial-averaging procedure is often convenient to simplify the description of mass transfer by averaging velocity and concentration over the vertical direction (shallow water approach), over a transverse direction or over a cross-section (unidirectional approach). Each mixing process is characterized by its typical spatial scale(s) of interest and therefore can be described only by a specific spatial-averaging procedure.

The example of a river (Figure 1.2) can be chosen to explain this concept: immediately around the injection point, the mass transfer is strongly three dimensional and is strongly dependent on the type of the injection and on the local flow regime. For this reason, to adequately model mass transfer near the injection point, is important to use a three dimensional model that takes into account the complete set of spatial and temporal variables. At some distance from the

injection, when the complete mixing along the vertical direction is already happened, transversal and longitudinal concentration gradients control the process. In this case, a vertical (depth) averaging procedure can be performed reducing the complexity of the model to a two dimensional, depth-averaged model. Further downstream, when also transversal concentration gradients have been modulated, only longitudinal concentration gradients control the mixing process. In this case a cross sectional-averaging procedure can simplify the model leading to a one-dimensional model.

1.4.1 Two dimensional depth-averaged model

To model a natural system for which the depth is small compared to the other two horizontal dimensions, equation (1.9) is integrated over the depth obtaining:

$$\frac{\partial(hC)}{\partial t} + \frac{\partial(hUC)}{\partial x} + \frac{\partial(hVC)}{\partial y} = \frac{\partial}{\partial x}\left(E_{xx}h\frac{\partial C}{\partial x}\right) + \frac{\partial}{\partial y}\left(E_{yy}h\frac{\partial C}{\partial y}\right) \tag{1.13}$$

where U, V, C are depth averaged quantities and E_{ii} are horizontal dispersion coefficients. Values of these coefficients depend on the handled problem and specific formulations can be used. Some examples related to vegetation density have been introduced in the next chapters.

1.4.2 One dimensional cross-sectional averaged model

In the case of cross-sectional averaging of the physical quantities, and no additional exchange fluxes through the lateral boundary are considered, the mass balance equation is reduced to the one-dimensional form:

$$\frac{\partial C}{\partial t} + U\frac{\partial C}{\partial x} = \frac{1}{A}\frac{\partial}{\partial x}\left(AK\frac{\partial C}{\partial x}\right), \tag{1.14}$$

where C and U are the cross-sectional average concentration and flow velocity, respectively, A is the flow cross-sectional area [L^2], and K is the longitudinal

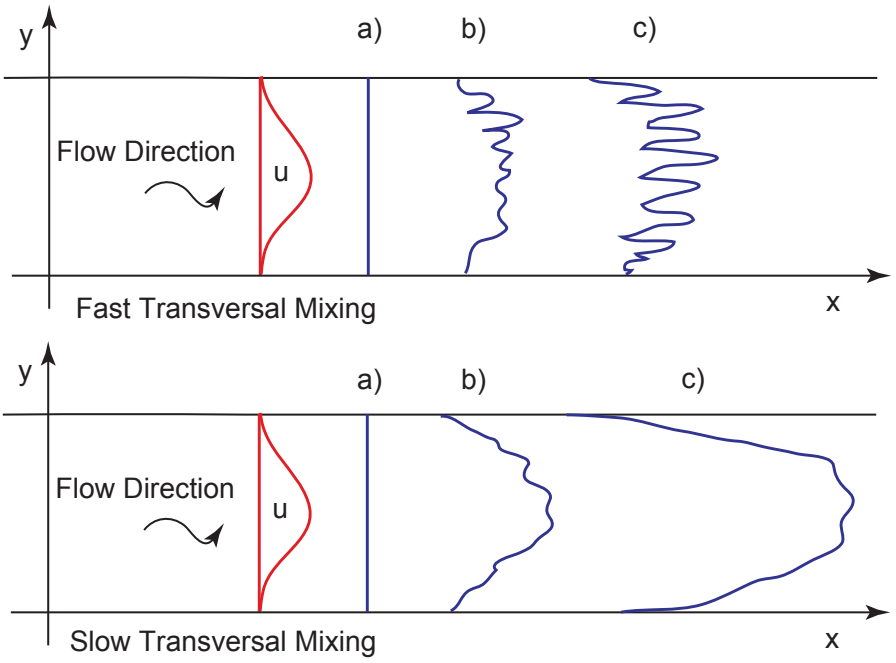

Figure 1.3. Differences in longitudinal transport processes in relation to the value of transversal mixing. In presence of fast trasversal mixing, the solute particles move with the average flow velocity and thus longitudinal dispersion has a low value. In presence of slow transversal mixing, the solute moves with local velocity of flow leading to a relevant longitudinal dispersion.

dispersion coefficient $[\mathrm{L}^2\,\mathrm{T}^{-1}]$. Under the assumption of constant A and K, the solution of equation (1.14) for an instantaneous injection of a mass of tracer M_0 in $x = 0$ at time $t = 0$ is given by:

$$C(x,t) = \frac{M_0/A}{\sqrt{4\pi K t}} \exp\left[-\frac{(x-Ut)^2}{4Kt}\right]. \tag{1.15}$$

The magnitude of the longitudinal dispersion coefficient K varies from case to case and is strongly related to the mixing velocity along the transversal direction. Usually, when transversal turbulent diffusivity D_{yy} is small, longitudinal dispersion is high and, in contrast, when transversal turbulent diffusivity D_{yy} is

high the value of longitudinal dispersion is small. The competitive role of the transverse turbulent mixing process against the non-uniformity of the velocity distribution in determining the variance of the concentration distributions is due to the ability of the solute particle to sample the cross sectional area (Figure 1.3). If the transverse mixing process is fast, solute particles sample the entire cross sectional area experimenting the whole velocity profile. Particles move with the same average velocity U and the spreading of the solute along the longitudinal direction is therefore limited. On the contrary, if transverse mixing is slow, particles tend to maintain the same position in the flow domain experimenting only a limited velocity range. This characteristic produces a longitudinal spreading of the solute cloud that lead to an higher value of longitudinal dispersion coefficient. To note that vertical turbulent mixing act in the same manner as transverse turbulent mixing but has a limited role due to the fact that vertical mixing can be regarded, in natural rivers, as instantaneous. An approximated relationship for K valid for streams with large width-to-depth ratios was suggested by *Fischer* (1975):

$$K = 0.011 \frac{U^2 B_r^2}{h u_*}, \tag{1.16}$$

1.5 Additional fluxes on the boundary

In § 1.4 a formulation of one-dimensional mass transfer equation has been proposed assuming the absence of mass solute fluxes through the river bed and through water surface. Although very useful, this simple model can describe only a small part of the real mixing processes in natural environments. Presence of retention in dead zones, advection and diffusion of decaying or volatile solutes, hyporheic contamination and solute consumption by biological components can clearly modify the mass transfer equation. For this reason, equation (1.14) can be

extended in order to account for these different processes as follows:

$$\frac{\partial CA}{\partial t} + \frac{\partial QC}{\partial x} = \frac{\partial}{\partial x}\left(AK\frac{\partial C}{\partial x}\right) \pm F_B P \pm F_A B_r - k'CA \pm S\,, \tag{1.17}$$

where Q is the discharge of the river $[\mathrm{L}^3\,\mathrm{T}^{-1}]$, F_B is the mass flux $[\mathrm{M}\,\mathrm{L}^{-2}\,\mathrm{T}^{-1}]$ of solute through the wetted perimeter P $[\mathrm{L}]$, F_A is the mass flux of solute $[\mathrm{M}\,\mathrm{L}^{-2}\,\mathrm{T}^{-1}]$ through the surface B_r $[\mathrm{L}]$, k' is a decay rate $[\mathrm{L}\,\mathrm{T}^{-1}]$ and the term S $[\mathrm{M}\,\mathrm{L}^{-1}\,\mathrm{T}^{-1}]$ is a general production/consumption term.

The decay of a solute represented by the term $-k'CA$ is a spontaneous phenomenon independent of the presence of other substances and is almost ever associated with the radioactive decay of the substances. Radioactive decay is however a very rare mechanism that acts at very long time scales. For common engineering purposes, this mechanism is often discarded but its mathematical formulation is very helpful to treat other non-conservative processes in natural environments. Other phenomena, although not related with the natural radioactive decay, can be indeed rewritten with the same mathematical formulation. This is the case of a first order decay chemical breakdown in wetlands or the loss of a volatile solute through the water surface.

Other mass exchanges with different types of storage zones as vegetated pockets, dead zones and permeable layers can happen in natural environments, as illustrated in Figure 1.4. Experimental observations of the presence of these additional boundary fluxes that can not be represented with the classical advection-diffusion equation have been provided since the early 50's by a number of studies using tracer tests (*Elder*, 1959; *Krenkel and Orlob*, 1962; *Thackston and Schnelle*, 1970; *Nordin and Sabol*, 1974; *Day*, 1975; *Nordin and Troutman*, 1980). These domains have fundamental role in determining the fate of transported substances for three reasons: first of all, they increase the dispersion of solute in the surface water; second, they control the exchange between the stream water and the

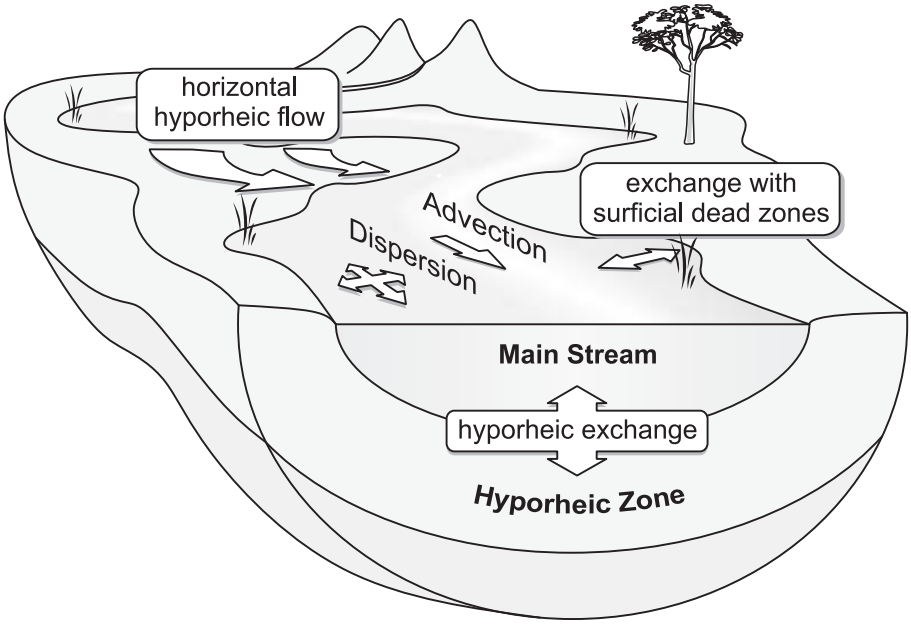

Figure 1.4. Illustration of the transport processes acting in a river. The downstream transport of solutes is governed by advection and hydrodynamic dispersion in the main stream, and by mass exchanges with different retention zones. These include vertical exchanges with the underlying sediments, where adsorption process may take place; lateral exchanges with surficial dead zones, typically vegetated pockets; and horizontal hyporheic flows induced by planimetric variation of the stream direction. (Figure kindly provided by authors, (*Marion et al.*, 2008)).

surrounding aquifer; third, they govern the storage of contaminants into the bed sediments. In the last 40 years, several models have been proposed to represent these additional fluxes and the retention effect caused by the transient storage of substances in these retention domains: among the others, it has to mention the TSM model presented by (*Bencala and Walters*, 1983), OTIS model proposed by (*Runkel*, 1998) and the most recent STIR model (*Marion and Zaramella*, 2005; *Marion et al.*, 2008) that has been taken as a reference model for the analysis presented in the next chapters.

Chapter 2

STIR model: application to three river environments[1]

2.1 Introduction

Retention processes in streams affect the fate of nutrients and contaminants by controlling mass exchanges between different compartments. A distinction is typically drawn between a main channel, where the velocity is relatively high, and different retention domains, where the flow velocity is relatively slow. Vegetated zones, side pockets of recirculating or stagnant water and the porous medium represent storage domains where solutes can be temporarily retained and gradually released over time. While temporarily trapped in the storage zones, solute can be adsorbed onto sediments or uptaken by the microfauna, therefore retention are important in determining both the vulnerability of a river to contamination processes and the long term evolution of a fluvial ecosystem. The increasing interest in mass exchanges with storage zones, in particular with the hyporheic zone, has led to the formulation of different mathematical models. The Transient Storage Model (TSM) presented by (*Bencala and Walters*, 1983) has

[1]The contents of this chapter have been published in: A. Bottacin-Busolin, A. Marion, T. Musner, M. Tregnaghi, M. Zaramella, Evidence of distinct contaminant transport patterns in rivers using tracer tests and a multiple domain retention model, *Advances in Water Resources*, 34 (2011), 737-746.

been widely applied in the last decades to both large rivers and small streams. In the TSM, the net mass exchange between the main channel and the storage zones is represented as a first-order mass transfer implying an exponential residence time distribution (RTD) (*Hart*, 1995). More complex mathematical formulations have been developed in the last few years to represent mass exchanges with the hyporheic zone. *Haggerty et al.* (2000) suggested an advection-dispersion mass transfer equation in which the transient storage is expressed through a convolution integral of the in-stream concentration and a residence time distribution. A similar mathematical formulation was used by *Wörman et al.* (2002) who developed a model (ASP, advective-storage path) based on *Elliott and Brooks* (1997a,b) theory of bedform-induced hyporheic exchange. Recently the application of a fractional advection-dispersion equation (*Deng et al.*, 2006) and of the Continuous Time Random Walk (*Boano et al.*, 2007) has also been suggested. In this chapter, the general residence time approach of the STIR model (Solute Transport In Rivers) (*Marion and Zaramella*, 2005; *Marion et al.*, 2008) is used.

2.2 Overview of the STIR model

The STIR model (Solute Transport In Rivers) was presented in its first form by *Marion and Zaramella* (2005) and then further extended by *Marion et al.* (2008). The model represents classical longitudinal dispersion of a solute in a river coupled with transient storage mediated by different storage domains, each of them is characterized by a proper residence time distribution. Differently from other classical models as OTIS and TSM, STIR approaches the problem of the propagation of a solute along the river using a stochastic approach: the time needed by a particle to travel a distance x, indicated with $\mathcal{T}$, is a random variable with probability density function $r(t;x)$ and can be viewed as a sum of the time spent in the main current ($\mathcal{T}_W$ characterized by its probability density function $r_W(t;x)$) and of the time $\mathcal{T}_S$ that is the sum of the single residence times within the N storage

domains ($\mathcal{T}_S = \sum_{i=1}^{N} \mathcal{T}_{Si}$).

A particle, during its permanence in the superficial main current, can be trapped n times in the i-th retention domain. The number of times the particle is trapped is a discrete random variable $\mathcal{N}_i$ with conditional distribution $p_i(n|\mathcal{T}_W = t_W)$. If each trapping event is assumed to be independent to the other, the time $\mathcal{T}_{Si}$ spent in each retention domain is characterized by the following conditional density:

$$r_{Si|n}(t) = \varphi_i(t) \underbrace{*\ldots*}_{n \text{ times}} \varphi_i(t) = [\varphi_i(t)]^{*n}, \tag{2.1}$$

where the symbol $(*)$ denotes time convolution and $\varphi_i(t)$ represents the probability density function of the specific retention domain. The conditional density of $\mathcal{T}_{Si}$ given $\mathcal{T}_W = t_W$ is thus:

$$r_{Si}(t|t_W) = \sum_{n=0}^{\infty} p_i(n|t_W)\, r_{Si|n}(t), \tag{2.2}$$

where $p_i(n|t_W)$ is the uptake probability of a particle to be trapped n times, given $\mathcal{T}_W = t_W$. For uniformly spaced storage zones, the uptake probability can be modeled by a Poisson distribution with parameter $\alpha_i t_W$ where α_i represents the flow rate into the storage zone per unit superficial volume. Equation (2.2) holds for each N-th retention domain, thus, the conditional density of the total time $\mathcal{T}_S$ spent in the retention domains, given $\mathcal{T}_W = t_W$ is:

$$r_S(t|t_W) = r_{S_1}(t|t_W) * \ldots * r_{S_N}(t|t_W). \tag{2.3}$$

The probability density function $r_W(t;x)$ of the time $\mathcal{T}_W$ spent in the main current can be derived from the solution of the advection diffusion equation. For an input mass pulse, when the computational domain is $x > 0$ and boundary condition at

infinity $C(x \to \infty, t) = 0$, holds:

$$r_W(t;x) = \frac{x}{2\sqrt{\pi K t^3}} \exp\left[-\frac{(x-Ut)^2}{4Kt}\right]. \tag{2.4}$$

Once $r_S(t|t_W)$ and $r_W(t;x)$ are known, is possible to express the overall residence time distribution within a stream reach of length x as:

$$r(t;x) = \int_0^t r_W(t-\tau;x)\, r_S(\tau|t-\tau)\, d\tau\,. \tag{2.5}$$

Equation (2.5) can be therefore used to determine the in-sream solute concentration (*Bottacin Busolin*, 2010): the quantity $r(t;x)dt$ represents the fraction of mass flowing through the downstream section in the time interval $[t, t+dt]$, and the flux is given by the convolution of $r(t;x)$ with the input flux. For a mass pulse concentrated in time this is given by $M_0/A\delta(t)$. The variation per unit time of the total concentration is equal to the opposite of the divergence of the local flux, $(M_0/A\delta(t)) * r(t;x)$, hence:

$$\frac{\partial C_\delta(x,t)}{\partial t} = -\frac{\partial}{\partial x}\int_0^t M_0/A\delta(t) r(t-\tau;x)\, d\tau = -\frac{M_0}{A}\frac{\partial r(t;x)}{\partial x}, \tag{2.6}$$

where the subscript δ is used to denote the solute concentration generated by a mass pulse. From the solution of Equation (2.6), through time convolution, can be derived solutions for other kind of boundary conditions different from mass pulse.

2.3 Application of STIR in three rivers: sites description

The basin of the Yarqon River spreads out along a wide area of the Israeli territory, from the West Bank down to the plain of Tel Aviv. The total extension of the basin is approximately 1805 km^2. The most important affluent of the Yarqon River is the Ayalon River, which drains all the southern area, including Jerusalem region,

Figure 2.1. Pictures of the Yarqon river illustrating typical study reaches.

and flows into the Yarqon River 2 km upstream of its estuary. It flows entirely along the coastal strip: the total length is 28 km, the sources altitude is about 50 m above sea level, and its average bed-slope is 0.0018. These characteristics of the river profile involve the formation of many meanders, which are typical of mild bed slopes. The population of the entire river basin counts approximately 750,000 inhabitants. Agricultural and industrial activities are present in this area, as well as trading and urban development, leading to one of the highest population density in Israel. The growth of the population, associated to the industrial and agricultural development since 1948, made water quality of the Yarqon River increasingly polluted. Contamination is mainly due to the drawing of the river sources and the drainage of the industrial effluents into the main river. A picture of a typical study reach is given in Figure 2.1. In the study reach, the river is characterized by thick bank vegetation, no submerged vegetation on the bed and a sandy bed. The Brenton torrent is an Italian torrential stream located in the area of Treviso in Northern Italy. The tributary catchment has an area of approximately 60 km^2 and the elevation from the average sea level varies from 45 to 496 m; the length of the channel is about 13.5 km with an average slope of 0.0042. The Brenton catchment basin was formed for the most part by the deposition of sediments transported by the Piave river since the last glaciations.

Figure 2.2. Pictures of the Brenton torrent illustrating typical study reaches.

The transported sediments are primarily coarse debris of grit and limestone. The bed is made of a thick, high permeable layer of gravel and is characterized by the presence of iron hydroxide due to the dissolving and hydrolyzing effect that meteoric waters, containing carbonic acid, exert on the gravel. The overall length of the study reach is about 5.8 km. The channel is primarily straight but has a few 90° bends and a few large radius bends. The channel cross-section is regular with no flood plains and without sensible variations of the flow cross sectional area, except for a few localized contractions. The channel bed is almost entirely natural, with only a few quite short reaches in which the banks are reinforced with concrete or stone. The banks are thickly vegetated (Figure 2.2).

The Desturo canal is a small 5.6 km-long drainage canal which is part of the drainage basin of the Venice Lagoon in Northern Italy. The canal is located just outside of an urban settlement and is used for irrigation purposes. The Desturo canal is affected by pollution due to distributed inputs of fertilizers used in agricultural activity. However, the main sources of pollution are due to input of water from a waste-water treatment plant of the nearby Monselice village and to inputs of non-treated water during rain periods from urban drainage systems. The total length of the study reach is equal to 3300 m and has almost uniform characteris-

Figure 2.3. Pictures of the Desturo canal illustrating a typical study reach.

tics with few channel bends. The channel cross section is trapezoidal with flood plains and natural banks. The vegetation on the banks is quite thin, with virtually no masts and bushes. The sediment bed is made of a sandy-silty material and at the time of the tests the channel bottom was characterized by the presence of algae, submerged vegetation, and pieces of marsh reeds (Figure 2.3).

2.4 Methods

2.4.1 Tracer Tests

Tracer tests were carried out in the Yarqon river in April 2005, in the Brenton torrent in June-July 2007, and in the Desturo canal in October 2007. The experiments consisted in both instantaneous (slug) and continuous (step) injections of rhodamine WT (RWT) fluorescent dye. For step injections, a peristaltic pump was used to ensure a constant continuous rate of input throughout the injection period. In each test RWT concentrations were measured at two downstream sections with a sampling period of 10 s using portable field fluorometers (Turner Design SCUFA). In addition to tracer concentrations, the fluorometers measured water turbidity, which was then used in the detrend procedure of the tracer BTCs

to remove artifact generated by variations of water turbidity. Part of the curves are excluded from the analysis presented here due to poor quality of the data, either because the concentration signal was too noisy or because the tail values of the concentration curves could not be obtained for sufficiently long times to permit an unambiguous determination of the model parameters. The location of the injection and the measurement sections was chosen so that the study reaches could be considered as approximately uniform. The length of the reaches, L, varies from around 660 to 1900 m for the Yarqon river (Table 2.1 a)), from 620 to 2160 m for the Brenton torrent (Table 2.2 a)), and from 260 to 340 m for the Desturo canal (Table 2.3 a)). In all cases, the distance from injection allowed the tracer to be well mixed over the cross-section at the measurement stations.

In Tables 2.1, 2.2 and 2.3 the value of the mass recovery ratio, r_M, is also reported. This is defined as:

$$r_M = \frac{\sum_j Q C_{obs,j} \Delta t}{M_0}, \tag{2.7}$$

where Q is the flow discharge, $C_{obs,j}$ is the j-th observed tracer concentrations, and Δt is the sampling interval. In the Yarqon river r_M varies from 0.71, in reach 4, to 0.89 in reach 1. It is interesting to note that lowest recovery ratio is found in reach 4 which is significantly longer than the other reaches. This might indicate a positive correlation between the value of the unrecovered mass and the reach length, though a consistent pattern is not observed. In the Brenton torrent the recovery ratio varies from 0.74 to 0.80, with lower values associated to longer reaches, whereas r_M ranges from 0.83 to 0.88 in the Desturo canal. If we compare the values of the recovery ratios in the different streams, we observe that higher ratios are found in the Desturo canal, where the permeability of the substrate material is relatively low, whereas lower ratios are found in the Brenton torrent, which has high bed permeability compared to the other streams. Intermediate

values are found in the Yarqon river. Higher recovery ratios are generally associated with streams with minimal hyporheic exchange, since the probability of the tracer to enter the bottom sediments and reenter the stream beyond the monitoring point is minimal. In our experiments, recovery ratios also varied with reach lengths and cross-sections, but a consistent pattern between the variables across the systems studied was not observed. Flow discharges during the tracer tests were obtained from data provided by local consortia equipped with their own meters. The flow cross-sectional area was inferred from technical cartography of the channel sections and partly from direct measurements along the study reaches. Values of the flow discharge Q, average flow velocity U, and mean advective travel time $t_{ad} = L/U$ are reported in Tables 2.1, 2.2 and 2.3 for the Yarqon river, the Brenton torrent and the Desturo canal, respectively. The ranges of flow discharges considered in the tracer experiments are $0.21 - 0.41\,\mathrm{m^3\,s^{-1}}$ for the Yarqon river, $0.68 - 1.5\,\mathrm{m^3\,s^{-1}}$ for the Brenton torrent, and $0.042 - 0.053\,\mathrm{m^3\,s^{-1}}$ for the Desturo canal. Mean advective travel times in the study reaches ranges from about 1 to 3 h for the Yarqon river, from 10 to 50 min for the Brenton torrent, and from 20 to 40 min for the Desturo canal.

2.4.2 STIR model closures

Here the STIR model is applied using two distinct modeling closures to represent transient storage. In both cases the residence time distribution in the storage zones is decomposed as follows:

$$\varphi(t) = \frac{1}{\alpha}\left[\alpha_1 \varphi_1(t) + \alpha_2 \varphi_2(t)\right], \tag{2.8}$$

where

$$\alpha = \alpha_1 + \alpha_2, \tag{2.9}$$

where Here, α_1 and $\varphi_1(t)$ are the transfer rate and residence time PDF associated to short timescale retention, respectively, and α_2 and $\varphi_2(t)$ are the transfer rate and residence time PDF associated to longer timescale retention. The decomposition given by equations (2.8)-(2.9) can be interpreted as a two-storage zone representation of transient storage where shorter timescales are expected to be associated to surface dead zone storage, whereas longer timescales are associated to hyporheic exchange.

In the first modeling closures the decomposition involves two exponential RTD's:

$$\varphi_1(t) = \frac{1}{T_1} e^{-t/T_1}, \tag{2.10a}$$

$$\varphi_2(t) = \frac{1}{T_2} e^{-t/T_2}. \tag{2.10b}$$

whereas the second one involves an exponential RTD for and a power law distribution approximating *Elliott and Brooks* (1997a) solution for bedform-induced hyporheic exchange. Using the approximation given by *Bottacin-Busolin and Marion* (2010), this can be written as:

$$\varphi_2(t) = \frac{\pi}{T_2}\left[\frac{1}{(t/T_2+2)^2} - \frac{1}{4} exp\left(-\frac{\pi}{2(\pi-2)}\frac{t}{T_2}\right)\right] \tag{2.11}$$

which clearly decays as t^{-2} at longer times.

In order to fully characterize the transport in the study reach, the model parameters must be estimated using an inverse approach. Calibration parameters include the longitudinal dispersion coefficient K [$L^2 T^{-1}$] and the exchange parameters characterizing the exchange with the retention domains, that is the transfer rate into the first storage zone α_1 [T^{-1}] and in the second storage zone α_2 [T^{-1}] and the relevant timescales of retention T_1 and T_2 [T]. Using the average channel width B_r and flow depth h based on technical cartography and partly

on direct in situ measurements, the average cross-sectional area is calculated as $A = B_r h$, and the average velocity as $U = Q/A$. Following *Bottacin-Busolin et al.* (2009), model calibration is performed in mixed scale using a linear scale to fit the bulk of the curve and log-scale to fit the tail. This is accomplished by minimizing the following root mean square error:

$$\mathrm{RMSE} = \left[\frac{1}{N} \left(\frac{\sum_{i \in I_U} (C_{\mathrm{sim},i} - C_{\mathrm{obs},i})^2}{(\max_{i \in I} C_{\mathrm{obs},i} - \min_{i \in I} C_{\mathrm{obs}})^2} + \frac{\sum_{I \in I_L} (\log C_{\mathrm{sim},i} - \log C_{\mathrm{obs},i})^2}{(\max_{i \in I} \log C_{\mathrm{obs},i} - \min_{i \in I} \log C_{\mathrm{obs},i})^2} \right) \right]^{1/2} \tag{2.12}$$

where C_{obs} and C_{sim} are the observed and simulated concentration values, respectively, I_U and I_L are the sets of the observed values higher and lower than a given threshold concentration, respectively, $I = I_U \cup I_L$ is the total set, and N is the number of elements in I. The threshold value was set equal to 20% of the peak concentration. The concentration values closer to zero are neglected in calculating, generally by excluding from the computation 5% of the total set corresponding to the lowest values (*Bottacin-Busolin et al.*, 2009). The optimization is performed using the differential evolution method for global optimization by *Storn and Price* (1997).

In addition to model calibration, an estimate of the uncertainty associated to the optimized value of each parameter is given as follows. For each parameter we determine the range of values in which the RMSE differs from the optimal (i.e. the minimum) value by less than 5%, provided that the other parameters are optimized accordingly. It should be stressed that this interval is not obtained by individually varying each parameter while keeping fixed the others, but searching for other values of the other parameters that produce similar fits according to the described criterion. In other words, if we change the value of a parameter in that range, we need to adequately change the values of the other parameters

to obtain a similarly good fit. Thus, this interval of variation provides a measure of the equifinality of the model parameters, rather than a measure of the model sensitivity to the variation of an individual parameter. Large variation intervals imply higher degrees of equifinality, and therefore a larger set of combinations of the model parameters that produce similar BTCs.

2.5 Results and Discussion

Transient storage processes in natural streams generate a delay in the downstream transport of a tracer inducing longer tails in the observed BTCs and increasing the skewness of the concentration distributions. Here, the STIR solute transport model has been used in combination with tracer test data to characterize transient storage in three case studies.

2.5.1 Two exponential RTDs model

The results of the calibration of the STIR model with the two exponential closure for the storage time distribution are presented in Table 2.1 b), Table 2.2 b), Table 2.3 b) for the Yarqon river, the Brenton torrent and the Desturo canal, respectively. A graphical comparison between the experimental data and the simulated breakthrough curves is given in Figure 2.4 for the Yarqon river, Figure 2.5 for the Brenton torrent, and in Figure 2.6 for the Desturo canal. Breakthrough curves are plotted using the normalized quantities $t^* = (t - \overline{t})/t_{ad}$ for time, where $\overline{t}$ is the centroid of the input concentration distribution, and $C^* = C/C_{max}$ for concentration, where C_{max} is the peak concentration. The curves are plotted in both linear and semi-log scale to emphasize their tail behavior, on which the retention parameters are primarily dependent. In the first three reaches of the Yarqon river the values of the longitudinal dispersion coefficient, K, are quite consistent, with an average value of $0.3\,\mathrm{m}^2/\mathrm{s}$, whereas in the fourth study reach the value is substantially higher, $K = 2.80\,\mathrm{m}^2/\mathrm{s}$. This is due to a larger channel width in reach 4, which changes from about 6 m, in reach 2 and 3, to about 8 m in reach 4,

and a lower water depth, which combined yield similar values of the flow cross-sectional area. The higher discharge characterizing the Brenton torrent produces, as a consequence, higher values of the longitudinal dispersion coefficient, which is very similar in all the four reaches and is about 2.0 m^2/s. In the Desturo canal the K is rather small, that is about 0.1 m^2/s, as a consequence of the relatively small channel width and flow discharge. Again, the value of K is quite consistent in all the four reaches of the Desturo canal. In the study reaches of the Yarqon river the average timescale T_1 of fast transient storage varies from 163 to 436 s, with an average value of 262 ± 152 s (Table 2.1 b)). The mean residence time T_1 associated to long timescale retention varies from 1720 to 3781 s and appears to be higher for increasing reach lengths. In Reach 3 of the Yarqon river, the optimization procedure converges to $\alpha \simeq 0$, whereas the timescale T_1 converges to a relatively high value compared to the other reaches (T_1 = 436 s), indicating that a single exponential distribution is sufficient in this case to adequately represent the BTC. In the study reaches of the Brenton torrent the timescale T_1 ranges from 51 s to 104 s, with an average value of 68 ± 25 s, and it is clearly higher for increasing reach lengths (Table 2.2 b)). The same increasing trend is visible for the timescale T_2 which varies from 733 s to 1735 s as the reach length, L, increases from 620 to 2160 m. In the Desturo canal the timescale T_1 ranges from 60 s to 171 s, with average 117 ± 48 s, whereas T_2 ranges from 280 to 397 s, with average 352 ± 50 s. In this case, a clear increasing trend of T_1 and T_2 with the reach length is not apparent.

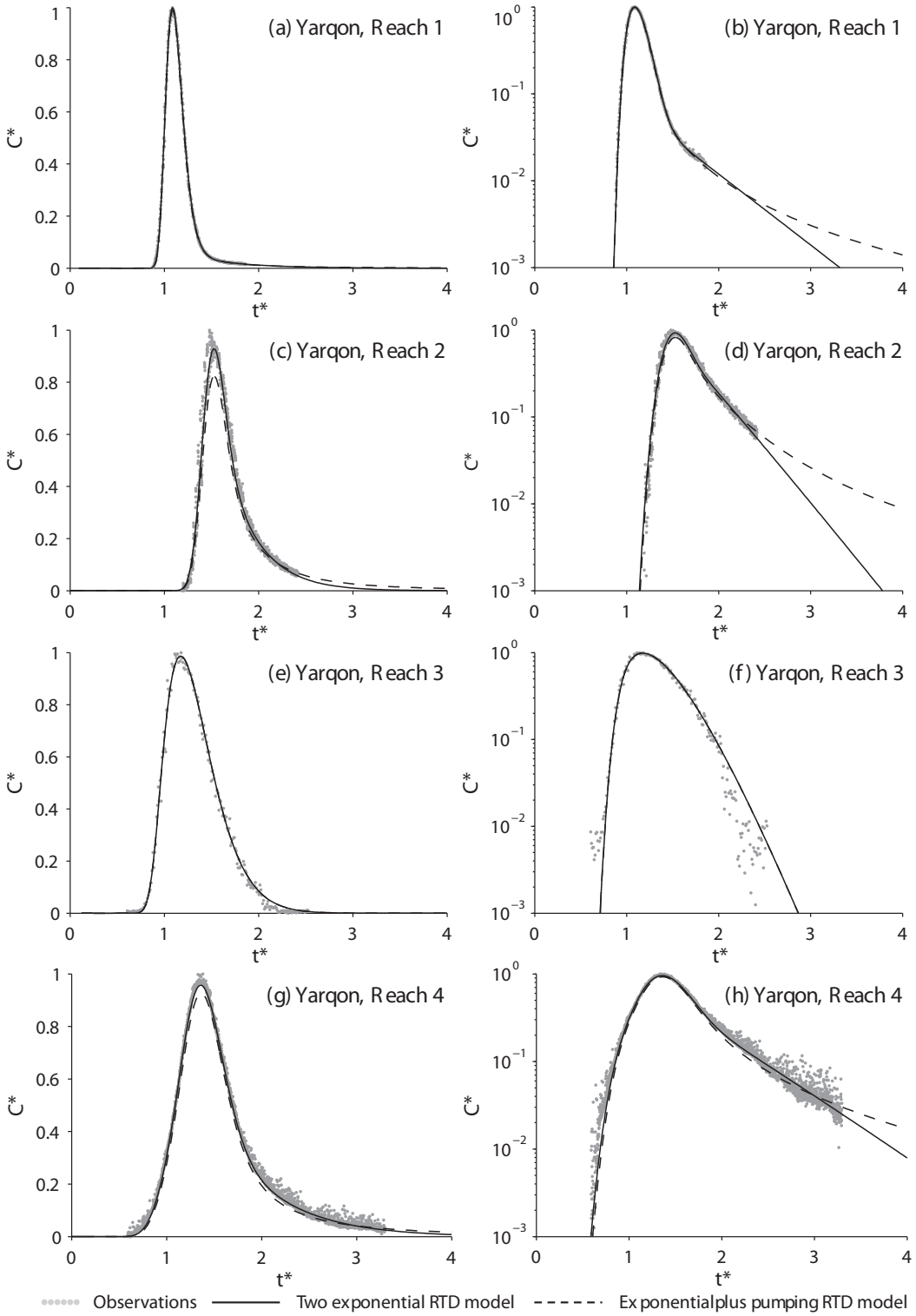

Figure 2.4. Observed and simulated breakthrough curves for the Yarqon river (left) in linear scale and (right) semi-log scale.

Reach	1	2	3	4
(a) Study reaches				
L (m)	1084	816	657	1887
Q ($m^3 s^{-1}$)	0.21	0.21	0.43	0.41
A (m^2)	1.06	2.18	2.71	2.15
t_{ad} (s)	5391	8345	4141	9895
r_M (s)	0.89	0.86	0.80	0.71
(b) Parameters of STIR model with two exponential RTDs				
K ($m^2 s^{-1}$)	0.24 ± 0.002	0.25 ± 0.012	0.49 ± 0.04	2.80 ± 0.20
α_1 ($\times 10^{-4} s^{-1}$)	7.4 ± 0.03	9.4 ± 0.7	7.3 ± 0.4	7.3 ± 0.5
α_2 ($\times 10^{-4} s^{-1}$)	0.25 ± 0.001	0.78 ± 0.04	0	0.54 ± 0.01
T_1 (s)	163 ± 2	109 ± 8	436 ± 15	340 ± 23
T_2 (s)	2382 ± 24	1720 ± 62	—	3781 ± 75
RMSE[a] ($\times 10^{-2}$)	1.36	4.36	10.29	5.85
(c) Parameters of STIR model with exponential plus pumping RTD				
K ($m^2 s^{-1}$)	0.24 ± 0.006	0.25 ± 0.03	0.49 ± 0.05	2.80 ± 0.25
α_1 ($\times 10^{-4} s^{-1}$)	7.7 ± 0.1	15.0 ± 1.6	7.3 ± 0.5	9.6 ± 0.8
α_2 ($\times 10^{-4} s^{-1}$)	0.29 ± 0.005	1.1 ± 0.1	0	0.58 ± 0.05
T_1 (s)	153 ± 2	63 ± 7	436 ± 21	255 ± 25
T_2 (s)	485 ± 17	297 ± 31	—	530 ± 37
RMSE[a] ($\times 10^{-2}$)	1.71	5.29	10.29	7.86

[a] The parameter RMSE is unitless.

Table 2.1. Summary of test and model parameters for the Yarqon River. Values of optimized parameters are reported as the intervals for which model optimization produces an RMSE differing by less than 5% from the global optimum value. The RMSE reported in the table corresponds to the global optimum.

The transfer rates are found to be higher in the Desturo canal, with α_1 in the

range $(10.1 - 13.5) \times 10^{-4}\,s^{-1}$ and $\alpha_2 = (0.70 - 4.27) \times 10^{-4}\,s^{-1}$, compared to the Brenton torrent where $\alpha_1 = ((2.8-15.5)\times 10^{-4}\,s^{-1}$ and $\alpha_2 = (0.06-0.26)\times 10^{-4}\,s^{-1}$, and the Yarqon river, where $\alpha_1 = (7.3-9.4)\times 10^{-4}\,s^{-1}$ and $\alpha_2 = (0-0.78)\times 10^{-4}\,s^{-1}$. It can be noticed that the transfer rate associated to the longer timescale retention component are at least an order of magnitude lower than the transfer rate associated to the shorter one. This is consistent with the fact that fast transient storage in surface dead zones is typically characterized by high exchange fluxes, whereas the transient storage in the hyporheic zones is associated to relatively small transfer rates and long residence times. The values of a1 and a2 do not exhibit particular trends as a function of the reach length L or of the average advective travel time, t_{ad}. The higher values of the timescale T_2 characterizing the Brenton torrent and the Yarqon river compared to the Desturo canal can be seen as a consequence of the higher permeability of the bed, which implies significant hyporheic fluxes in the subsurface. In the Desturo canal, the low permeability of the bed implies that the subsurface fluxes are extremely small, and the observed retention effects are likely to be primarily due to surface dead zones and, in particular, to the thick submerged vegetation characterizing the channel bed. Nevertheless, it is not possible to compare unambiguously the properties of short timescale retention in the streams analyzed. In the Brenton torrent the longitudinal dispersion coefficients are an order of magnitude greater than those found in the Desturo canal, which allows a wider range of retention phenomena to be lumped in the parameter K. An important parameter of the two-exponential RTD model is given by the ratio of the two timescales of retention T_2/T_1. When this ratio is close to 1, the breakthrough curves can be well represented by a single exponential distribution, and hence the conventional TSM model with a single storage zone is expected to provide acceptable approximations of the experimental data. This is the case of the Desturo canal for which the mean ratio is T_2/T_1 is 3.3 ± 1.1. In a semi-log graph, the corresponding breakthrough curves tend

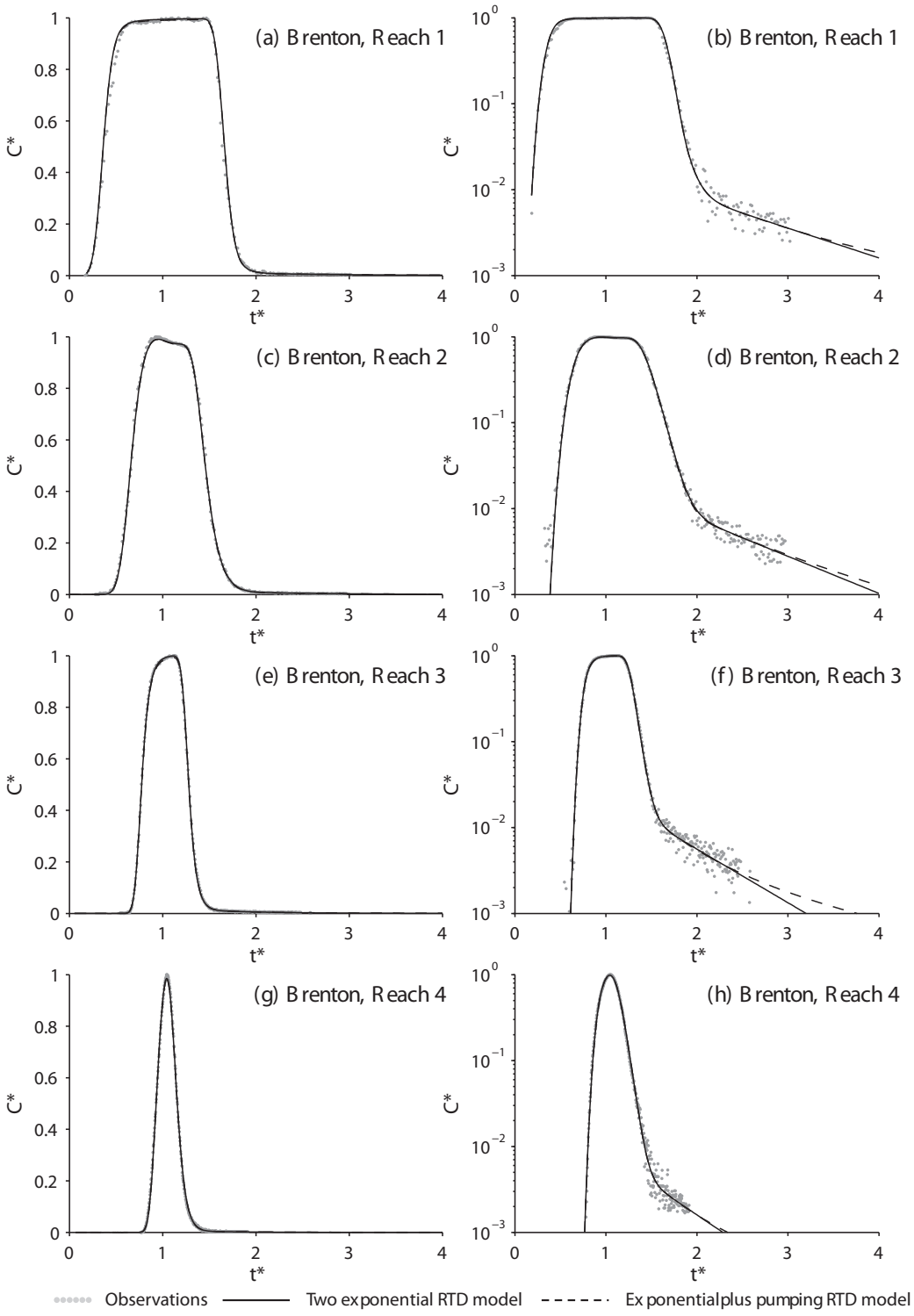

Figure 2.5. Observed and simulated breakthrough curves for the Brenton torrent (left) in linear scale and (right) semi-log scale.

to follow a linear pattern after the concentration peak. High ratios are instead found in the Yarqon river and the Brenton torrent, for which the average ratio T_2/T_1 is 11.3 ± 5.3 and 16.3 ± 7.1, respectively. When plotted in semi-log scale, the relevant breakthrough curves shows a long tail behavior. In particular, in the case of the Brenton torrent, the decreasing part of the curve is characterized by a clear change of slope Figure 2.5: the part of the curve between the concentration peak and the bend is associated to quicker exchange processes and determines primarily the value of T_1 and α_1; the subsequent part the curve is associated to long term retention and is related to the parameters T_2 and α_2. The rising part of the curve is mainly associated to advection and dispersion processes in the main channel and the steepness of the curve depends primarily on the value of the longitudinal dispersion coefficient. If we consider the uncertainty associated with the optimal value of the model parameters, we notice that the interval of variability that allows similar curve fitting, in the sense described in section 3.3, is found in most cases to be less than 17% of the optimal value. If we consider the variability that characterizes environmental applications, this level of uncertainty can be considered as acceptable for a model. Exceptions apply for the cases, e.g. one Yarqon reach and one Desturo reach, where the second component of transient storage appear to vanish, and an equivalent comparative equifinality validation procedure could not be applied. Furthermore, it is important to observe that this variability of the model parameters does not affect the comparative analysis of the model parameters between the different streams presented above. Whenever the exchange rate of the second storage component is different from zero, the two storage zone model cannot be substituted by a single exponential RTD model while keeping a similar quality of the fit. This implies that the model is not over-parameterized when the two-exponential RTD closure is used.

Reach	1	2	3	4
(a) Study reaches				
L (m)	620	1080	1560	2160
Q ($m^3 s^{-1}$)	1.5	1.5	1.5	0.68
A (m^2)	1.45	1.34	1.57	0.96
t_{ad} (s)	599	962	1632	3036
r_M (s)	0.80	0.83	0.76	0.74
(b) Parameters of STIR model with two exponential RTDs				
K ($m^2 s^{-1}$)	1.98 ± 0.10	2.01 ± 0.16	1.85 ± 0.12	1.95 ± 0.005
α_1 ($\times 10^{-4} s^{-1}$)	2.8 ± 0.2	15.5 ± 0.6	5.0 ± 0.3	4.9 ± 0.07
α_2 ($\times 10^{-4} s^{-1}$)	0.26 ± 0.01	0.11 ± 0.004	0.18 ± 0.004	0.6 ± 0.001
T_1 (s)	51 ± 4	52 ± 2	66 ± 3	104 ± 1
T_2 (s)	733 ± 56	912 ± 58	1081 ± 47	1735 ± 105
RMSE[a] ($\times 10^{-2}$)	4.94	2.53	3.26	2.90
(c) Parameters of STIR model with exponential plus pumping RTD				
K ($m^2 s^{-1}$)	1.98 ± 0.13	2.00 ± 0.19	1.91 ± 0.13	1.97 ± 0.08
α_1 ($\times 10^{-4} s^{-1}$)	2.8 ± 0.29	1.59 ± 0.66	5.10 ± 0.35	4.9 ± 0.1
α_2 ($\times 10^{-4} s^{-1}$)	0.29 ± 0.02	0.12 ± 0.006	0.20 ± 0.009	0.07 ± 0.002
T_1 (s)	52 ± 8	51 ± 3	65 ± 4	104 ± 3
T_2 (s)	198 ± 23	290 ± 28	280 ± 22	474 ± 45
RMSE[a] ($\times 10^{-2}$)	4.98	2.52	3.30	2.92

[a] The parameter RMSE is unitless.

Table 2.2. Summary of test and model parameters for the Brenton torrent. Values of optimized parameters are reported as the intervals for which model optimization produces an RMSE differing by less than 5% from the global optimum value. The RMSE reported in the table corresponds to the global optimum.

2.5.2 Exponential RTD plus pumping RTD model

The parameters obtained by calibration of the model assuming an exponential RTD and the pumping RTD are reported in Table 2.1 c) for the Yarqon river, Table 2.2 c) for the Brenton torrent, and Table 2.3 c) for the Desturo canal. The relevant simulated BTCs are presented in figures 2.4, 2.5 and 2.6, respectively. The results show the this modeling closure can well represent the breakthrough curve in the case of the Yarqon river and the Brenton torrent where the tails are relatively long. In these cases model optimization converges to the very similar values of the storage parameters of the first exponential retention component and dispersion coefficient, which turn out to be exactly the same for the Brenton torrent. This reassuring result indicates that, when the ratio of the timescales of two retention components is very high, the parameters of the first retention component are only weakly affected by the particular closure assumed for the second storage component, provided that this can approximate the experimental curve sufficiently well. Conversely, in the case of the Desturo canal the parameters of the first storage component, as well as the longitudinal dispersion coefficient, sensibly changes, and the timescale parameter of the hyporheic component becomes extremely low, with values of T_2 ranging from 0 to 0.15 s, indicating the absence of hyporheic transport. Analysis of the RMSE and visual inspection of the curve fits reveal that the combination of an exponential and a pumping RTD can still provide a good approximation of the breakthrough curves, but the resulting parameters lose physical sense, and there is an inversion of the expected behavior of the two storage components: the timescale of the first component increases to represent the long timescale processes whereas the pumping component turns out to represent the short term component. In the case of the Yarqon river and the Brenton torrent, the pumping RTD shows a scale dependent behavior of the relevant timescale, which increases from $T_2 = 297\,\mathrm{s}$ for $L = 816\,\mathrm{m}$ to

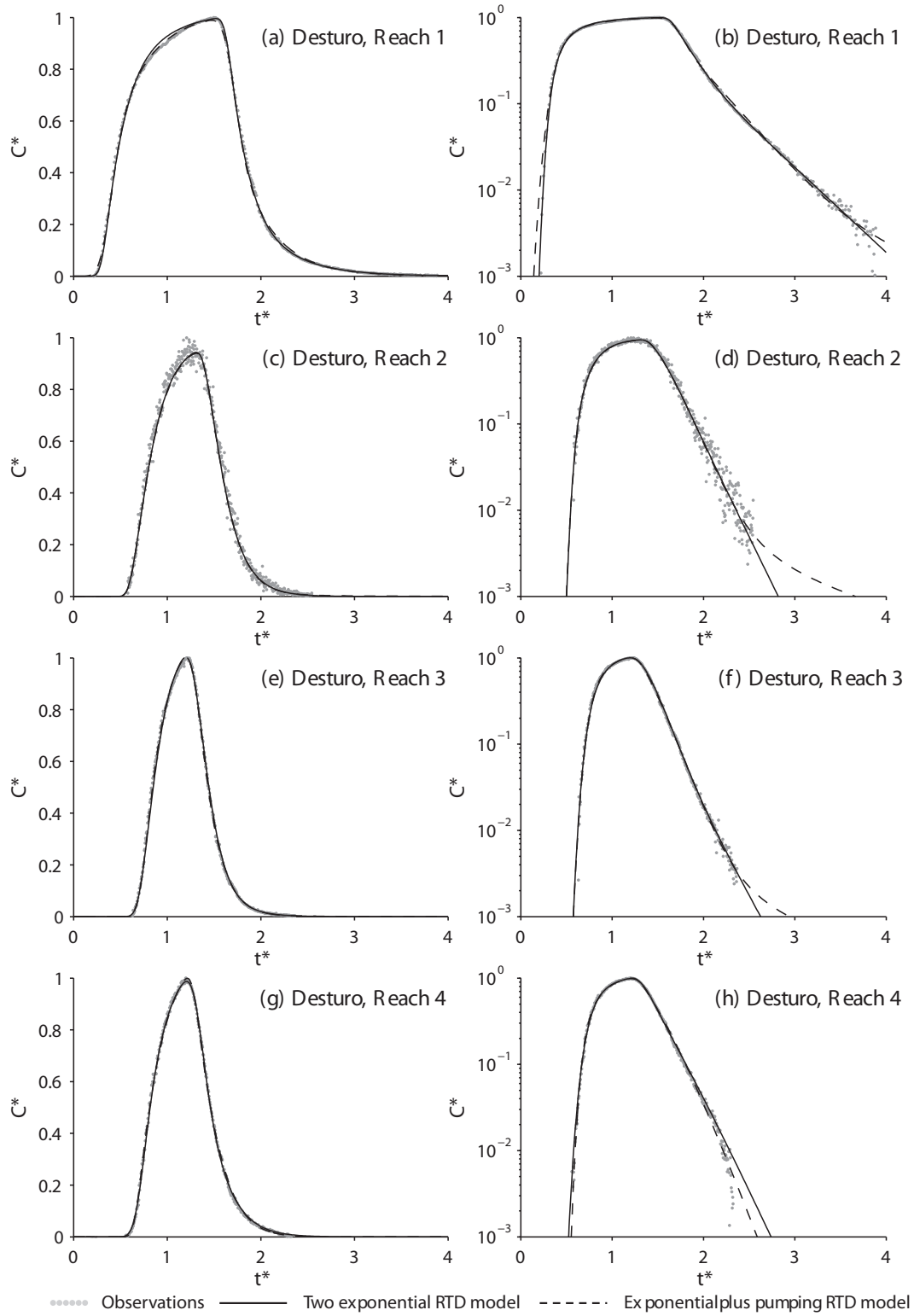

Figure 2.6. Observed and simulated breakthrough curves for the Desturo canal (left) in linear scale and (right) semi-log scale.

$T_2 = 3781\,\mathrm{s}$ for $L = 1887\,\mathrm{m}$ for the Yarqon river, and from $T_2 = 198\,\mathrm{s}$ for $L = 680\,\mathrm{m}$ to $T_2 = 474\,\mathrm{s}$ for $L = 2160\,\mathrm{m}$ for the Brenton torrent. As pointed out above, a similar behavior was observed for the two exponential RTD model. The dependence of the timescale on the length of the study reach might be related to the fact that longer reaches implies that longer transport paths become active, which in turn implies a lengthening of the tails of the breakthrough curves. The assumption of a power-law RTD as the one associated to pumping derived by Elliott and Brooks does not make the problem independent of the length scale of the study reach. The intervals of variability in which "similar" fits can be obtained using the exponential plus pumping RTD modeling closure is found to be less than 21% of the optimal parameter values for the Yarqon river and the Brenton torrent. A higher uncertainty is found in the case of the Desturo canal, which is linked to the inadequacy of the pumping RTD to represent the tails of the break-through curves.

Reach	1	2	3	4
(a) Study reaches				
L (m)	262	305	336	278
Q ($m^3 s^{-1}$)	0.045	0.045	0.053	0.042
A (m^2)	0.19	0.21	0.36	0.31
t_{ad} (s)	1114	1440	2329	2040
r_M (s)	0.88	0.83	0.86	0.84
(b) Parameters of STIR model with two exponential RTDs				
K ($m^2 s^{-1}$)	0.10 ± 0.007	0.14 ± 0.01	0.09 ± 0.007	0.10 ± 0.008
α_1 ($\times 10^{-4} s^{-1}$)	13.5 ± 0.4	10.1 ± 0.6	11.0 ± 0.3	11.0 ± 0.9
α_2 ($\times 10^{-4} s^{-1}$)	2.73 ± 0.11	1.50 ± 0.13	0.07 ± 0.06	4.27 ± 0.35
T_1 (s)	99 ± 5	171 ± 10	140 ± 5	60 ± 5
T_2 (s)	367 ± 19	365 ± 16	397 ± 16	280 ± 11
RMSE[a] ($\times 10^{-2}$)	2.02	5.40	1.96	4.29
(c) Parameters of STIR model with exponential plus pumping RTD				
K ($m^2 s^{-1}$)	0.27 ± 0.04	0.18 ± 0.04	0.11 ± 0.01	0.06 ± 0.007
α_1 ($\times 10^{-4} s^{-1}$)	4.94 ± 0.29	7.52 ± 0.68	5.77 ± 0.26	8.79 ± 0.14
α_2 ($\times 10^{-4} s^{-1}$)	3225 ± 622	145 ± 31	8686 ± 1859	0
T_1 (s)	291 ± 8	237 ± 15	215 ± 3	218 ± 5
T_2 (s)	0.0077 ± 0.0015	0.13 ± 0.03	0.0015 ± 0.0005	—
RMSE[a] ($\times 10^{-2}$)	2.22	5.37	1.74	3.24

[a] The parameter RMSE is unitless.

Table 2.3. Summary of test and model parameters for the Desturo canal. Values of optimized parameters are reported as the intervals for which model optimization produces an RMSE differing by less than 5% from the global optimum value. The RMSE reported in the table corresponds to the global optimum.

2.6 Implications and findings

The results presented here show that the use of two storage components in a multi-domain solute transport model does not lead to an over-parameterization of transient storage. In the recent years, a few works (*Gooseff et al.*, 2007; *Haggerty and Wondzell*, 2002) discussed the application of exponential and power-law RTD models to represent tracer BTCs in natural streams. Those works showed that a power-law RTD can sometimes represent the observed RTDs and be a better alternative to an exponential RTD transient storage model. Yet a clear physical explanation for the power-law RTD has not been given. The pumping RTD used here is asymptotically a power-law and was derived analytically by *Elliott and Brooks* (1997a) for the case of bedform-induced hyporheic exchange, under a few simplifying assumptions. The results of this work show that this particular form of the RTD can provide a good representation of the observed BTCs, but only in streams where hyporheic exchange is an important storage component. This evidence suggests that tracer BTCs can embed signatures of specific storage processes which can be identified by inverse modeling. It is further shown that a two-exponential RTD can provide a good alternative to the exponential plus pumping RTD model, giving an excellent curve fit in all the cases considered. Interestingly, when there is significant hyporheic exchange, the first storage component appears to be only marginally affected by the choice of exponential RTD instead of a pumping RTD for the second storage zone. We feel that the different behavior of a pumping RTD compared to exponential RTD for the long term transient storage may become visible if longer tails of the BTCs were available. However, it is apparent from this work that typical tracer BTCs do not contain enough information at long time scales to discriminate the validity of either assumptions. It is unlikely that field tracer tests could ever be improved to such extent due to the presence of background noise, and turbidity and temperature fluctuations.

This may be an interesting point for future research performed in very well controlled laboratory experiments using instruments with high resolution. With the only exception of two of the study reaches analyzed, a single exponential RTD model, as the TSM, is unable to fully represent the experimental data if we minimize the difference between model simulations and data using a combination of linear scale for the bulk of the BTC, and log-scale for the tails. The use of a single exponential RTD model may therefore underestimate the long-time component associated to hyporheic flows. The use of a transient storage modeling closure derived by physical modeling of hyporheic exchange can in principle provide an estimate of the volume interested by solute penetration. As pointed out by *Gooseff et al.* (2003), the influence of hyporheic exchange on stream nutrient cycles is determined by the time-rate of nutrient transformations. Long hyporheic residence times are not necessary to support biogeochemical processes occurring at fast rates, such as nitrification and uptake of soluble reactive phosphorous, but may have an important impact on mineralization of dissolved organic carbon (DOC) and nitrogen (DON), which can occur over timescales of days to weeks.

2.7 Conclusions

In this study a multiple domain general residence time solute transport model has been applied to tracer tests data from different streams. The analysis has shown that streams are characterized by different responses to a solute injection, revealed by model parameters. Two distinct forms of the residence time distribution in the storage domains have been considered. These modeling closures can be considered as double domain closures assuming a first domain to be associated to short timescale retention and the second one to long term retention. In both models the first storage domain is associated to an exponential residence time distribution. The second storage component is represented in the two models with another exponential distribution and with a power law distri-

bution derived by theoretical modeling of bed form induced hyporheic exchange, respectively. In streams where hyporheic exchange is a significant retention component calibration of the model assuming two exponential RTDs yields relatively high retention timescales of the second storage domain and a relatively high ratio between the timescales of slow and fast exchange. In that case a model assuming the second storage component to be represented by the RTD derived by *Elliott and Brooks* (1997a) for pumping exchange due to bed forms provides an equivalently good approximation of the observed breakthrough curves. The fitting procedure, based on a global optimization algorithm, converges to the same values of the dispersion coefficient and of the parameters of the first exponential retention component. The observed stability of the model parameters allows for a direct comparison of the model results for the two different modeling closures. Conversely, when modeling closure assuming an exponential and a pumping RTD is applied to streams where hyporheic exchange is limited, the model fails to properly represent the observed breakthrough curves. Furthermore the model parameters change in such a way the that results between the two different transient storage modeling closures are difficult to compare, and uncertainty arises about the interpretation of the model parameters since the observations are not well reproduced. In both models the timescales of retention are found to be dependent on the length scale of the study reach, which points out that a more comprehensive approach is still needed to properly compare retention properties of different study reaches. Overall, the results show that a multiple domain solute transÂňport model like STIR can be used to characterize river transient storage processes in terms of average retention times, and demonstrate that streams that are very different in terms of channel size, substrate material and presence of submerged vegetation, show also distinct retention patterns.

Chapter 3

Bimodality of wetland residence time distributions and their modeling[1]

3.1 Introduction

Vegetation plays a major role in controlling the fate of contaminants in natural and constructed wetland. Accurate estimates of the contaminant removal efficiency of a wetland require separate knowledge of the residence time statistics in the main flow channels, where the flow velocity is relatively higher, and in the more densely vegetated zones, where the velocity is smaller and most of the biochemical transformations occur. A conceptual wetland characterized by a main flow channel (MFC) and lateral vegetated zones (LVZs) is modeled here using a two-dimensional depth-averaged hydrodynamic and advection-dispersion model. The overall effect of vegetation is described as a flow resistance represented in the hydrodynamic model as a function of the stem density.

The removal efficiency of natural and constructed wetlands is controlled by the time spent by contaminants in the vegetated zones (*Persson et al.*, 1999). Veg-

[1] The contents of this chapter are described in: T. Musner, A. Bottacin-Busolin, M. Zaramella, A. Marion, A contaminant transport model for wetlands accounting for distinct residence time bimodality, *Ecological Engineering* (submitted)

etation plays an important role for two main reasons: first, dense vegetated zones locally decrease the flow velocity, creating stagnant zones and favoring the sedimentation of suspended solids; second, plant roots and associated epiphytic biofilms are responsible for the transformation of the transported substances as a result of biochemical processes. Vegetation, in combination with the wetland topography, can also produce hydraulic shortcuts that can substantially decrease the overall efficiency of a wetland.

Constructed wetlands for waste water treatment are often designed with reference to an average water residence time (*Kadlec and Wallace*, 2009), but this can lead to significant inaccuracies in the estimation of the wetland efficiency (*Kadlec*, 2000). Zero-dimensional models are often used because of their simplicity, but they are inadequate to represent complex spatial patterns resulting from heterogeneous vegetation distributions, which significantly affects the contaminant removal of a wetland (*Akratos and Tsihrintzis*, 2007; *Kadlec and Wallace*, 2009). One-dimensional transient storage models have been widely used to represent the transport and retention dynamics in rivers due to vegetation and permeable beds (*Runkel and Broshears*, 1991; *Bencala and Walters*, 1983; *Gooseff et al.*, 2003), but a major question is whether these models can represent the more complex hydrodynamics found in natural and constructed wetlands. Recent studies (*Keefe et al.*, 2004; *Martinez and Wise*, 2003) have used transient storage models to assess the contaminant removal in constructed wetlands providing in some cases a good approximation of the breakthrough curves. However, these models fail to describe in general the different flow paths through vegetation and the main flow channels, which can result in a clear bimodality of the solute breakthrough curves. A bimodal behavior of the hydraulic residence time distributions (RTDs) induced by riparian vegetation has been experimentally observed in a real wetland by *Martinez and Wise* (2003) and in a conceptualized lowland river by *Perucca et al.* (2009).

Since spatial heterogeneity plays a fundamental role in controlling the fate of contaminants, a two-dimensional approach is more appropriate to describe transport dynamics in wetlands. Although two-dimensional hydrodynamic models have already been used in the past (*Persson et al.*, 1999; *Somes et al.*, 1999), the formulation of more detailed models accounting for vegetation distribution is relatively recent (*Arega and Sanders*, 2004; *Jenkins and Greenway*, 2005). However, the use of these models do not display a clear relationship between vegetation density and hydraulic RTDs.

Following *Jenkins and Greenway* (2005), a two-dimensional depth-averaged model is applied here to a conceptual wetland characterized by a central main flow channel (MFC) and lateral vegetated zones (LVZs). Contaminant transport simulations are performed for different vegetation densities to analyze the effect on the hydraulic RTDs of the degree of channelization of a wetland. A one-dimensional transport model is proposed and calibrated against the RTDs derived with the two-dimensional depth-averaged model. The behavior of the model parameters is then analyzed as a function of the system parameters and analytical relationships are provided for the average residence times and flow discharges in the MFC and in the LVZs.

3.2 2-D depth-averaged model

If the vertical gradients are sufficiently small compared to the horizontal gradients, the transport of a substance in a wetland can be well represented by a two-dimensional, depth-averaged model. Such a model can account for horizontal variations of flow resistance associated with different vegetation densities, and can be used to describe mass and momentum exchanges between main flow channels and vegetated zones.

3.2.1 Hydrodynamic model

Under the assumption of hydrostatic pressure, steady-state flow, negligible wind and Coriolis forces, the depth-averaged velocity field and water depth satisfy the following equations (*Wu*, 2007):

$$\frac{\partial(hU)}{\partial x} + \frac{\partial(hV)}{\partial y} = 0 \tag{3.1}$$

$$\frac{\partial(hU^2)}{\partial x} + \frac{\partial(hUV)}{\partial y} = -gh\frac{\partial z_s}{\partial x} - \frac{\tau_x^b}{\rho} - \frac{\tau_x^v}{\rho} \tag{3.2}$$

$$\frac{\partial(hUV)}{\partial x} + \frac{\partial(hV^2)}{\partial y} = -gh\frac{\partial z_s}{\partial y} - \frac{\tau_y^b}{\rho} - \frac{\tau_y^v}{\rho} \tag{3.3}$$

The quantities U and V represent the depth-averaged velocities [$\mathrm{L\,T^{-1}}$] in the x- and y- directions, respectively, h is the water depth, z_s is the water surface elevation [L], and ρ the water density [$\mathrm{ML^{-3}}$]. The shear stresses τ_x^b and τ_y^b account for bed resistance, whereas τ_x^v and τ_y^v account for vegetation resistance along the x- and y- direction, respectively. Equation (3.2) and equation (3.3) assume that Reynolds stresses are negligible compared to bed and vegetative resistance. In channelized wetlands, *Babarutsi et al.* (1989) experimentally showed that bed friction dominates and Reynolds stresses can be neglected when $c_D^b\, L_h/h > 0.1$, where L_h is the the horizontal length scale of recirculation zones. Since typical values of c_D^b vary between 0.009 and 0.003 in tidal wetlands, this model is expected to resolve recirculation zones where $L_h/h >$ 10–30 (see *Arega and Sanders*, 2004).

The contribution of bed friction to bed shear stresses is computed by adapting the one-dimensional relationships proposed by *Kadlec* (1990) to a two-dimensional velocity field, which leads to:

$$\tau_x^b = \rho c_D^b U\sqrt{U^2 + V^2} \tag{3.4}$$

$$\tau_y^b = \rho c_D^b V \sqrt{U^2 + V^2} \tag{3.5}$$

The bed drag coefficient c_D^b [−] in equation (3.4) and equation (3.5) combines both laminar and turbulent stresses, and can be calculated as follows (*Kadlec*, 1990):

$$c_D^b = \frac{3\nu}{h\sqrt{U^2 + V^2}} + f^2 g h^{-1/3} = \frac{3}{Re_h} + f^2 g h^{-1/3} \tag{3.6}$$

where ν is the kinematic viscosity [$\mathrm{L^2\,T^{-1}}$] and f is the Manning's friction coefficient [$\mathrm{T\,L^{-1/3}}$]. For depth-Reynolds numbers Re_h less than 500 the first term prevails, whereas the second term prevails for depth-Reynolds numbers greater than 12 500 (*Kadlec*, 1990). The sum of the two terms therefore provides a complete description of the bed shear stresses for a wide range of depth-Reynolds numbers.

Vegetation drag is modeled in a similar way by representing aquatic plant stems as an array of randomly distributed cylinders with a uniform diameter d [L], as suggested by *Kadlec* (1990) and by *Arega and Sanders* (2004):

$$\tau_x^v = \frac{1}{2}\rho c_D^v n l d U \sqrt{U^2 + V^2} \tag{3.7}$$

$$\tau_y^v = \frac{1}{2}\rho c_D^v n l d V \sqrt{U^2 + V^2} \tag{3.8}$$

where n is the superficial stem density [$\mathrm{L^{-2}}$], l is the submerged stem length [L] and c_D^v is the vegetation drag coefficient. For fully emergent vegetation, as considered in this work, the submerged stem length can be taken as the water depth. The behavior of the vegetation drag coefficient for an individual cylinder is well known (*Bennett and Myers*, 1962; *White*, 1991) and shows a decreasing trend for increasing stem Reynolds numbers, defined as $Re_d = \sqrt{U^2 + V^2}\, d/\nu$. Other studies (*Ergun*, 1952; *Petryk*, 1969; *Nepf*, 1999; *Hill et al.*, 2001; *Blevins*, 2005) have shown that neighboring cylinders can produce a velocity reduction and, as a con-

sequence, a reduced drag (*Tanino and Nepf*, 2008). Nevertheless, cumulative effects of multiple wake interactions can be neglected for sufficiently sparse vegetation, i.e. when the solid volume fraction ad is lower than 0.1 (*Raupach*, 1992). Here, the parameter a represents the frontal area of vegetation per unit volume [L^{-1}], and can be written as a function of the superficial stem density, $a = nd$, if the plants are modeled as cylinders.

Nepf (1999) performed numerical and laboratory experiments for superficial stem densities lower than 2500 stems/m^2 and a stem diameter of 2 mm, corresponding to a solid volume fraction $ad = nd^2 \approx 0.01$, and found relatively constant values of c_D^v. Such values are common in natural and constructed wetlands. *Tanner* (2001) measured the superficial density of vegetation in pilot-scale constructed wetlands and found 1400–1500 stems/m^2 of *Schoenoplectus Tabernaemontani* and densities higher than 2000 stems/m^2 of *Schoenoplectus Validus*. *Hocking* (1989) and *Parr* (1990) found superficial vegetation densities of *Phragmites Australis* ranging from 70 to 250 stems/m^2. Other hydraulic studies on diffusion in emergent vegetation (*Nepf et al.*, 1997) and vegetation drag (*Hall and Freeman*, 1994) used densities ranging between 200–2000 stems/m^2 and 400–800 stems/m^2. In this study, a vegetation density in the range between 50 and 800 stems/m^2 is considered, for which the vegetation drag coefficient depends only on the stem Reynolds number, Re_d. A continuous range of Re_d was modeled using the relationship proposed by *Kadlec* (1990). This relationship is based on laboratory tests performed by *Wieselberger* (1921) for laminar flows, and *Tritton* (1959) for turbulent flows. Kadlec's formulation, similar to the one proposed by *White* (1991), is given as follows:

$$c_D^v = \frac{10\mu}{\rho d\sqrt{U^2+V^2}} + 1 = \frac{10}{Re_d} + 1 = \frac{10}{Re_h}\frac{h}{d} + 1 \tag{3.9}$$

3.2.2 Solute transport model

Solute transport of a passive tracer through a wetland is simulated with a depth-averaged solute transport model,

$$\frac{\partial(hC)}{\partial t} + \frac{\partial(hUC)}{\partial x} + \frac{\partial(hVC)}{\partial y} = \frac{\partial}{\partial x}(hE_{xx}\frac{\partial C}{\partial x} + hE_{xy}\frac{\partial C}{\partial y}) + \frac{\partial}{\partial y}(hE_{yx}\frac{\partial C}{\partial x} + hE_{yy}\frac{\partial C}{\partial y}) \tag{3.10}$$

where C is the depth-averaged solute concentration [ML^{-3}], U, V are the vertically integrated velocity components [LT^{-1}] in the x-, y-directions respectively. The coefficients $E_{i,j}$ [$\mathrm{L}^2\mathrm{T}^{-1}$], $i,j = x,y$, account for both turbulent diffusion and shear dispersion due to vertical velocity gradients. *Nepf* (1999) proposed the following relationship for the transverse diffusivity:

$$\frac{E_T}{Ud} = \alpha_T[c_D^v ad]^{1/3} + \frac{\beta^2}{2}ad \tag{3.11}$$

In equation (3.11), the first term represents the turbulent diffusivity, whilst the second term represents the effect of mechanical dispersion through emergent vegetation. The coefficient $\alpha_T = 0.81$ [–], derived by *Nepf* (1999) from experimental data, accounts for horizontal turbulent diffusion, whereas the coefficient $\beta = 1$ [–] represents a scale factor that accounts for the transverse motion of a solute particle through stems along a characteristic distance $\Delta y = \beta d$. The turbulent diffusivity is based on the assumption that all the energy extracted from the mean flow through stems is converted into turbulent kinetic energy. This assumption is valid for $Re_d < 200$, when the effect of viscous drag is significant. As experimentally confirmed by *Nepf* (1999), for sufficiently small stem densities, $ad < 0.01$, mechanical dispersion is small compared to turbulent diffusion and the second term can be neglected. Experimental tests performed with stem Reynolds numbers in the range between 90 and 2000 (typical value $\approx 200-300$) show that this is not the case for the lower end of the range, where mechani-

cal diffusion dominates. However, *Lightbody and Nepf* (2006) used this assumption as a first approximation to determine the longitudinal dispersion coefficient E_L using field velocity measurements in the range between 0.1 and 0.24 cm s^{-1} (Re_d = 2–360). The proposed longitudinal dispersion coefficient is written as a combination of the stem-scale and the depth-scale dispersion process as follows:

$$\frac{E_L}{Ud} = \frac{1}{2} {c_D^v}^{3/2} + \frac{Uh}{D_z}\Gamma \tag{3.12}$$

where $D_z = \alpha_2[c_D^v ad]^{1/3} Ud$ is the vertical turbulent diffusion coefficient and Γ is the non-dimensional velocity shape factor. According to *Lightbody and Nepf* (2006) for the coefficient D_z, the value $\alpha_2 = 0.1$ was chosen to account for the vertical turbulent diffusion. The first term of equation (3.12) accounts for the stem-scale longitudinal dispersion process, whereas the second term accounts for the dispersion induced by vertical velocity gradients. As noted by *Lightbody and Nepf* (2006), the first term of equation (3.12) is typically much smaller than the second term, and can be neglected. For the range of stem Reynolds numbers investigated in this work it is reasonable to consider only the first term of equation (3.11) and only the second term of equation equation (3.12). These relationships were adapted for the two-dimensional model by expressing the dispersion tensor as in *Arega and Sanders* (2004):

$$E_{xx} = E_L + (E_L - E_T)\frac{U^2}{U^2 + V^2} \tag{3.13}$$

$$E_{xy} = E_{yx} = (E_L - E_T)\frac{UV}{U^2 + V^2} \tag{3.14}$$

$$E_{yy} = E_T + (E_L - E_T)\frac{V^2}{U^2 + V^2} \tag{3.15}$$

3.2.3 Residence time distributions

The physical and chemical transformations of dissolved solutes in a wetland depend on the time spent by a particle in the vegetated zones. The residence time of a solute particle can vary to a wide degree due to different flow paths, velocity gradients and hydraulic short-circuits (*Somes et al.*, 1999), making a statistical description in terms of probability distributions more appropriate for analyzing the problem (*Somes et al.*, 1999; *Kadlec and Wallace*, 2009). Hydraulic RTDs provide a measure of the variability of the detention time and can be a valuable tool for assessing the efficiency of contaminant removal. By using a two-dimensional depth-averaged hydrodynamic model in combination with a solute transport model, it is possible to numerically derive the RTDs as a function of the system variables. Other studies have used a similar approach to characterize the hydraulic response of a wetland (*Wörman and Kronnäs*, 2005).

The mass outflow, $\dot{M}$ [MT^{-1}], is given by the temporal convolution between the mass inflow, $\dot{M}_{\mathrm{in}}$, and the probability density function of the residence time, $\phi(t)$:

$$\dot{M}_{out} = (\phi * \dot{M}_{in})(t) = \int_0^t \phi(\tau)\dot{M}_{in}(t-\tau)\,\mathrm{d}\tau \tag{3.16}$$

In this work the expression "residence time distribution" (RTD) is used interchangeably to denote the probability density function of the residence time, $\phi(t)$. In general, the mass inflow $\dot{M}_{in}$ can be time-dependent, and can be written as the product of the input concentration $C_{in}(t)$ [ML^{-3}] and the inflow discharge $Q_{in}(t)$ [$\mathrm{L}^3\,\mathrm{T}^{-1}$], hence $\dot{M}_{\mathrm{in}} = C_{\mathrm{in}}(t)\,Q_{\mathrm{in}}(t)$. Under the assumption of steady-state flow, $Q_{in}(t) = \overline{Q}$ and assuming a constant concentration at the inlet, $\overline{C}_{in}$, equation (3.16) can be arranged in the form:

$$\frac{\dot{M}_{out}}{\overline{C}_{in}\overline{Q}} = \int_0^t \phi(\tau)\,\mathrm{d}\tau \tag{3.17}$$

The right hand side of equation (3.17) represents the cumulative distribution function of the wetland hydraulic residence time, denoted by $\Phi(t)$. Under steady flow conditions, the water inflow equals the water outflow, therefore $\dot{M}_{out} = C_{out}(t)\overline{Q}$. Equation (3.17) then becomes:

$$\frac{C_{out}(t)}{\overline{C}_{in}} = \int_0^t \phi(\tau)\,\mathrm{d}\tau = \Phi(t) \tag{3.18}$$

and hence:

$$\phi(t) = \frac{\mathrm{d}\Phi(t)}{\mathrm{d}t} = \frac{\mathrm{d}}{\mathrm{d}t}\left(\frac{C_{out}(t)}{\overline{C}_{in}}\right) \tag{3.19}$$

Equation (3.19) provides the link between solute breakthrough curves and RTDs. In particular, if a constant unitary concentration, $\overline{C}_{\mathrm{in}} = 1$, is imposed as a boundary condition at the inlet, the hydraulic RTD can be obtained by numerically differentiating the output concentration $C_{\mathrm{out}}(t)$ with respect to time.

3.2.4 Model application

The flow domain considered in this work is given by a rectangular wetland with length $L = 200$ m, width $B = 50$ m, and constant bed elevation. The choice of a zero bed slope is supported by the evidence that in many natural wetlands the bed elevation does not vary significantly in the streamwise direction, and the effect of bed slope can often be neglected (*Wörman and Kronnäs*, 2005; *Wu*, 2007). The flow domain is characterized by a main flow channel surrounded by vegetated zones on both sides. The channel follows the center line of the wetlands and has a uniform breadth b. The wetland inlet and outlet coincide with the end sections of the main channel. Two different values of the channel width were considered in this work: $b = 5$ m and $b = 10$ m.

For the flow equations (3.1) and (3.3), the boundary conditions are given by the inflow at the inlet, $Q = 0.5\ \mathrm{m}^3\ \mathrm{s}^{-1}$, and the water depth at the outlet, $h = 0.5$ m. For the solute transport equation, the boundary conditions are given by a con-

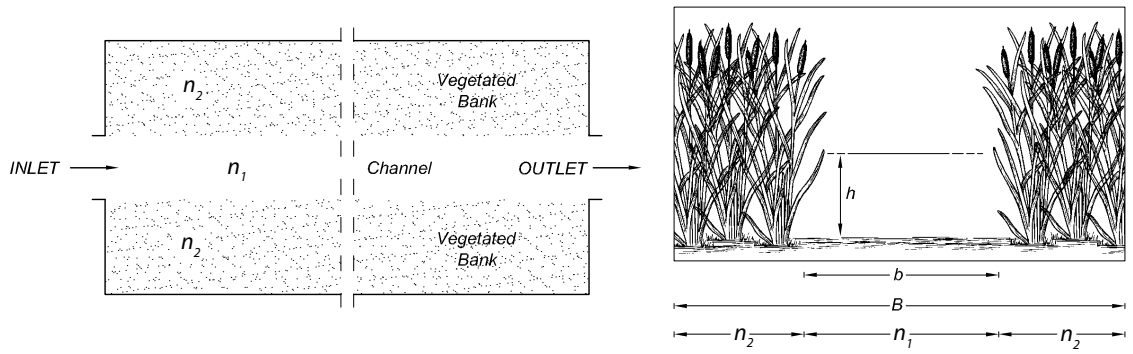

Figure 3.1. Illustration of the conceptual wetland analyzed in this work. A depth-averaged hydrodynamic model is applied to a rectangular flow domain with different vegetation densities in the main channel and in the lateral vegetated zones. The average vegetation density of the wetland is kept constant for all simulations and different combinations of discharge and main channel widths are investigated.

stant unitary concentration at the inlet, $C = 1\ \mathrm{kg\,m^3}$, an open boundary condition at the outlet, and the no-flux condition on the remaining part of the flow boundary. The equations are solved via a finite element method using COMSOL *Multiphysics*® with quadratic shape functions. The computational grid is made of approximately 150 000 triangular elements, with higher spatial resolution near the inlet and the outlet, and a maximum element size of 2 m.

Simulations of the hydraulic RTD are performed in three steps: first, the steady-state flow field is derived by solving the flow equations (3.1) and (3.3); second, the transport equation is solved using the previously calculated flow field until the concentration at the outlet becomes constant; finally, the average concentration at the outlet is calculated as a function of time, and the hydraulic RTD is derived by numerical differentiation of the output concentration according to equation (3.19).

A uniform value of the Manning's roughness coefficient $f = 0.02\ \mathrm{m^{-1/3}\ s}$ (usually associated with clean earth) was assumed to represent the bottom flow re-

sistance, whereas a sequence of increasing vegetation densities were imposed for the vegetative resistance. No friction was considered on the lateral walls of the wetland domain.

In the simulations, the average vegetation density of the whole wetland,

$$\bar{n} = \frac{n_2(B-b) + n_1 b}{B} \tag{3.20}$$

was kept constant and equal to 650 stems/m^2. In equation (3.20), B denotes the wetland width, b is the MFC width and n_i, $i = 1, 2$, are the vegetation densities in the MFC and the LVZs, respectively. Starting from an initial homogeneous configuration with $n_1 = n_2 = \overline{n}$, a sequence of decreasing vegetation densities was imposed in the main channel, varying from $n_1 = 650$ stems/m^2 down to 50 stems/m^2. The resulting vegetation density in the lateral zones was then calculated from equation (3.20) by keeping $\overline{n}$ constant and solving for n_2. This allowed to analyze the statistics of the residence time for a range of degrees of channelization while keeping the average vegetation density as constant. Ten density ratios $n^* = n_1/n_2$ were considered for each width ratio $b^* = b/B$. Note that the parameter n^* represents the degree of uniformity of the vegetation density in the wetland, which increases as the degree of channelization decreases, and is equal to 1 when the vegetation density in the MFC is the same as in the LVZs. In this case, there is no real distinction between MFC and LVZs.

3.3 1-D solute transport model

In the two-dimensional model presented in the previous section, the hydraulic RTDs are determined in three steps: first, the 2-D depth-averaged flow equations are solved to derive the steady-state velocity field; second, the 2-D depth-averaged transport equation is solved for a continuous input resulting in a concentration field as a function of time; finally, the RTD is derived by calculating the

derivative of the average concentration at the outlet according to equation (3.19). The complexity of such a modeling process can be substantially reduced if a parameterization of the RTDs is available in which the model parameters can be linked to physical characteristics of the system. One-dimensional models are generally easier to calibrate and more suitable for inverse-modeling using tracer tests (e.g. *Keefe et al.*, 2004), especially when a closed-form solution of the underlying 1-D equations can be derived analytically. Here, a parameterization of the hydraulic RTDs is presented based on the one-dimensional residence time formulation proposed by *Marion and Zaramella* (2005) and *Marion et al.* (2008).

In order to represent the effect of the differential transport in the MFC and the LVZs, the overall RTD is expressed as a weighted sum of two residence time distributions individually describing the residence time statistics in the MFC and in the LVZs. The overall RTD in a wetland segment of length x is therefore written as follows:

$$\phi(t;x) = w_1 r_1(t;x) + (1 - w_1) r_2(t;x) \tag{3.21}$$

where w_1 is a weight parameter [–] and r_1 and r_2 are the hydraulic residence time distributions in the MFC and in the LVZs, respectively. In the model application presented in this work the variable x is replaced by the longitudinal extension of the wetland, L, since the focus of the analysis is on the residence time statistics in the whole wetland. However, the dependence on the coordinate x is maintained in equation (3.21) for sake of generality and to preserve the one-dimensional structure of the STIR formulation (*Marion et al.*, 2008).

The functional form of the individual RTDs, r_1 and r_2, is derived from the solution of the advection-dispersion equation for a mass pulse at $x = 0$, and is given by:

$$r_i(t;x) = \frac{x}{\sqrt{4\pi K_i t^3}} \exp\left[-\frac{(x - U_i t)^2}{4K_i t}\right] \tag{3.22}$$

where the subscript i takes the value 1 for the MFC, and 2 for the LVZs.

The model defined by equation (3.21) and equation (3.22) depends on five parameters characterizing the transport dynamics of a passive tracer in a channelized wetland, namely, the average flow velocities U_1 and U_2, the longitudinal dispersion coefficients, K_1 and K_2, and the weight parameter w_1. If the flow discharges are denoted by Q_1 and Q_2 and the flow cross-sectional areas are denoted by A_1 and A_2, then $U_1 = Q_1/A_1$ and $U_2 = Q_2/A_2$. The weight factor w_1 can then be calculated as the fraction of the total discharge flowing through the main channel, $w_1 = Q_1/Q$, where $Q = Q_1 + Q_2$ is the total discharge.

The above-described model was implemented as an extension of the software STIR, which provides an extendable modeling framework and a set of optimization routines for model calibration[2]. This particular extension is referred to as STIR-DTD, where the acronym DTD stands for Double Transport Domain. Although in this study the transport dynamics in the MFC and in the LVZs is represented as a purely advection-dispersion process, the software allows to incorporate additional retention processes via specific RTDs.

The capability of the model to reproduce the observed RTDs was analyzed by calibrating the model against the results of the two-dimensional simulations. The RTDs resulting from equation (3.21) and equation (3.22) were fitted to the RTDs generated according to Section § 3.2.3 and the behavior of the parameters was analyzed as a function of the degree of channelization. The calibration parameters are given by the velocities U_1, U_2, and the dispersion coefficients K_1 and K_2, whereas the weight factor w_1 was imposed using the definition $w_1 = Q_1/Q$ and the flow discharge Q_1 calculated from the hydrodynamic model.

Whilst the parameter calibration procedure provides a way to assess the suitability of the functional form equations (3.21) and (3.22) to represent the numerically simulated RTDs, a direct modeling approach may be preferable in predictive studies even if a certain degree of approximation is involved. Here, an ap-

[2]The software is available for download at `www.wetengineering.com`.

proximate relationship is derived for the discharges Q_1 and Q_2 that can be used to calculate the parameters U_1, U_2 and w_1. The relationship is based on Manning's equation, $U = f_{eq}^{-1} R_h^{2/3} S^{1/2}$, in which R_h is the hydraulic radius [L], S the slope of the energy line [–], and f_{eq} is an equivalent roughness coefficient representing the flow resistance due to vegetation and bed friction. The Manning's roughness coefficient, f_{eq}, is linked to the sum of the bed and vegetation shear stress, τ, by the relationship

$$f_{eq} = \frac{1}{U} R_h^{2/3} \left(\frac{\tau}{\gamma R_h} \right)^{1/2} = \frac{1}{U} R_h^{1/6} \left(\frac{\tau}{\gamma} \right)^{1/2} \tag{3.23}$$

where the equation $\tau = \gamma R_h S$ was used to link the total shear stress to the energy slope, S. If the hydraulic radius is approximated with the water depth, h, the equivalent Manning's roughness coefficient for fully emergent vegetation becomes:

$$f_{eq} = \frac{1}{g^{1/2}} \left(f^2 g + \frac{3\nu h^{-2/3}}{U} + \frac{5\nu h^{4/3}}{U} n + \frac{d h^{4/3}}{2} n \right)^{1/2} \tag{3.24}$$

The first two terms of equation (3.24) are associated with the bed roughness, whereas the last two terms represent the contribution to the shear stress due to vegetation. Under the flow conditions analyzed in this work, the first two terms are generally much smaller than the others. Also, with exception for the lower end of the range of Reynolds numbers, the third term can be considered small compared to the fourth. Under these assumptions, the equivalent Manning's roughness coefficient can be written as

$$f_{eq} = \left(\frac{d h^{4/3}}{2g} n \right)^{1/2} \tag{3.25}$$

Since $Q = Q_1 + Q_2$, it follows that:

$$\frac{Q_2}{Q} = \left(1 + \frac{Q_1}{Q_2} \right)^{-1} \tag{3.26}$$

$$\frac{Q_1}{Q} = 1 - \left(1 + \frac{Q_1}{Q_2}\right)^{-1} \tag{3.27}$$

Assuming that the energy slope S is the same in the MFC and in the LVZ, the ratio Q_1/Q_2 can be expressed using Manning's equation combined with equation (3.25):

$$\frac{Q_1}{Q_2} = \frac{f_{eq_2}}{f_{eq_1}} \frac{A_1}{A_2} \left(\frac{R_{h_1}}{R_{h_2}}\right)^{2/3} = \left(\frac{n_2}{n_1}\right)^{1/2} \frac{b}{B-b} = \frac{1}{\sqrt{n^*}} \frac{b^*}{1-b^*} \tag{3.28}$$

Finally, replacing equation (3.28) in equation (3.26) and equation (3.27) yields:

$$\frac{Q_2}{Q} = \left(1 + \frac{1}{\sqrt{n^*}} \frac{b^*}{1-b^*}\right)^{-1} \tag{3.29}$$

$$\frac{Q_1}{Q} = w_1 = 1 - \left(1 + \frac{1}{\sqrt{n^*}} \frac{b^*}{1-b^*}\right)^{-1} \tag{3.30}$$

Equation (3.29) and equation (3.30) provide a relationship between the non-dimensional discharges, Q_1/Q and Q_2/Q, the vegetation density ratio, n^*, and the non-dimensional channel width, b^*. The equations can be used to calculate the weight $w_1 = Q_1/Q$, and the velocities $U_1 = Q_1/(bH)$ and $U_2 = Q_2/H(B-b)$, where H is the average water depth. In the following section, the results of the model calibration and the two-dimensional simulations are compared with the predictions from (equation (3.29), equation (3.30)), and an attempt is made to clarify the parametric dependence of the dispersion coefficients K_1, K_2 as a function of the density ratio, n^*.

3.4 Results and discussion

Figure 3.2 shows the effect of different vegetation densities on the velocity field. For a homogeneous roughness distribution, the velocity profile becomes approximately uniform at a distance of 20–25 m from the wetland inlet. The most significant velocity gradients are located in proximity of the inlet and the outlet section,

with higher velocities in the center line and significantly smaller velocities at the corners (Figure 3.2a).

As the difference between stem density in the main channel and in the lateral banks increases, the flow is increasingly confined in the main channel and a first evidence of the bimodal behavior appears in the RTD (Figure 3.2b). In the most channelized case (Figure 3.2c), the hydraulic RTD shows an evident bimodality, indicating that mass transport is characterized by two distinct time scales associated with the transport in the main flow channel (MFC) and in the lateral vegetated zones (LVZs). The development of a clear bimodality as n^* decreases supports the decomposition of the overall RTD into two components according to equation (3.21).

A comparison of the RTDs is presented in Figure 3.3 for a constant flow discharge $Q = 0.5$ m^3 s^{-1} and for two different values of the parameter $b^* = b/B$. In the figure, the residence time is normalized by the mean hydraulic residence time in the wetland, defined as $T_R = BLH/Q$, where H is the average water depth [L] and L is the wetland length [L]. When the RTDs are plotted in a semilogarithmic scale, it becomes apparent that the RTDs decay exponentially and the slope of the tails depends on the ratio of vegetation density, n^*. As n^* decreases, the slope of the tails decreases and the distributions resemble more closely the solution of a conventional advection-dispersion equation. The shape of the RTDs is also affected by the width of the main channel. For a larger width, $b^* = 0.2$, the RTDs decay more slowly than for $b^* = 0.1$, indicating a slower transport in the LVZs. Also, for $b^* = 0.2$ the peak of the faster component is higher than for $b^* = 0.1$, due to the higher discharge in the MFC.

As the ratio $n^* = n_1/n_2$ decreases, the mean velocity in the lateral vegetated zones decreases whereas the mean velocity in the main channel increases. This behavior is showed in Figure 3.6 and confirmed by the pattern of the mean residence times in each zone as a function of the density ratio, n^* (Table 3.1 and Table

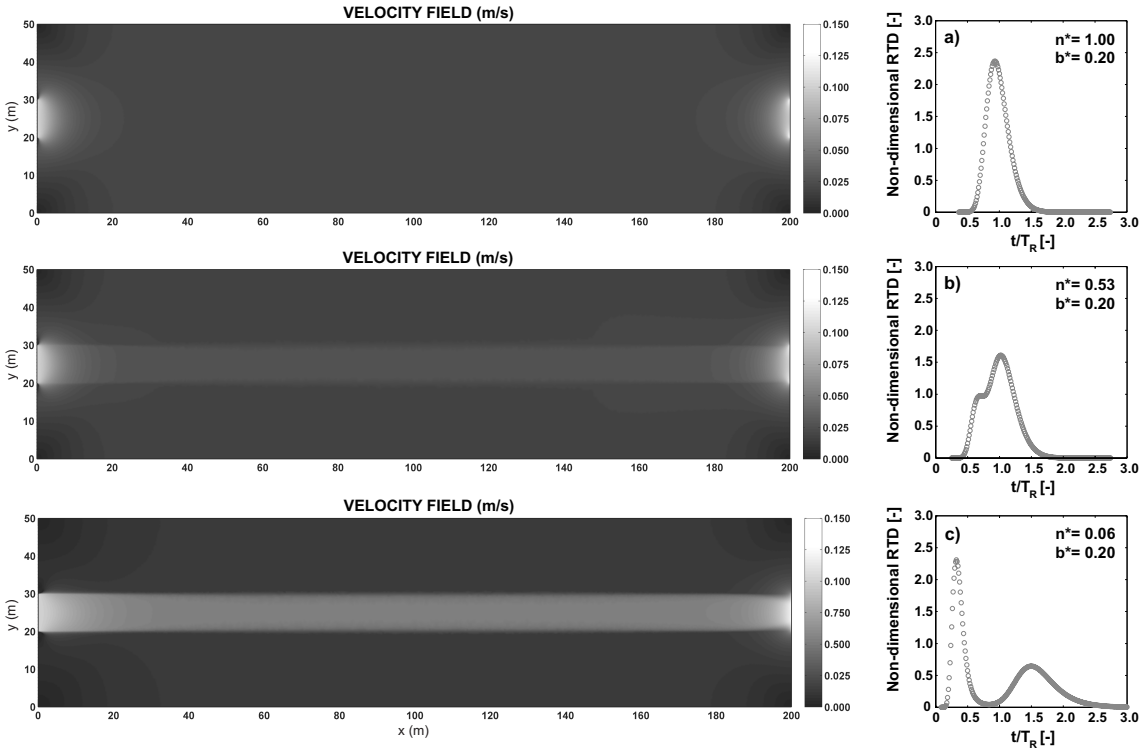

Figure 3.2. Comparison between three selected velocity fields for a flow discharge $Q = 0.5$ m^3 s^{-1} and a main channel width $b = 10$ m. Hydraulic residence time distributions (RTDs) are plotted in non-dimensional form using the average residence time $T_R = BLH/Q$ as a reference time scale. For a uniform vegetation distribution of 650 stems/m^2 (a), the flow velocity is almost uniformly distributed, with diverging and converging flow regions in proximity of the inlet and the outlet. In the intermediate case (b), with 717 stems/m^2 in the LVZs and 384 stems/m^2 in the MFC ($n^* \approx 0.53$), a slight bimodality becomes apparent: the velocity field is more channelized, with higher velocities in the main channel. In the third case (c), with 800 stems/m^2 in the VZs and 50 stems/m^2 in the MFC ($n^* \approx 0.06$), the residence time statistics is characterized by two distinct timescales, associated with the faster transport in the MFC and the slower transport in the LVZs, respectively. The result is a pronounced bimodality of the RTD.

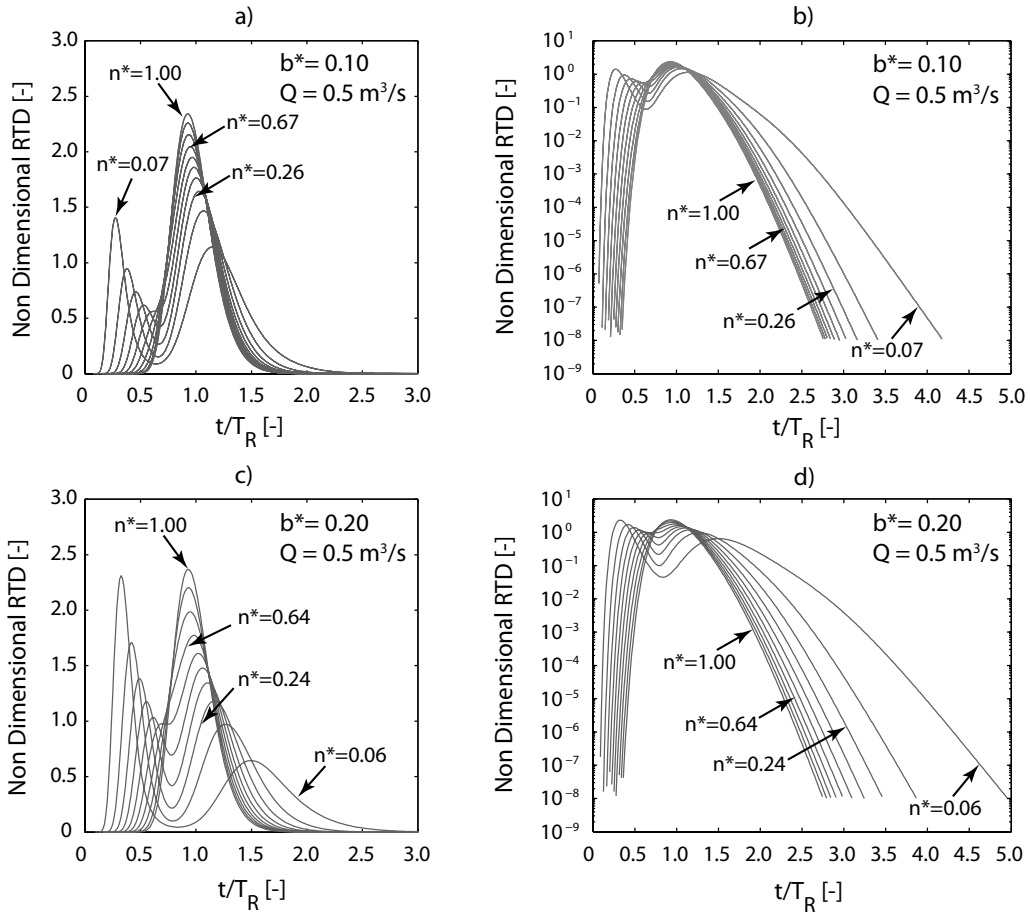

Figure 3.3. Comparison between non-dimensional hydraulic RTDs for a discharge of $Q = 0.5\ \mathrm{m^3 s^{-1}}$ and two MFC widths, $b = 5$ m (a) and $b = 10$ m (c). Curves are normalized by the average water residence time in the wetland, $T_R = BLH/Q$, and plotted in linear than in logarithmic scale. The logarithmic plot (b) and (d) shows a linear behavior of the curves at longer times.

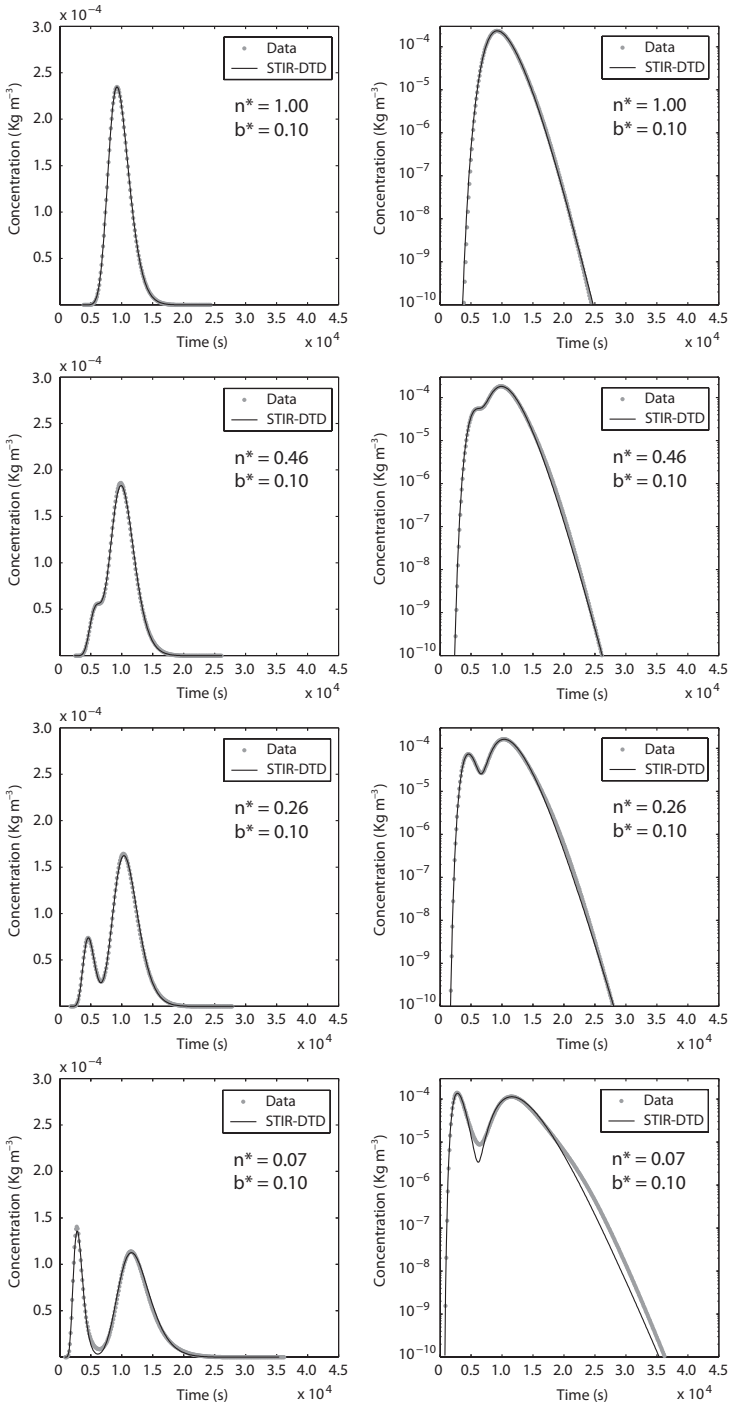

Figure 3.4. Comparison between the results from 2-D depth-averaged model and the 1-D transport model for $Q = 0.5$ m^{3}s^{-1} and $b = 5$ m.

Table 3.1. Best-fit model parameters for $Q = 0.5\,\mathrm{m^3\ s^{-1}}$ and main channel width $b = 5$ m.

n^* (-)	1.00	0.887	0.777	0.669	0.564	0.461	0.360	0.261	0.164	0.070
w_1 (-)	0.101	0.107	0.114	0.121	0.130	0.142	0.157	0.177	0.208	0.267
K_1 ($\times 10^{-2}$ m^2 s^{-1})	3.56	4.46	9.58	10.4	10.3	11.2	12.8	17.0	25.7	47.8
K_2 ($\times 10^{-2}$ m^2 s^{-1})	6.88	7.43	7.14	6.82	6.62	6.68	6.72	6.78	6.96	7.83
U_1 ($\times 10^{-2}$ m s^{-1})	2.25	2.20	2.35	2.67	2.96	3.25	3.61	4.08	4.83	6.41
U_2 ($\times 10^{-2}$ m s^{-1})	2.02	2.02	2.00	1.97	1.95	1.92	1.88	1.83	1.75	1.61
T_1 ($\times 10^3$ s)	8.90	9.11	8.50	7.48	6.76	6.15	5.55	4.91	4.14	3.12
T_2 ($\times 10^3$ s)	9.92	9.92	10.0	10.1	10.3	10.4	10.6	10.9	11.4	12.4
Pe_1 ($\times 10^4$)	2.10	2.17	2.27	2.40	2.54	2.72	2.96	3.29	3.85	5.15
Pe_2 ($\times 10^4$)	9.38	9.35	9.31	9.26	9.22	9.18	9.13	9.08	9.02	8.93

3.2). For decreasing values of n^* the time scale of transport in the MFC, $T_1 = L/U_1$, decreases and the time scale of the transport in the LVZs, $T_2 = L/U_2$, increases. The fraction $w_1 = Q_1/Q$ of the total discharge flowing through the main channel, calculated in the central region of the domain where the flow is not affected by inlet and outlet effects, is shown in Table 3.1 and Table 3.2.

The value of w_1 for a channel width $b = 5$ m is approximately double the value for $b = 10$ m, whereas $w_1 = 1$ for the limit case of $b = B$. Figure 3.4 shows a comparison between the breakthrough curves generated with the 2-D model and the curves generated with the calibrated one-dimensional model. As explained in the previous section, in the calibration, the parameter w_1 was imposed using the flow discharge Q_1 calculated from the 2-D simulations, whereas the parameters U_1, U_2, K_1 and K_2 were optimized to obtain a best-fit with the 2-D model results. A good agreement between the curves is found both in linear and in logarithmic

Table 3.2. Best-fit model parameters for $Q = 0.5\,\mathrm{m^3\ s^{-1}}$ and main channel width $b = 10\,\mathrm{m}$.

n^* (-)	1.00	0.875	0.756	0.643	0.535	0.432	0.333	0.239	0.149	0.0625
w_1 (%)	0.202	0.213	0.226	0.241	0.259	0.280	0.307	0.343	0.395	0.489
K_1 ($\times 10^{-2}\,\mathrm{m^2 s^{-1}}$)	4.38	6.44	7.63	8.04	8.70	9.77	11.7	15.1	21.0	35.8
K_2 ($\times 10^{-2}\,\mathrm{m^2 s^{-1}}$)	6.67	7.41	6.44	6.10	5.94	5.89	5.84	5.75	5.63	5.45
U_1 ($\times 10^{-2}\,\mathrm{m s^{-1}}$)	2.20	2.17	2.47	2.68	2.90	3.14	3.44	3.83	4.43	5.54
U_2 ($\times 10^{-2}\,\mathrm{m s^{-1}}$)	1.99	1.99	1.93	1.89	1.84	1.79	1.72	1.62	1.49	1.25
T_1 ($\times 10^3$ s)	9.08	9.21	8.08	7.45	6.90	6.37	5.82	5.22	4.52	3.61
T_2 ($\times 10^3$ s)	10.0	10.0	10.4	10.6	10.9	11.2	11.6	12.3	13.4	16.0
Pe_1 ($\times 10^4$)	4.19	4.34	4.56	4.79	5.08	5.43	5.90	6.57	7.68	10.3
Pe_2 ($\times 10^4$)	8.33	8.26	8.18	8.10	8.02	7.59	7.86	7.77	7.66	7.49

scale. The use of an advection-dispersion model for the two transport components leads to a satisfactory representation of the RTDs, both in presence and absence of a clear bimodality. The behavior of the tails is also well represented, with only a slight deviation in the most channelized case. The model is therefore capable to represent the residence time statistics with good approximation, matching the main time scales and the variance of the RTDs.

The conceptual model expressed by equation (3.29) and equation (3.30) linking the weight w_1 to the channel width, b^*, and the vegetation density ratio, n^*, shows a good agreement with the flow discharges calculated in the 2-D simulations. As shown in Figure 3.5, the model appears to slightly overestimate the discharge flowing in the MFC (and consequently underestimate the discharge in the LVZs), especially for smaller values of n^*. In this case, the vegetation density in the main channel is lower and the velocity higher, making the magnitude of the

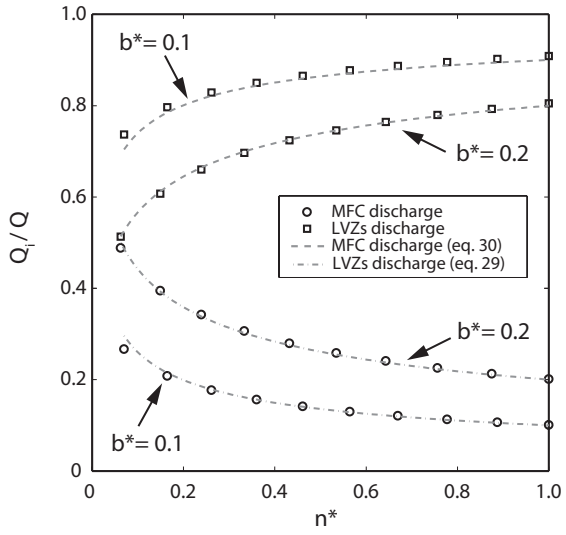

Figure 3.5. Comparison between discharges calculated with the 2-D depth-averaged model and equations (3.29)-(3.30). Results are plotted for $b^* = 0.1$ and $b^* = 0.2$.

first term of equation (3.24) comparable to the fourth term, which was neglected in the derivation of equation (3.29) and equation (3.30). This term should be taken into account if a higher accuracy is desired. However, the approximation provided by equation (3.29) and equation (3.30) appears to be quite satisfactory to determine the value of the weight factor w_1, as demonstrated by the graph in Figure 3.5.

The values of the Peclet number for the main channel, $Pe_1 = U_1 b/E_{T,1}$, and the lateral vegetated zones, $Pe_2 = U_2(B-b)/2E_{T,2}$, calculated using the transverse diffusion coefficient in equation (3.11), are reported in Table 3.1 and 3.2, respectively. The values indicate that the transport process is dominated by advection both in the MFC and in the LVZs. In particular, it is interesting to note that the nondimensional longitudinal dispersion coefficients, defined as $K_i^* = K_i/E_{T,i}$, are found to be proportional to the square of the Peclet number Pe_i^2. This means that the ratio K_i^*/Pe^2 is approximately constant as the density ratio n^* varies. Deviations from a constant value are observed for density ratios close to one (i.e. $n^* \approx 1$) for which the bimodality of the RTDs is much less pronounced, mak-

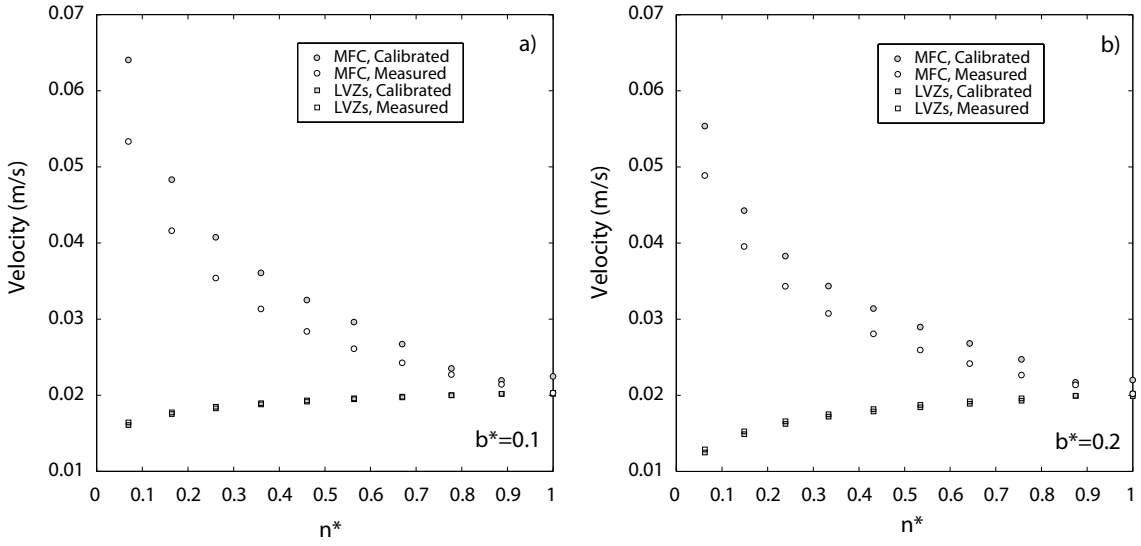

Figure 3.6. Comparison between computed velocities and calibrated velocities in the main channel and in the vegetated zones. Results are plotted for $b^* = 0.1$ (a) and $b^* = 0.2$ (b).

ing the automatic parameter estimation unable to distinguish between the two transport components. Overall, the parameterization of the RTDs expressed by equation (3.21) and equation (3.22) can well reproduce the shape of the simulated RTDs, and the approximate relationships in equation (3.29) and equation (3.30) provide a reliable estimate of the repartition of the flow discharge in the MFC and the LVZs. Although the parametric dependence of the dispersion coefficients K_1 and K_2 is not fully resolved, results show that the ratios K_i^*/Pe^2 are independent of n^* and depend only on the nondimentional channel width b^*.

3.5 Conclusions

A two-dimensional depth-averaged hydrodynamic model coupled with a solute transport model was used to derive the hydraulic residence time distribution in a conceptual wetland characterized by a main flow channel (MFC) and lateral vegetated zones (LVZs). Results show that the repartition of the flow between the main channel and the vegetated zones leads to a bimodal behavior of the

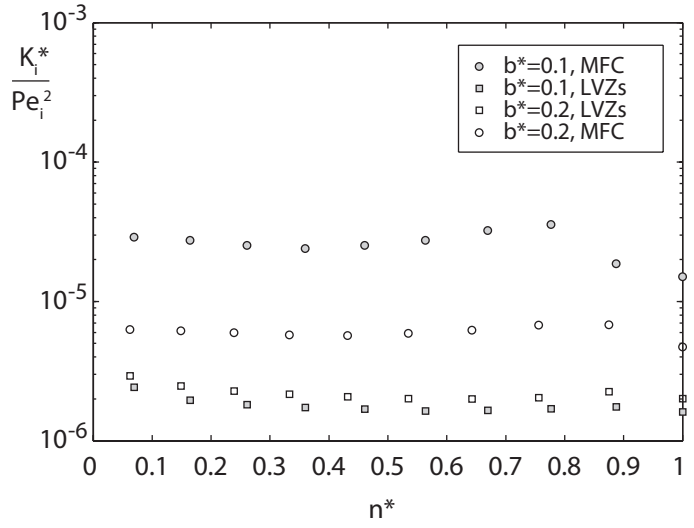

Figure 3.7. Behavior of the ratio K_i^*/Pe_i^2 in each zone. The nondimensional groups are calculated using the transverse diffusivity defined by equation (3.11).

hydraulic RTDs. The shape of the RTDs was modeled with an adapted version of the STIR model, here called STIR-DTD, that uses two components to represent surface transport. Although the model can be easily extended to account for additional retention processes, the use of a conventional advection-dispersion model for each transport component was shown to be sufficient to adequately reproduce the observed bimodality, with a reasonable level of accuracy also for the tail behavior of the RTDs. The best-fit model parameters were analyzed as a function of the width of the MFC and the density ratio between the MFC and the LVZs. The position of the two concentration peaks on the time axis is linked to the average travel time in each zone, whilst the ratio between the non-dimensional longitudinal dispersion coefficient and the square of the Peclet number was found to be approximately constant. Approximate analytical relationships were derived for the flow discharges in the MFC and in the LVZs, which allow to estimate part of the model parameters in a predictive way.

The analysis presented in this work retains a number of limitations due to the simplified geometry and topography of the simulated wetland. Even in the ide-

alized case of a rectangular wetland with uniform bed elevation, the residence time statistics depends on several variables, such as the flow discharge, the wetland aspect ratio, the geometry of the main channel and the vegetation density, making the problem extremely complex to describe in a comprehensive way. The methodology and the results presented in this work can, however, be a basis for future studies aiming to clarify the relationship between contaminant removal efficiency and design parameters of constructed wetlands for waste-water treatment.

Chapter 4

Optimal vegetation distribution in wetlands: an automatic evolutionary algorithm[1]

4.1 Introduction

Pollution control in natural water bodies is one of the most important tasks of our time. High concentrations of different dissolved organic chemicals, such as carbon, nitrogen or phosphorus, can stress ecosystems, decrease overall environmental quality and change the characteristics of the water for human uses. Over the past 50 years, a great effort has been made to collect, control and process polluted water with treatment plants specifically designed for wastewater. While such an approach is effective with point sources (sources characterized by high concentrations and relatively small volumes of fluid), its cost may be excessive in presence of diffused sources (sources characterized by low concentrations and big volumes of fluid). To treat wastewater in the latter cases, researchers proposed to exploit the bio-geochemical processes present in natural environments,

[1] The contents of this chapter have been partially published in: M. Gaudesi, A. Marion, T. Musner, G. Squillero, A. Tonda, An Evolutionary Approach to Wetlands Design, *SAC2013*, 28th Symposium On Applied Computing, Coimbra, Portugal, March 18 - 22, 2013

for example adopting free surface constructed wetlands. Wetlands are small artificial basins, partially covered by water, used to purify and filtrate polluted water by means of vegetation. Patches made of plant species that exploit dissolved organic matter present in water to support their vital functions (e.g., *Phragmites Australis*, *Typha Latifolia*), are distributed over the wetland area in order to obtain a valuable breakdown efficiency.

Designing an effective wetland, however, is a difficult task. While it is possible to determine the effect of a certain configuration of vegetation patches using simulation tools, the underlying dynamics are too complex to derive an inverse function. The only viable approach is therefore the classical trial and error, deeply relying on human sensibility and experience. Vegetated areas are tentatively placed by an expert, and the effect evaluated using simulation tools. Then, the expert needs to manually tweak the characteristics and position of each vegetation patch until a satisfactory result is attained.

Over the past decade, evolutionary algorithms (EA) have been successfully employed as optimization tools in many real-world applications (*Yu et al.*, 2008; *Sanchez et al.*, 2012). EAs provide an effective methodology for tackling difficult problems, when no preconceived idea about the optimal solution is available. While it is not usually possible to mathematically guarantee that the optimal solution will be found in a finite amount of time, EAs have been demonstrated able to perform much better than traditional optimization techniques in several practical non deterministic polynomial-time hard (NP-hard) problems.

This chapter proposes an automatic approach to wetland design. Candidate layouts are generated by an EA that internally uses a state-of-the-art fluid dynamics simulator to evaluate water purification and water flow alterations. The process is completely automatized, and it is not based on human experience or sensibility. Nevertheless, experimental results clearly show that the best solution

evolved is comparable to a solution devised by an expert starting from the same premises.

4.2 Background

4.2.1 Wetlands

Cowardin (1979) defines a wetland as an ecosystem transitional between aquatic and terrestrial ecosystems, in which the water table is usually at or near the surface or the land is covered by shallow water (*Bendoricchio and Jorgensen*, 2001). Before the extensive land reclamation through the last century, wetlands were common along the coasts, where they functioned as a natural buffer between inner agricultural zones and coastal areas. Today there is a pressing necessity to restore these areas and their role, defining optimal design criteria to obtain, at reasonable costs, the best removal efficiency.

The removal efficiency of natural and constructed free-surface wetlands is controlled by the time spent by contaminants into vegetated zones (*Persson et al.*, 1999). The role of vegetation in wetlands is important for two main reasons: water passing through vegetated zones decreases its local velocity, favoring the sedimentation of suspended solids; and biochemical processes determine a transformation of the dissolved substances. In combination with bathymetry, distribution of vegetation can produce preferential pathways of water (hydraulic shortcuts) that can substantially decrease the overall efficiency of a wetland. Removal efficiency is also affected by other hydrodynamic characteristics, as water depth and discharge, both dependent on vegetation distribution and density (*Akratos and Tsihrintzis*, 2007; *Kadlec and Wallace*, 2009). Wetlands constructed for waste water treatment are often designed considering an average water residence time (*Kadlec and Wallace*, 2009), even though these methods cannot adequately describe spatial configurations of vegetation in real wetlands (*Kadlec*, 2000). These models, usually called zero-dimensional, are often used because they require a

few data and are easy to manage. Nevertheless, zero-dimensional models produce significant inaccuracies in the prediction of the efficiency of contaminant removal. Other one-dimensional models with transient storage were recently used (*Martinez and Wise*, 2003) to assess the contaminant removal in a constructed wetland, giving in most cases a good approximation of breakthrough curves.

These models, however, fail to describe different flow paths across the vegetation and through main channels. The evidence of different flow pathways results, as described in previous chapter, in a clear bimodality of the solute breakthrough curves, that account for the different characteristic time scales of water residence time. Since spatial heterogeneity of the variables assumes a prominent role in determining the removal efficiency, the use of a more detailed *two-dimensional* approach becomes necessary to obtain reliable predictions.

4.2.2 Evolutionary Algorithms

Natural evolution is not a random process: although it is based on random variations, their preservation or dismissal is determined by objective evaluations. Darwinian *natural selection* is the process by which only those changes that are beneficial to the individuals will spread into subsequent generations, and sometimes it strikingly resembles an optimization process. Unlike most optimization processes, however, it does not require the ability to design intelligent modifications, but only the assessment of the effect of random modifications.

Several researchers, independently, tried to replicate such a characteristic to solve difficult problems more efficiently. Evolutionary computation does not have a single recognizable origin, but most scholars agree on identifying four macro areas: genetic algorithms (*Holland*, 1992), evolution strategies (*Schwefel*, 1965), evolutionary programming (*Fogel*, 1962), and genetic programming (*Koza*, 1992).

The different paradigms share some key concepts, and can be cumulatively called evolutionary algorithms. An EA starts by generating an initial set of usu-

ally random candidate solutions for the given problem. These solutions, called *individuals*, are evaluated using problem-dependent metrics. The result of the evaluation, that is, the goodness of the solution, is termed *fitness*. The set of candidate solutions, also known as *population*, is then sorted on its fitness values. Subsequently, offspring is produced by altering the existing solutions: often the best solutions have a higher probability of being selected for reproduction. Offspring might be added to the existing population, or replace it entirely; in any case, some of the worst solutions are deleted before iterating the process, starting from reproduction. When a given stop condition is met, the iterations end and the best solutions are returned to the user.

Being based on a population, EAs are more robust than pure hill climbing. Both small and large modifications are possible, but with different probabilities. Sexual recombination makes it possible to merge useful characteristics from different solutions, exploring efficiently the search space. Furthermore, EAs are quite simple to set up, and require no human intervention when running. They are inherently parallel, and a nearly-linear speed-up may be easily achieved on multiple instruction/multiple data (MIMD) architectures. Finally, it's easy to trade-off between computational resources and quality of the results.

4.3 Proposed Approach

The proposed approach exploits an evolutionary algorithm to create candidate solutions to the wetland design problem, represented as a set of patches of vegetation to be placed inside the area at specific locations. Candidate solutions are evaluated by simulating the water flow inside the wetland, keeping track of the quantity of fluid being purified as well as several related metrics.

4.3.1 Mathematical Models

A wetland is modeled here using a two-dimensional depth averaged model that solves hydrodynamics coupled with a two-dimensional solute transport equation

with a first order decay term. Under the assumption of hydrostatic pressure, stationary flow, and negligible wind and Coriolis forces, the depth-averaged velocity field and water depth can be described by the following equations (*Wu*, 2007):

$$\frac{\partial(hU)}{\partial x} + \frac{\partial(hV)}{\partial y} = 0 \tag{4.1}$$

$$\frac{\partial(hU^2)}{\partial x} + \frac{\partial(hUV)}{\partial y} = -gh\frac{\partial z_s}{\partial x} + \frac{1}{\rho}\frac{\partial(hT_{xx})}{\partial x} + \frac{1}{\rho}\frac{\partial(hT_{xy})}{\partial y} - \frac{\tau_{bx}}{\rho} \tag{4.2}$$

$$\frac{\partial(hUV)}{\partial x} + \frac{\partial(hV^2)}{\partial y} = -gh\frac{\partial z_s}{\partial y} + \frac{1}{\rho}\frac{\partial(hT_{yx})}{\partial x} + \frac{1}{\rho}\frac{\partial(hT_{yy})}{\partial y} - \frac{\tau_{by}}{\rho} \tag{4.3}$$

The quantities U and V represent the depth-averaged velocities [$\mathrm{L\,T^{-1}}$] along the x and y direction, respectively, h is the water depth [L], z_s is the water surface elevation [L], and ρ the water density [$\mathrm{M\,L^{-3}}$]. The bed shear stresses τ_{bx} and τ_{by} [$\mathrm{M\,L^{-1}\,T^{-2}}$] in the x and y direction respectively are calculated using the following relationships:

$$\tau_{bx} = \rho c_f m_b U\sqrt{U^2 + V^2} \tag{4.4}$$

$$\tau_{by} = \rho c_f m_b V\sqrt{U^2 + V^2} \tag{4.5}$$

In the case modeled here, the bed slope is set to zero and the investigated velocity range makes it possible to consider the friction coefficient as a constant. This assumption generally holds where the velocity is sufficiently fast to assume turbulent flow. For a flat bathymetry, the bed slope coefficient m_b is unitary and the coefficient of friction c_f can be rewritten using Manning's equation as $c_f = gf^2h^{-1/3}$. The effect of different vegetation densities is modeled here using different values of Manning roughness coefficient f [$\mathrm{T\,L^{-1/3}}$]. This choice is confirmed by many studies that relate vegetation density, stem diameter and flow conditions to an equivalent roughness coefficient (*Augustijn et al.*, 2006; *Green and Garton*, 1983; *White and Nepf*, 2003). Fluid shear stresses $T_{ij}(i,j = x,y)$ associated to viscous and

turbulent effects, are determined using the Boussinesq assumption:

$$T_{xx} = 2\rho(\nu + \nu_t)\frac{\partial U}{\partial x} \tag{4.6}$$

$$T_{xy} = T_{yx} = \rho(\nu + \nu_t)(\frac{\partial U}{\partial y} + \frac{\partial V}{\partial x}) \tag{4.7}$$

$$T_{yy} = 2\rho(\nu + \nu_t)\frac{\partial V}{\partial x} \tag{4.8}$$

where ν, ν_t, are the kinematic and eddy viscosities $[\mathrm{L}^2\,\mathrm{T}^{-1}]$. Since the kinematic viscosity has a lower value than the eddy viscosity, it can be neglected in most cases. For a turbulent flow regime, as it was assumed in this preliminary study, ν_t can be expressed using Elder depth-averaged parabolic model (*Elder*, 1959) as $\nu_t = \alpha u_* h$, where the term α is an empirical coefficient dims- and u_* is the shear velocity $[\mathrm{L}\,\mathrm{T}^{-1}]$.

For longitudinal dispersion Elder proposed a value of the coefficient α of about 5.9 (*Elder*, 1959), for transverse dispersion, Fischer found that α is about 0.6 (0.3-1.0) in irregular waterways with weak meanders (*Fischer et al.*, 1979). In accordance with *Arega and Sanders* (2004) and *Wu* (2007), a value of α of 6.0 and 0.6 was chosen for the longitudinal and transversal dispersion coefficients respectively.

Solute transport of a reactive tracer through the wetland is simulated with a depth-averaged solute transport model accounting for the effect of advection, turbulent diffusion, dispersion and decay. In the simulations, the tracer is assumed to interact with vegetation and the chemical breakdown due to the permanence in the vegetated zones is modeled with a first order decay relationship. The equation governing the transport of a reactive tracer in the wetland can be modeled as:

$$\frac{\partial(hUC)}{\partial x} + \frac{\partial(hVC)}{\partial y} = \frac{\partial}{\partial x}(hE_{xx}\frac{\partial C}{\partial x}) + \frac{\partial}{\partial y}(hE_{yy}\frac{\partial C}{\partial y}) - hkC \tag{4.9}$$

where C is the depth-averaged solute concentration [ML^3], U, V are the vertically integrated velocity components under steady flow conditions [$\mathrm{ML}^{-1}\,\mathrm{L}^{-2}$] in the x, y directions respectively. Coefficient E_{xx}, E_{yy} [$\mathrm{L}^2\,\mathrm{T}^{-1}$], account for both turbulent diffusion and dispersion. For simplicity, constant homogeneous value of E_{xx}, E_{yy} is chosen ($10^{-5}\,\mathrm{m}^2\,\mathrm{s}^{-1}$) throughout the entire domain.

4.3.2 Evolutionary Core

The EA used is μGP (*Sanchez et al.*, 2011), is a versatile toolkit developed at Politecnico di Torino in the early 2000s and available under the GNU Public License from Sourceforge[2]. μGP original use was to assist microprocessors' designers in the generation of programs for test and verification, hence, the greek letter μ in its name. But over the years has been used as optimizer in a much wider spectrum of problems, including numerical optimizations.

The algorithm initially creates a set of random candidate solutions to the given problem, that are then evaluated, and sorted by their fitness value (see Subsection § 4.3.3). Offspring is then created favoring the fittest individuals and also trying to favor diversity among the population. New candidate solutions are then evaluated and added to the initial population. Solutions are again sorted, and the worst ones are removed until the population returns to its original size. The process is then iterated, starting from offspring generation, until a stop condition is reached.

Two categories of genetic operators are used to generate the offspring: *mutations*, or single-parent operators, and *crossovers*, or recombination operators. Mutation operators create new candidate solutions by altering one single parent solution; crossover operators mix the information contained in two or more parents solutions to create offspring. The most common operators are available

[2] http://ugp3.sourceforge.net/

inside μGP, but the toolkit also implements *differential evolution* and other operators specially calibrated for real parameters.

μGP, relying on an external configuration file, constraints the individuals, represented internally as multigraphs, to sensible structure, and maps the internal individuals to valid solutions of the problem. In the specific context, each individual encodes a candidate wetland configuration, that is, it describes the features of the several vegetation patches, with variable number of occurrences from 20 to 35, that are going to be placed over the wetland area; the order in which the patches are described within the individual is irrelevant. All vegetation patches are assumed to be of circular shape. Since they can overlap, however, they can create more complex shapes. Each patch is characterized by its position (x, y coordinates expressed in real values) over the wetland, its radius, and the friction value of the center. Position of vegetation patch is constrained by the size of the wetland; its radius is constrained following the minimum and maximum size of typical vegetation areas that characterize real wetlands. Friction value is selected among several values associated to different kinds of vegetation.

Intuitively, vegetation patches tend to be denser in the middle and sparser near their outer bounds. Thus, vegetation density in an individual present two discontinuities, at $radius/2$ and $3*radius/4$ respectively, where the friction value in the center is higher. Friction value is increased in the common parts in case two vegetated patches overlap. A sample individual is presented in Figure 4.1.

4.3.3 Fitness Function

The definition of an appropriate fitness function is a key aspect in the use of an EA. The process of evolution is based on *differential survival*, that is, different individuals must have a different chance to spread their offspring in future generations. In the artificial environment modeled by an EA, it is essential that different individual get different fitness values. It is a common practice to include

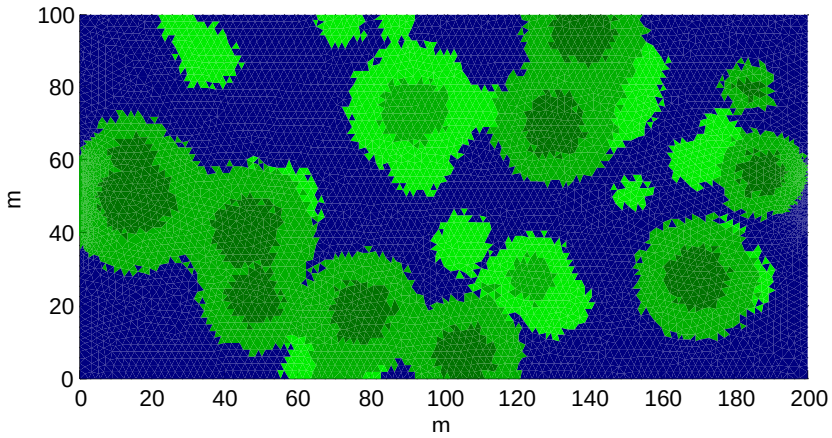

Figure 4.1. Phenotype of an individual: graphic representation of the genotype, represented by a list (center, radius etc.) of features that characterizes each vegetation patch. Darker green indicates a higher coefficient of friction.

in the fitness some heuristic knowledge, in order to help the EA explore the most promising regions of the search space.

In μGP, the fitness is not a single value but a vector of positive coefficients. The individual A is considered to be fitter than the individual B if the first j elements of the two fitness vectors are equal, and the $(j+1)-th$ element of the A's fitness is greater than the $(j+1)-th$ element of the B's fitness. In the context of wetland optimization, three values have been used.

In order to evaluate the goodness of a candidate wetland layout, a simulation of the hydrodynamic field is performed extracting computed values of discharge Q $[\mathrm{L}^3\mathrm{T}^{-1}]$ and water depth h $[\mathrm{L}]$ at the inlet and at the outlet sections of the wetland. During the simulation, a reactive tracer with a known concentration is injected at the inlet. Thanks to the presence of vegetation the tracer is gradually degraded and reaches the outlet section. Mass fluxes $\dot{M}_{in}$ and $\dot{M}_{out}$ $[\mathrm{MT}^{-1}]$ passing through these sections are measured, and the difference between the two values represent the first parameter of the fitness function. In order to obtain the optimal vegetation distribution, this difference must be maximized.

On the other hand, a candidate layout must still let the water flow, avoiding configurations where the vegetation is so dense to make the flow impossible. The energy requested by the water to flow can be represented by the difference between the water depth at the inlet and outlet section. This difference represents the second parameter of the fitness function. This parameter is minimized by the algorithm: solutions that completely block the water flow are then heavily penalized.

The third and last fitness parameter measures the difference of discharge between the inlet and the outlet sections of the wetland. This value assures that the stationary flow conditions are reached and that the mass fluxes are finely computed. This discharge difference is strongly minimized.

4.4 Experimental Evaluation

The flow domain is given here by a 200m-long-by-100m-wide rectangular wetland. The length of the wetland allows the solute to spread throughout the cross section and make sure that the whole vegetated area can act on the breakdown process. The elevation of the bed is assumed to be constant, as in a large set of natural wetlands the bed topography does not vary significantly in space and the effect of bed slope can be discarded (*Wörman and Kronnäs*, 2005; *Wu*, 2007).

Inlet and outlet sections (each 10 m wide) are located symmetrically in the middle of the shorter sides of the wetland domain. A constant discharge of $0.2\,\mathrm{m}^3\,\mathrm{s}^{-1}$ is imposed at the inlet section and a constant water depth of 0.5 m acts as the downstream boundary condition at the outlet section. The remaining boundary is treated as impermeable (no flux condition) and no friction is applied to the lateral walls. Reactive solute with a constant concentration of $1\,\mathrm{kg}\,\mathrm{m}^{-3}$ is injected at the inlet section and, once the steady state is reached, the average value of concentration at the outlet section is calculated in order to define the

value of the fitness function. An adaptive triangular mesh is used to ensure numerical stability and resolution in case of steep gradients of the hydrodynamic and solute transport solutions.

A value of the Manning roughness coefficient and a particular decay value are assigned to each node of the grid, according to the particular generated individual. The value of decay coefficient k [T^{-1}] is assigned only to those zones in which vegetation is present, assuming higher values in zones with higher roughness coefficient. Decay coefficients are conveniently scaled compared to natural ones in order to obtain a measurable breakdown (not affected by numerical errors) at the outlet sections. Manning roughness coefficients vary from $0.02\,s\,m^{-1/3}$ to $0.20\,s\,m^{-1/3}$ and decay coefficients vary from $10^{-6}\,s^{-1}$ to $10^{-5}\,s^{-1}$. A zero value of the decay coefficient is assigned to the zones without vegetation.

The evolutionary core exploited is μGP version 3.2.0 (revision 198). Fitness of each individual is evaluated solving equations (4.1)-(4.3) and equation (4.9) by a free, open source code called *TELEMAC2D*, part of the wider set of programs *openTELEMAC* (*Galland et al.*, 1991; *Hervouet et al.*, 1994). The code has been specifically modified in order to meet the requirements of the performed simulations.

Each individual evolved by μGP is converted to the *TELEMAC2D* format: a map of the nodes in the basin is created and to each node covered by a vegetation patch is assigned the correct law of friction and the relative decay coefficient. In order to reduce the computation time required to simulate an entire population, individual processing is distributed on two machines: through this approach and by means of EAs' parallelism characteristics, it is possible to process different individuals at the same time. For this purpose, *GNU Parallel* (*Tange*, 2011), a shell tool for executing jobs in parallel using one or more computers, is used to distribute the computing effort.

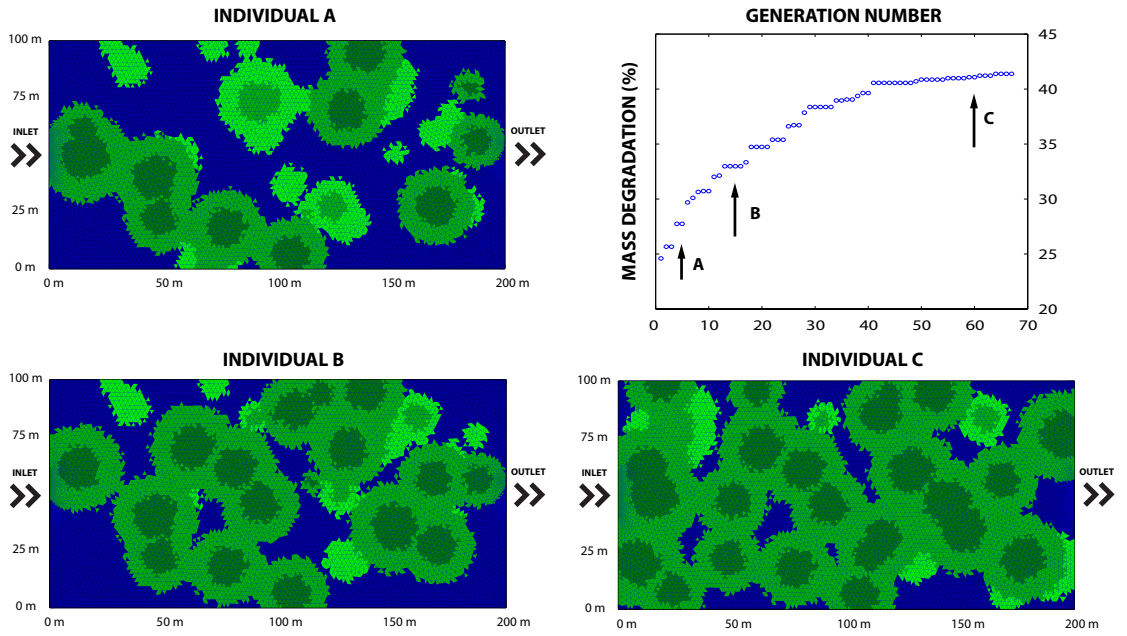

Figure 4.2. Progressive optimization of candidate solutions. On the left, the best layout in the population, for several generations. On the right, a graph showing the increase in the best fitness value as the EA proceeds.

The optimization process is run on two distributed machines, configuring the system in order to simulate up to 4 individuals at the same time on each machine. The first machine is equipped with an *Intel Core i5-2500* CPU running at 3.3 GHz, while the second is equipped with an *Intel Core i7-950* CPU running at 3.06 GHz. By means of this configuration, it was possible to evaluate a maximum of eight individuals at the same time, requiring an average computation time of 80 minutes for each individual.

To check the functioning of the optimization system, two different numerical experiments have been performed: the first one, with a wider range of free optimization parameters, has been performed to check the ability of the system to give reasonable results in term of vegetation distribution and density; the second one, with a limited number of free parameters has been performed to observe the geometric characteristics of an optimal vegetation distribution in terms of mass

degradation.

The first experiment fixes a maximum number of vegetation patches but does not limit a total amount of vegetated surface. The optimization algorithm can modify the position of the vegetation patches, the radius and the value of the Manning's roughness coefficient. Each vegetation patch can be freely positioned over the wetland surface by the genetic algorithm starting from an initial random population of 20 individual ($\mu_i = 20$). The EA uses a set of 12 genetic operators applied at each step of evolution ($\lambda = 12$)[3]. μGP constantly adjusts the activation probabilities of each genetic operator in order to enhance the evolution process.

In the second experiment, the vegetational cover has been fixed to a maximum value of 60% of the total wetland surface. A single uniform roughness coefficient corresponding to an uniform vegetation density has been imposed for each vegetation patch. A unique law of friction (and therefore a single decay coefficient equal to $5\times10^{-6}\mathrm{s}^{-1}$) was applied to the mesh nodes covered by vegetation and no decay properties were assigned to the zone not covered by vegetation. Manning roughness coefficients were set to 0.20 $\mathrm{s\,m}^{-1/3}$ to nodes with vegetation, and 0.02 $\mathrm{s\,m}^{-1/3}$ otherwise. The EA has been configured to create a random initial population of 20 individuals ($\mu_i = 20$), on which 12 genetic operators ($\lambda = 12$) chosen among the 20 available in *μGP* tool have been applied at each evolution stage. The entire process evolved for 90 generations, for a total of 1070 individuals generated. During the individual generation, all those individuals characterized by a vegetation cover larger than 60%, were discarded in order to hold the initial constraint of a fixed vegetation.

[3]Differently from the usual terminology, in μGP "λ" represents the number of genetic operators activated in each generation. Since each genetic operator may generate any number of individuals (even zero), the true offspring size cannot be defined.

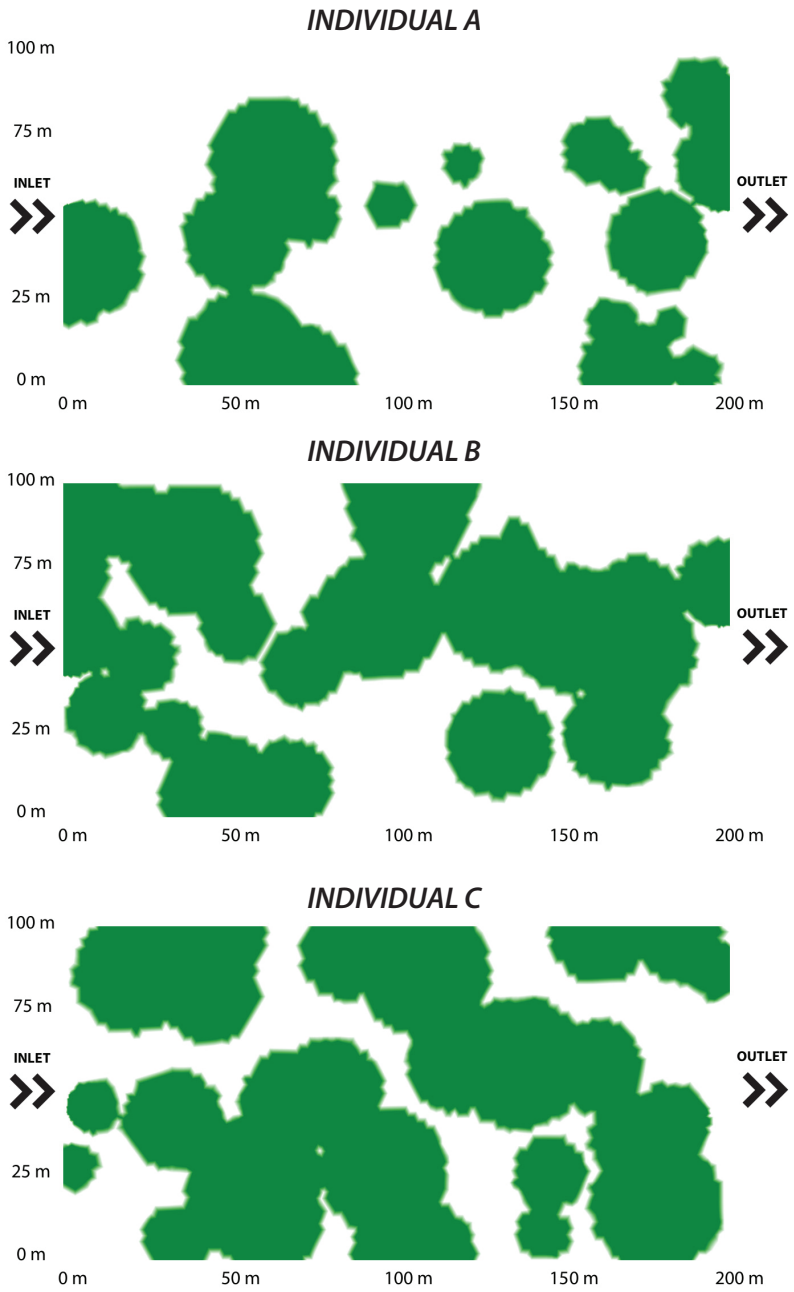

Figure 4.3. Three stage of the optimization performed keeping a fixed maximum value of vegetation cover equal to 60%. One of the initial individuals (individual A) is characterized by a poor vegetational cover, whilst individuals B and C reach the maximum vegetation even with a different disposition of vegetated patches. Individual C is characterized by the maximum mass removal efficiency.

4.5 Results and Discussion

Results of the first test were reached after approximately 100 generations and 1100 individuals analyzed and are described in Figure 4.2. Three individuals at three different evolution stages are shown as a reference for the whole optimization process. It is interesting to note that each individual presents the same number of vegetated patches. Individual *A*, at the initial stage of the evolution, shows a poor vegetative covering and vegetation patches are characterized by both dense and sparse vegetation (brighter color for some patches compared to the others). Level of mass degradation is around 20%. During the computation, the evolution promotes individuals to spread over the wetland surface and to develop a thicker vegetation. This is clear in the case of the individual *B*, in which the percentage of superimposed vegetation patches decreases. Patches tend to cover the maximum available wetland surface by reaching the maximum allowed *radius* of 20 m: patches diameter becomes indeed more homogeneous compared to individual *A* and the remaining small vegetated areas does not impact on the degradation process. In this case, mass degradation increases and reaches a value close to 32%. As the evolution proceeds, the vegetative cover tends still to increase (individual *C*) even though mass degradation values show an asymptotic behavior from generations 45 to 70. That means that, at this stage of evolution, processed individuals are very similar to each other and the population can be regarded as mature. Under the assumption of the model, mass degradation percentage of the best individual reaches a satisfying 43%, approaching values that are common in real constructed wetlands (*Haberl et al.*, 1995).

Results of the second experiment are described in Figure 4.3. Among individuals of first generations, its possible to note some individuals (individual A, for example) which are characterized by a low number of vegetated areas clearly separated between each other. This configuration produces a low filtration ca-

pacity due to the limited decay process acting along the wetland. Individual A is characterized by a removal efficiency of 21% related to the inlet concentration. As evolution proceeds, vegetational cover tend to increase and the evolutionary algorithm generates individuals which respect the maximum cover constraint. The maximum number of patches is rapidly reached and the maximum radius of each patch grows fast in order to reach the 60% value. In order to define more complex configurations, the EA is able to combine position and dimensions of each area, creating complex shapes and allowing a better filtering performance. A direct comparison between individual B and individual C in Figure 4.3 allow to identify shapes and characteristics of vegetation patches that optimizes the breakdown efficiency: both individual B and C are indeed characterized by a vegetated coverage very close to the imposed limit of 60%, but have a different fitness value. Individual B belongs to the third generation, in which evolution is still very close to the starting stage and, although the maximum vegetation coverage is reached, is characterized by a filtering amount to 27%. Individual C instead, represents the best configuration achieved in this experiment: vegetative cover is comparable to individual B but presents a filtering performance of 33.2%. The difference between these two configurations can be addressed to the length of the flow pathways between the inlet and the outlet zones: vegetation disposition in individual C forces the water to pass through vegetation following a longer pathway, whereas vegetation disposition in individual B allow the solute to reach the outlet section in a faster way passing through the lower end of the wetland domain.

4.6 Conclusions

Wetlands are artificial ponds, extensively used to filtrate and purify water. Achieving an optimal design for this purpose is an extremely complex task, usually carried on by experts on the basis of fluid dynamics simulations. In this chap-

ter, an evolutionary algorithm is applied to the wetlands design problem. Each candidate solution is evaluated by a state-of-the-art fluid dynamics simulator, on the basis of several relevant metrics. Experimental results on the best solution provided by the algorithm show a performance comparable with human-devised designs, despite the absence of human intervention during the optimization process. Future works will include a more complex individual representation, with patches of several different shapes and a more refined management of friction values. Managing larger populations, or different sub-population, might also prove beneficial to the quality of the final solutions: nevertheless, the computational-intensive simulations needed to evaluate a single candidate represent a severe bottleneck. For this reason, further developments will probably exploit the parallelism innate in evolutionary algorithms, using clusters or grids to speed up the process. Finally, the choice of decay coefficients has a predominant role in determination of the final breakdown efficiency: a more detailed analysis on a real case should be used to demonstrate the potential of the proposed approach, that shows promising results in this first experience.

Chapter 5

Random field modeling of wetlands[1]

5.1 Introduction

In the previous chapter, an automatic genetic optimization procedure has been performed to define the best vegetation distribution that produces the maximum mass breakdown efficiency. Nevertheless, a more comprehensive work is needed to identify spatial vegetation characteristics (size of vegetation patches, complex shapes, position related to the inlet and outlet zones..) that produce the optimal breakdown efficiency. A series of numerical experiments that mimic the effect of vegetation density on wetland efficiency have been therefore performed using, as a reference, a known spatial probability density function. This work will allow to define, if any exists, the best set of statistical parameters of a randomly distributed vegetation in order to achieve the maximum removal efficiency. Completely emergent vegetation is simulated by means of a two-dimensional depth averaged model that solves coupled hydrodynamic- and advection-diffusion equations with the presence of a first order decay term. Decay coefficient is assumed proportional to vegetation density in order to account for the effect of vegetation

[1] This chapter provides a brief preview of the first results coming from the last work on the effect of random spatial vegetation distributions on wetland efficiency.

on the chemical breakdown. Preliminary results suggest the definition of non-dimensional parameters which are able to relate statistical parameters of spatial random distribution to discharge and removal efficiency. At this stage, only a few combination of parameter have been investigated, but first considerations can be made in order to address next simulations.

5.2 Modeling overview

Simulation have been performed using the modeling framework defined in Chapter 3 adapting the solute transport equation in order to account for mass breakdown. For the sake of completeness, main equations are rewritten here in their more simplest form, leaving the detailed description to the dedicated chapter.

5.2.1 Hydrodynamic model

Under the assumption of hydrostatic pressure, incompressible fluid, steady-state flow, negligible wind and Coriolis forces, the depth-averaged velocity field and water depth satisfy the following equations (*Wu*, 2007):

$$\frac{\partial(hU)}{\partial x} + \frac{\partial(hV)}{\partial y} = 0 \tag{5.1}$$

$$hU\frac{\partial U}{\partial x} + hV\frac{\partial U}{\partial y} = -g\frac{\partial}{\partial x}\left(\frac{h^2}{2}\right) - \frac{\tau_x^b}{\rho} - \frac{\tau_x^v}{\rho} + ghi_x \tag{5.2}$$

$$hU\frac{\partial V}{\partial x} + hV\frac{\partial V}{\partial y} = -g\frac{\partial}{\partial y}\left(\frac{h^2}{2}\right) - \frac{\tau_y^b}{\rho} - \frac{\tau_y^v}{\rho} + ghi_y \tag{5.3}$$

The quantities U and V represent the depth-averaged velocities [$\mathrm{L\,T^{-1}}$] in the x- and y- directions, respectively, h is the water depth, i_x and i_y are the bottom slopes [$-$] along the x- and y- direction respectively, and ρ the water density [$\mathrm{M\,L^{-3}}$]. The shear stresses τ_x^b and τ_y^b account for bed resistance, whereas τ_x^v and τ_y^v account for vegetation resistance along the x- and y- direction, respectively. Reynolds stresses are assumed to be negligible compared to bed and vegetative resistance and the

contribution of bed friction to bed shear stresses is computed by adapting the one-dimensional relationships proposed by *Kadlec* (1990) to a two-dimensional velocity field.

The hydrodynamic field has been solved using a formal analogy between equations (5.1), (5.2) and (5.3) and the weakly compressible Navier-Stokes equations:

$$\frac{\partial(\rho U)}{\partial x} + \frac{\partial(\rho V)}{\partial y} = 0 \tag{5.4}$$

$$\rho U \frac{\partial U}{\partial x} + \rho V \frac{\partial U}{\partial y} = -\frac{\partial p}{\partial x} + \frac{\partial}{\partial x}\left[2\eta \frac{\partial U}{\partial x} - \left(\frac{2}{3}\eta - k_{dv}\right)\frac{\partial U}{\partial x} - \left(\frac{2}{3}\eta - k_{dv}\right)\frac{\partial V}{\partial y}\right] + \frac{\partial}{\partial y}\left[\eta\left(\frac{\partial U}{\partial y} + \frac{\partial V}{\partial x}\right)\right] + F_x \tag{5.5}$$

$$\rho U \frac{\partial V}{\partial x} + \rho V \frac{\partial V}{\partial y} = -\frac{\partial p}{\partial y} + \frac{\partial}{\partial y}\left[2\eta \frac{\partial V}{\partial y} - \left(\frac{2}{3}\eta - k_{dv}\right)\frac{\partial V}{\partial y} - \left(\frac{2}{3}\eta - k_{dv}\right)\frac{\partial U}{\partial x}\right] + \frac{\partial}{\partial x}\left[\eta\left(\frac{\partial U}{\partial y} + \frac{\partial V}{\partial x}\right)\right] + F_y \tag{5.6}$$

where ρ is the fluid density [$\mathrm{ML^{-3}}$], η is the dynamic viscosity [$\mathrm{ML^{-1}\,T^{-1}}$] and k_{dv} is the dilatational viscosity [$\mathrm{ML^{-1}\,T^{-1}}$]. A direct comparison of equations (5.1) and (5.4) shows the correspondence between the water depth h and the weakly compressible fluid density ρ, whereas a complete superposition of the remaining terms of of equations (5.2) and (5.5) can be obtained imposing $p = 1/2gh^2$ and $k_{dv} = 2/3\eta = 0$. Under these conditions, both the equations have the same velocity field and the numerical procedure used to solve the weakly compressible Navier-Stokes equations can be used to solve the hydrodynamic field described by equations (5.1), (5.2) and (5.3). This formal analogy has been used in order to exploit the complete and powerful set of routines provided by the *COMSOL Multiphysics®* software.

5.2.2 Solute transport model

Solute transport of a reactive tracer through a wetland is simulated with a depth-averaged solute transport model,

$$\frac{\partial(hC)}{\partial t} + \frac{\partial(hUC)}{\partial x} + \frac{\partial(hVC)}{\partial y} = \frac{\partial}{\partial x}(hE_{xx}\frac{\partial C}{\partial x} + hE_{xy}\frac{\partial C}{\partial y}) + \frac{\partial}{\partial y}(hE_{yx}\frac{\partial C}{\partial x} + hE_{yy}\frac{\partial C}{\partial y}) - hkC \tag{5.7}$$

where C is the depth-averaged solute concentration [ML^{-3}], U, V are the vertically integrated velocity components [LT^{-1}] in the x-, y-directions respectively and k is the decay coefficient [T^{-1}]. The coefficients $E_{i,j}$ [$\mathrm{L}^2\mathrm{T}^{-1}$], $i, j = x, y$, account for both turbulent diffusion and shear dispersion due to vertical velocity gradients. Values of coefficients $E_{i,j}$ have been calculated as described in Chapter 3 expressing the dispersion tensor as in *Arega and Sanders* (2004):

$$E_{xx} = E_L + (E_L - E_T)\frac{U^2}{U^2 + V^2} \tag{5.8}$$

$$E_{xy} = E_{yx} = (E_L - E_T)\frac{UV}{U^2 + V^2} \tag{5.9}$$

$$E_{yy} = E_T + (E_L - E_T)\frac{V^2}{U^2 + V^2} \tag{5.10}$$

where E_L and E_T represent the dispersion coefficients along the longitudinal and transversal flow direction, respectively.

5.3 Model application

The flow domain considered in this work is given by a rectangular wetland with length L = 400 m, width B = 300 m, and constant bed elevation. The choice of a zero bed slope is supported by the evidence that in many natural wetlands the bed elevation does not vary significantly in the streamwise direction, and the effect of bed slope can often be neglected (*Wörman and Kronnäs*, 2005; *Wu*,

2007). The flow domain is characterized by an inlet and outlet section $b = 10$ m and vegetation density n, expressed as $stems/m^2$ is randomly distributed over the wetland area.

The random field that describes vegetation density distribution over the wetland domain has been built using the free, open-source algorithm proposed by *Bellin and Rubin* (1996). Although the algorithm allow to reproduce random fields characterized by different spatial probability density functions, a simple Gaussian space probability density function with homogeneous correlation length has been adopted for this work. Varying the three parameters of the Gaussian PDF, (mean μ, variance σ and correlation length l_c), a number of 135 random fields was created. Three means of 400, 800 and 1200 $stems/m^2$ characterized by nine correlation lengths (5-10-15-20-25-30-35-40-45 m respectively) and three variances have been simulated. The variance of each field has been fixed in order to obtain only positive values of vegetation density.

For the flow equations (equation (5.1)–equation (5.3)), the boundary conditions are given by the inflow at the inlet and the water depth at the outlet, $h = 0.5$ m whereas the remaining boundary is treated as impermeable. Hydrodynamic field is computed varying the flux boundary condition at the inlet section until the same head loss of 0.03 m between the inlet and the outlet section has been reached for all tests. The choice to fix the head loss between inlet and outlet section appear reasonable as in large lowland basins, hydraulic safety and removal efficiency has a primary importance in relation to the amount of treated water.

For the solute transport equation, the boundary conditions are given by a constant unitary concentration at the inlet, $C = 1$, an open boundary condition at the outlet, and the no-flux condition on the remaining part of the flow boundary. The equations are solved via a finite element method using COMSOL *Multiphysics*® with quadratic shape functions. The effect of vegetation on breakdown efficiency

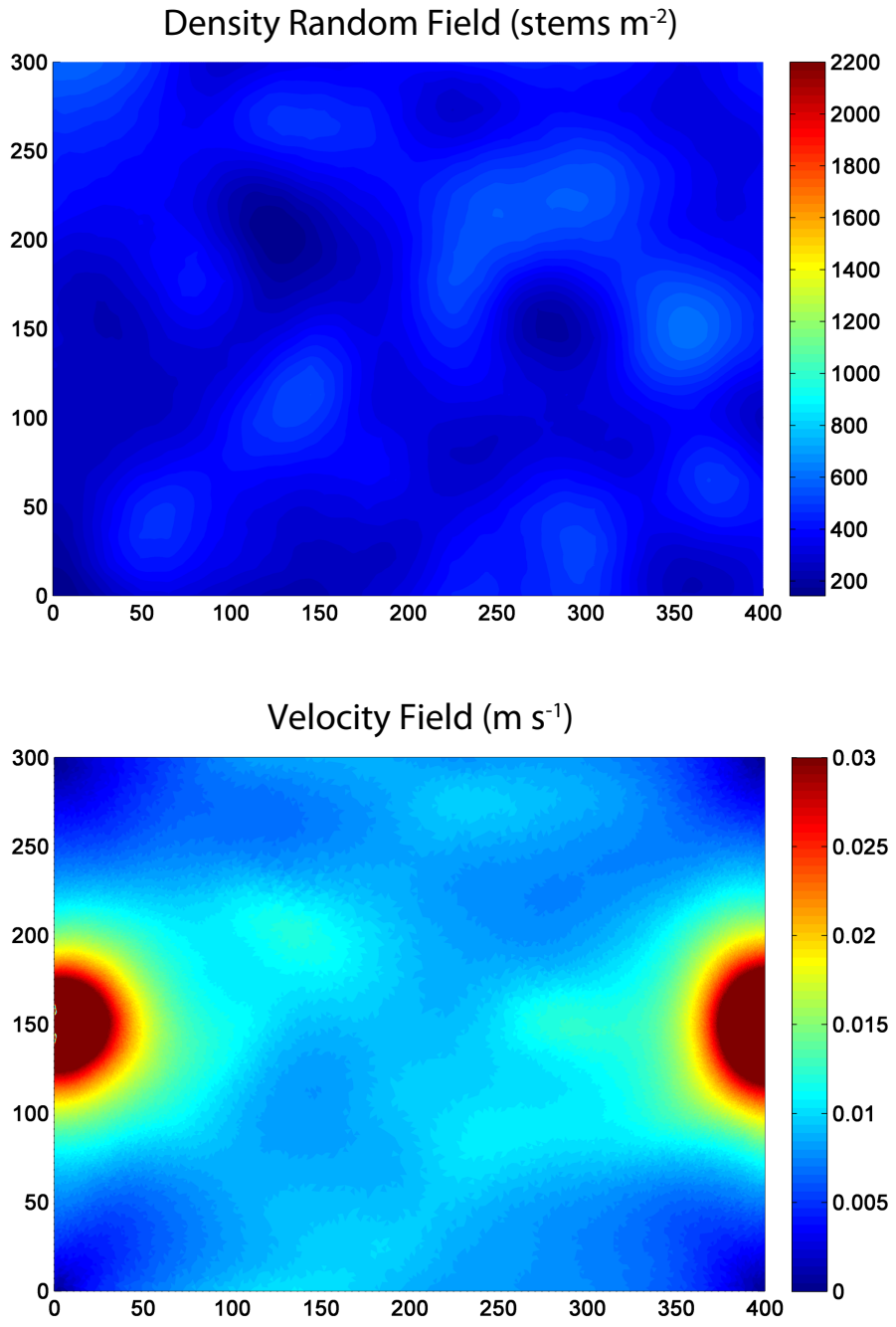

Figure 5.1. Random vegetation density field for a mean $\mu = 400$, a variance $\sigma = 10000$ and a correlation length $l_c = 45\,m$. Velocity field follows the main characteristics of the vegetation density: velocity module appear to be higher in zones characterized by low vegetation density.

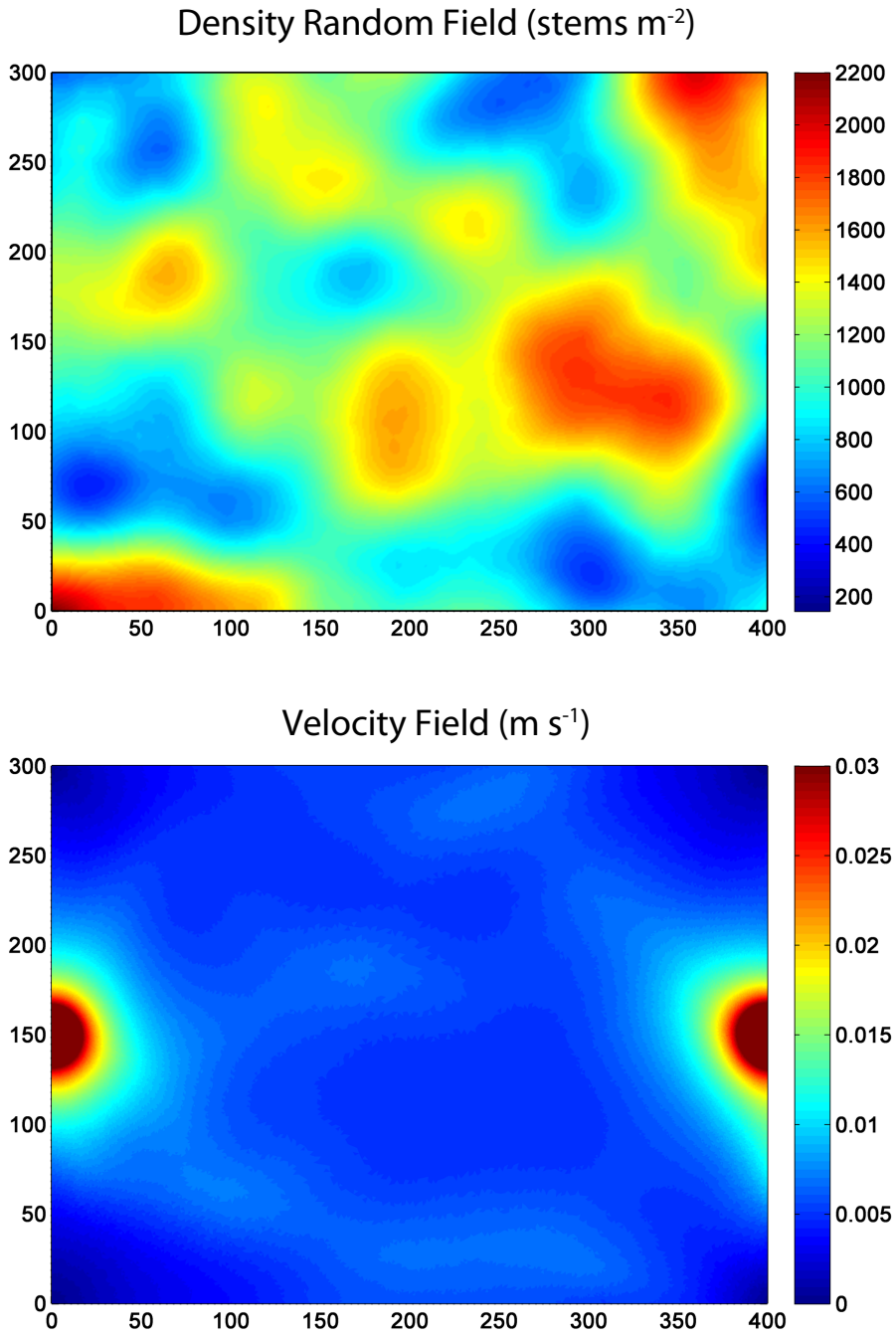

Figure 5.2. Random vegetation density field for a mean $\mu = 1200$, a variance $\sigma = 90000$ and a correlation length $l_c = 45\,m$. Velocity field follows the main characteristics of the vegetation density: velocity module appear to be higher in zones characterized by low vegetation density.

has been evaluated assuming a decay coefficient linearly proportional to stem density in order to account for different mean stem densities and for local patches of thicker vegetation. Examples of two different vegetation density fields and of the related velocity fields are shown in Figure 5.1 and in Figure 5.2. Values of discharges and removal efficiency have been measured for each case and plotted as a function of statistical parameters of the random density fields.

5.4 First results and considerations

First results are shown in Figure 5.3: as the mean stem density increases, the overall vegetation resistance increases and, keeping a constant head loss, the entering discharge decreases (Figure 5.3 c). Mass removal efficiency $E_M = M_{in} - M_{out}$ $[\mathrm{MT}^{-1}]$ (Figure 5.3 a) is related to removal efficiency $E = (C_{in} - C_{out})/C_{in}$ $[-]$ through the discharge: although other mean densities should be analyzed in order to have a clearer trend, it can be seen that mass efficiency tends to decrease the rate of growth as the mean density increases. A presence of a peak on the mass removal efficiency can be therefore expected as the mean vegetation density increases. Removal efficiency, expressed only as a function of the concentration difference between the outlet and the inlet sections, seem to be linearly correlated with mean vegetation density although an asymptotic behavior to 100% can be expected for larger mean densities. Figure 5.3 d shows the correlation between statistical parameters of the random density field, the discharge Q and the parameter $M_{yv} + M_{xv}$. M_{iv} represents a sort of first moment of the density around the x- y- axis defined by the inlet/outlet sections. The subscript v accounts for a weighting procedure based on the local velocity field, that assigns low importance to high density regions (assumed to have an higher breakdown effect) located in dead zones characterized by low velocity and therefore, low fluxes. Plotted variables in Figure 5.3 d are combined in order to obtain two non-dimensional quantities. The good correlation between these two non-

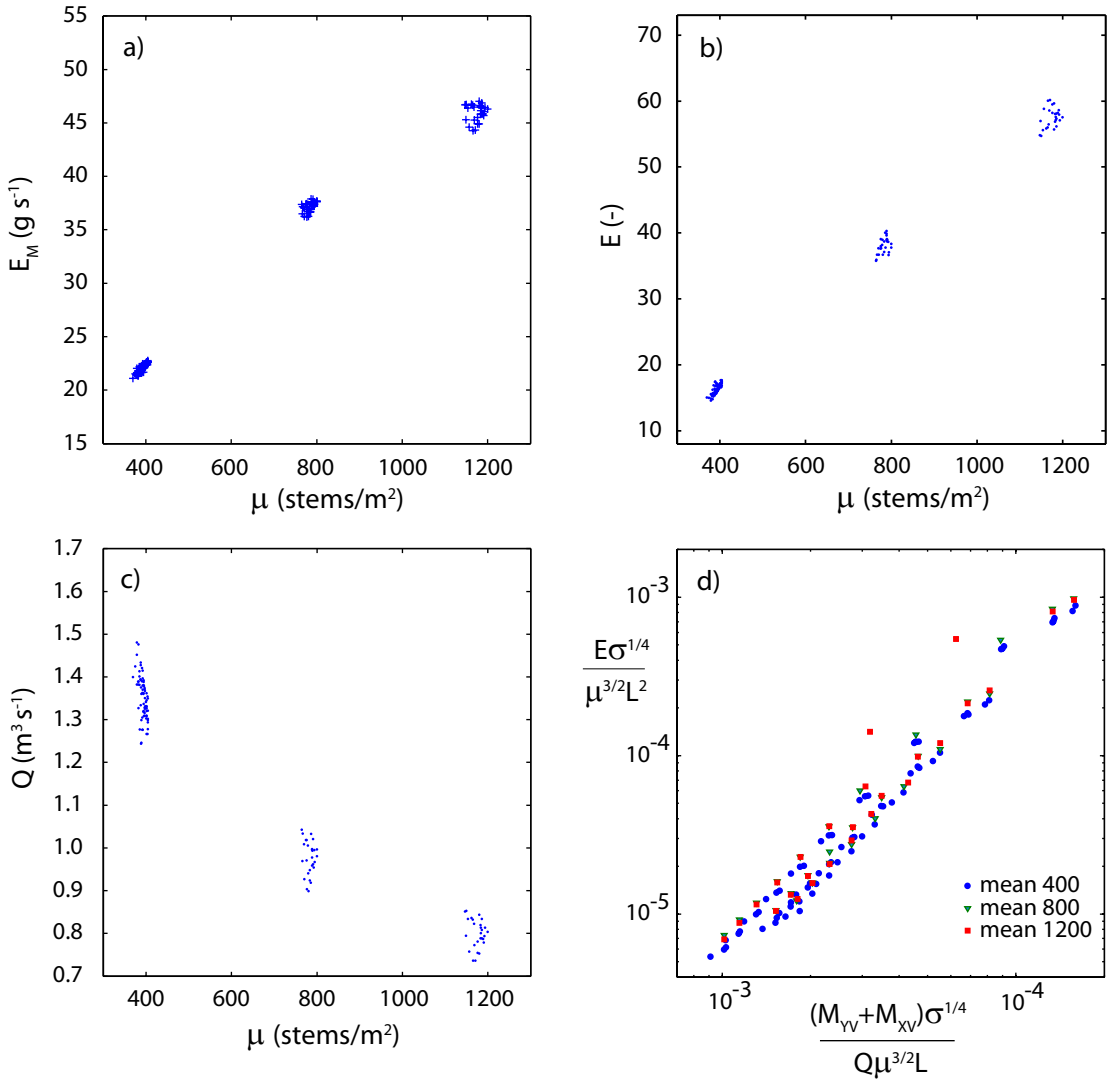

Figure 5.3. System variables as a function of the mean density a), b), c) and correlation of the system variable and statistical parameter of the random distribution written in a non-dimensional way.

dimensional quantities suggests the presence of a relationship between system parameter that will be analyzed more deeply in the next future.

5.5 Conclusion

A first attempt to identify a proper mean, variance and length scale of a randomly distributed vegetation which assures the best overall efficiency has been made in this work. Efficiency can be expressed in terms of mass and in terms of concentration in relation to the wetland management requirements. Present regulations and design principles focus their attention only on a removal efficiency written as a function of concentration difference between the inlet and the outlet sections but a more comprehensive evaluation should be done considering also the total amount of removed mass. A good correlation between statistical parameters, removal efficiency and discharge suggest that the problem can be parametrized with the principal statistical parameters of the random vegetation density distribution. The role of the parameter $M_{yv} + M_{xv}$, that describes the position of the thicker vegetated areas in relation to the inlet and the outlet sections could be important to predict the wetland efficiency, but a more comprehensive analysis is needed to confirm performed.

Notation

The symbols and notation appearing in this thesis are listed below. Within the main body of the text, symbols are usually defined at their first usage within a chapter, or at other times when needed for clarity. In some cases equations have been presented using the same notation used in the original papers; in other cases, original notation has been altered to better fit with the surrounding material.

Acronyms

ADE	Advection-Dispersion Equation;
BTC	Breakthrough Curve;
DOC	Dissolved Organic Carbon
DON	Dissolved Organic Nitrogen
EA	Evolutionary Algorithm;
LVZ	Lateral Vegetated Zone;
MFC	Main Flow Channel;
MIMD	Multiple Instruction Multiple Data.
PDF	Probability Density Function;
RMSE	Root Mean Square Error;
RTD	Residence Time Distribution;
RWT	Rodhamine-WT;

STIR Solute Transport In Rivers;

TSM Transient Storage Model;

Roman symbols

Upper case

A average stream cross-sectional area [L^2];

B wetland width [L];

B_r river width [L];

C concentration [ML^{-3}];

C^* dimensionless concentration, $C^* = C/C_{\max}$ [-];

C_{obs} observed concentration [ML^{-3}];

C_{sim} simulated concentration [ML^{-3}];

$C_{\max}$ peak concentration of BTCs [ML^{-3}];

$\overline{C}_{in}$ constant concentration at the inlet section of the wetland [ML^{-3}];

C_{out} concentration at the outlet section of the wetland [ML^{-3}];

C_δ concentration resulting from a mass pulse [ML^{-3}];

D_m molecular diffusion coefficient [L^2T^{-1}];

D_{ij} components of the turbulent diffusion tensor [L^2T^{-1}];

D_z vertical turbulent diffusivity [L^2T^{-1}];

E removal efficiency [-];

E_{ij} components of the dispersion tensor [L^2T^{-1}];

E_L longitudinal dispersion coefficient in a canopy [L^2T^{-1}];

E_M mass removal efficiency [MT^{-1}];

E_T transversal dispersion coefficient in a canopy [L^2T^{-1}];

F_A exchange flux across the surface [$ML^{-2}T^{-1}$];

F_B exchange flux across the river bed [$ML^{-2}T^{-1}$];

H mean water depth over the wetland domain [L];

I set of observed concentration values, $I = I_U \cup I_L$;

I_L set of observed concentration values lower than a given threshold concentration;

I_U set of observed concentration values higher than a given threshold concentration;

K longitudinal dispersion coefficient for a 1D model [$L^2 T^{-1}$];

K_i MFC and LVZ longitudinal dispersion coefficients of the STIR-DTD model [$L^2 T^{-1}$];

L length of study reach [L];

L_h horizontal size of the recirculation zones [L];

M_0 injected mass [M];

$\dot{M}_{in}$ mass flux entering the wetland [$M T^{-1}$];

$\dot{M}_{out}$ mass flux exiting the wetland [$M T^{-1}$];

M_{iv} first velocity-weighted moment of the density field around the x, y directions [T^{-1}];

P wetted perimeter [L];

Q flow discharge [$L^3 T^{-1}$];

$\overline{Q}$ flow discharge passing through a wetland under stationary conditions [$L^3 T^{-1}$];

Q_i flow discharge passing MFC and LVZs [$L^3 T^{-1}$];

S source/sink term [$M L^{-1} T^{-1}$];

T_a timescale for the time-averaging procedure [T];

T_i timescales for retention processes [T];

$T_i j$ turbulent shear stresses [$M L^{-1} T^{-2}$];

U depth-averaged flow velocity along x direction [$L T^{-1}$];

V depth-averaged flow velocity along y direction [$L T^{-1}$].

Lower case

a frontal vegetation area per unit volume [L^{-1}]

b wetland inlet/outlet width [L];

b^* non dimensional inlet ratio [-];

c local instantaneous concentration [ML^{-3}];

$\widetilde{c}$ time average of the local instantaneous concentration [ML^{-3}];

c_D^i drag coefficients due to vegetation and bottom drag [-];

c_f coefficient of friction in the 2D depth averaged equations [-];

d stem diameter [L];

f Manning's roughness coefficient [$TL^{-1/3}$];

f_{eq} Manning's roughness coefficient equivalent to bed and vegetative resistance [$TL^{-1/3}$];

g gravity acceleration [LT^{-2}];

h water depth [L];

$i_x\, i_y$ bed slopes along the x and y directions [-];

k' decay rate [LT^{-1}];

k decay coefficient [T^{-1}];

k_{dv} dilatational viscosity [$ML^{-1}T^{-1}$];

l submerged stem length [L];

l_c corelation length of the spatial random vegetation density field [L];

m_b slope coefficient [-];

n vegetation density [L^{-2}];

n^* non dimensional density ratio [-];

p pressure [$ML^{-1}T^{-2}$];

p_i conditional probability distribution of the random variable $\mathcal{N}_i$ [-];

r overall residence time distribution within a stream of length x [T^{-1}];

r_i probability density function (PDF) of the generic residence time [T^{-1}];

r_M mass recovery ratio [-];

r_W probability density function (PDF) of the residence time the surface water, $\mathcal{T}_W$ [T^{-1}];

r_S probability density function (PDF) of the overall residence time in the storage zones, $\mathcal{T}_S$ [T^{-1}];

r_{S_i} probability density function (PDF) of the overall residence time in the i-th storage domain, $\mathcal{T}_{Si}$ [T^{-1}];

$r_{S_i|n}$ conditional residence time probability density function (PDF) in the i-th storage domain given that a particle has entered the storage domain n times [T^{-1}];

t time [T];

$\overline{t}$ averaging timescale [T];

t^* dimensionless time [-];

t_{ad} average advection time, $t_{\mathrm{ad}} = L/U$ [T];

$\mathbf{u}$ velocity vector, $\mathbf{u} = (u, v, w)$ [$\mathrm{L\,T}^{-1}$];

u velocity component in the x-direction [$\mathrm{L\,T}^{-1}$];

$\widetilde{u}$ time average velocity component in the x-direction [$\mathrm{L\,T}^{-1}$];

$\widetilde{\mathbf{u}}$ time average of velocity field, $\widetilde{\mathbf{u}} = (\widetilde{u}, \widetilde{v}, \widetilde{w})$ [$\mathrm{L\,T}^{-1}$];

u_* shear velocity [$\mathrm{L\,T}^{-1}$];

v velocity component in the y-direction [$\mathrm{L\,T}^{-1}$];

$\widetilde{v}$ time average of the velocity component in the y-direction [$\mathrm{L\,T}^{-1}$];

w velocity component in the z-direction [$\mathrm{L\,T}^{-1}$];

$\widetilde{w}$ time average of the velocity component in the z-direction [$\mathrm{L\,T}^{-1}$];

w_1 weight of the STIR-DTD model [-];

$\mathbf{x}$ position vector, $\mathbf{x} = (x, y, z)$ [L];

x spatial coordinate [L];

y spatial coordinate [L];

z spatial coordinate [L];

z_s water surface elevation [L];

Calligraphic symbols

$\mathcal{N}_i$ number of times a particle enters the i-th storage domain (random variable) [-];

$\mathcal{T}$ total residence time in the study reach (random variable) [T];

$\mathcal{T}_S$ overall residence time in the storage zones (random variable) [T];

$\mathcal{T}_{Si}$ overall residence time in the i-th storage domain (random variable) [T];

$\mathcal{T}_W$ residence time in the surface water (random variable) [T].

Greek symbols

Upper case

Δt_{inj} time length of injection period [T];

Δy transversal motion of a particle passing through a canopy [L];

Γ velocity shape factor [-];

$\mathbf{\Phi}$ mass flux of solute [$\mathrm{M\,L^{-2}\,T^{-1}}$];

Φ cumulative distribution function of the wetland RTD [-];

Lower case

$\alpha\,\alpha_i$ transfer rates [$\mathrm{T^{-1}}$];

α_T coefficient for the transverse diffusivity [-];

β scale factor for the transverse motion of a particle in a canopy [-];

λ number of genetic operators used EA [-];

χ general variable used for the time-averaging procedure;

$\widetilde{\chi}$ general time-averaged variable;

χ' fluctuation of the general variable around the time-averaged value;

μ mean vegetation density of the random field [$\mathrm{L^{-2}}$];

μ_i number of individuals of the initial generation used by EA [-];

ν kinematic viscosity [$\mathrm{L^2\,T^{-1}}$];

ν_t turbulent viscosity coefficient $[\mathrm{L}^2\,\mathrm{T}^{-1}]$;

η dynamic viscosity $[\mathrm{M}\,\mathrm{L}^{-1}\,\mathrm{T}^{-1}]$;

φ_i probability density function (PDF) of the residence time in the i-th storage domain $[\mathrm{T}^{-1}]$;

σ variance of the density random field from the mean density value $[\mathrm{L}^{-4}]$;

ρ water density $[\mathrm{M}\,\mathrm{L}^{-3}]$

τ_i^j shear stresses due to bottom and vegetation resistance $[\mathrm{M}\,\mathrm{L}^{-1}\,\mathrm{T}^{-2}]$;

Ringraziamenti

Il contenuto di questo lavoro é stato sviluppato nell'ambito del progetto di ricerca **"Processi di trasporto e criteri ottimali di progettazione delle aree umide"** finanziato dalla **Fondazione Cassa di Risparmio di Padova e Rovigo** nell'ambito del programma "Progetto Dottorati di Ricerca 2009". Si ringrazia la Fondazione per il sostegno e la professionaltà dimostrati in questi tre anni di lavoro e formazione alla ricerca.

Vorrei ringraziare innanzitutto il mio docente tutore, Prof. Andrea Marion, per avermi dato l'opportunità di conoscere e sperimentare in autonomia l' ambiente della ricerca e il mio correlatore, ing. Andrea Bottacin Busolin, per il fondamentale stimolo datomi nello sviluppo di molte delle idee che sono contenute in questa tesi. Vorrei ringraziare il dott. Luca Palmeri e la dott.ssa Comis per avermi ospitato e accolto nel loro gruppo di ricerca così ispirato e i colleghi del Politecnico di Torino, ing. Alberto Tonda, ing. Giovanni Squillero e ing. Marco Gaudesi per aver percorso con me strade nuove nel panorama della ricerca sugli algoritmi evolutivi.

Vorrei ringraziare poi chi mi ha affiancato tutti i giorni nella mia attività di ricerca, condividendo con me i momenti di gioia e quelli di frustrazione che talvolta si sono verificati: un ringraziamento particolare a Marco Bonato per i suoi racconti africani, a Marco Carrer per il suo accento veneziano, a Paola per le

sue riflessioni su ciò che davvero conta, a Leonardo per il punto di vista sempre alternativo sulla vita, ad Alberto Pittarello per la foto d'addio, ad Alice per i cioccolatini che non mancano mai, ad Alberto Barausse per lo sguardo incantato sulla natura veneta, a Dario per il suo amore contagioso per la laguna, a Luca per la sua dedizione nel lavoro e a Matteo per la sua amicizia.

Ai miei genitori, ai miei fratelli, ai miei amici e familiari va un intimo riconoscimento che preferisco non esprimere in queste poche righe. A loro devo la persona che sono oggi e a loro dedico non la mia vita passata, ma quella che avrò occasione di costruire, con un pizzico di fortuna e molta dedizione, nei giorni a venire.

Tommaso Musner

Bibliography

Akratos, C., and V. Tsihrintzis (2007), Effect of temperature, HRT, vegetation and porous media on removal efficiency of pilot-scale horizontal subsurface flow constructed wetlands, *Ecological Engineering*, *29*(2), 173–191.

Arega, F., and B. F. Sanders (2004), Dispersion model for tidal wetlands, *Journal of Hydraulic Engineering*, *130*(8), 739–754.

Augustijn, D., F. Huthoff, and E. Velzen (2006), Comparison of vegetation roughness descriptions.

Babarutsi, S., J. Ganoulis, and V. H. Chu (1989), Experimental investigation of shallow recirculating flows, *Journal of Hydraulic Engineering*, *115*(7), 906–924.

Bellin, A., and Y. Rubin (1996), HYDRO_GEN: a spatially distributed random field generator for correlated properties, *Stochastic Hydrology and Hydraulics*, *10*(4), 253–278.

Bencala, K. E., and R. A. Walters (1983), Simulation of solute transport in a mountain pool-and-riffle stream: A transient storage model, *Water Resour. Res.*, *19*(3), 718–724.

Bendoricchio, G., and S. E. Jorgensen (Eds.) (2001), *Fundamentals of Ecological Modelling, Third Edition*, 3 ed., Elsevier Science.

Bennett, C. O., and J. E. Myers (1962), *Momentum, heat, and mass transfer*, McGraw-Hill New York.

Blevins, R. D. (2005), Forces on and stability of a cylinder in a wake, *Journal of Offshore Mechanics*, *127*, 39–45.

Boano, F., A. I. Packman, A. Cortis, R. Revelli, and L. Ridolfi (2007), A continuous time random walk approach to the stream transport of solutes, *Water Resour. Res.*, *43*, W10,425.

Bottacin Busolin, A. (2010), Transport of solutes in streams with transient storage and hyporheic exchange, Ph.D. diss., Dept. of Civil and Environ. Eng., University of Padova, Padova (Italy).

Bottacin-Busolin, A., and A. Marion (2010), Combined role of advective pumping and mechanical dispersion on time scales of bed form–induced hyporheic exchange, *Water resources research*, *46*(8), W08,518.

Bottacin-Busolin, A., G. Singer, M. Zaramella, T. J. Battin, and A. Marion (2009), Effects of streambed morphology and biofilm growth on the transient storage of solutes, *Environmental science & technology*, *43*(19), 7337–7342.

Cowardin, L. M. (1979), *Classification of Wetlands and Deepwater Habitats of the United States*, DIANE Publishing.

Day, T. J. (1975), Longitudinal dispersion in natural channels, *Water Resour. Res.*

Deng, Z.-Q., L. Bengtsson, and V. P. Singh (2006), Parameter estimation for fractional dispersion model for rivers, *Environ. Fluid. Mech.*, *6*(5), 451–475.

Elder, J. W. (1959), The dispersion of marked fluid in turbulent shear flow, *J. Fluid. Mech.*, *5*(04), 544–560.

Elliott, A. H., and N. H. Brooks (1997a), Transfer of nonsorbing solutes to a streambed with bed forms: Theory, *Water Resour. Res.*, *33*(1), 123–136.

Elliott, A. H., and N. H. Brooks (1997b), Transfer of nonsorbing solutes to a streambed with bed forms: Laboratory experiments, *Water Resour. Res.*, *33*(1), 137–151.

Ergun, S. (1952), Fluid flow through packed columns, *Chem. Eng. Prog.*, *48*, 89–94.

Fick, A. (1855), *Annln. Phys.*, *170*, 59.

Fischer, H. B. (1975), Discussion of "Simple method for predicting dispersion in streams", *J. Env. Eng. Div., ASCE*, *101*(3), 435–455.

Fischer, H. B., J. E. List, C. R. Koh, J. Imberger, and N. H. Brooks (1979), *Mixing in Inland and Coastal Waters*, Academic Press.

Fogel, L. J. (1962), Autonomous automata, *Industrial Research*, *4*, 14–19.

Galland, J. C., N. Goutal, and J. M. Hervouet (1991), TELEMAC: a new numerical model for solving shallow water equations, *Advances in Water Resources AWREDI,*, *14*(3).

Gooseff, M. N., S. M. Wondzell, R. Haggerty, and J. Anderson (2003), Comparing transient storage modeling and residence time distribution (RTD) analysis in geomorphically varied reaches in the lookout creek basin, oregon, USA, *Adv. Water. Resour.*, *26*(9), 925–937.

Gooseff, M. N., R. O. H. Jr., and J. L. Tank (2007), Relating transient storage to channel complexity in streams of varying land use in jackson hole, wyoming, *Water Resour. Res.*, *43*, W01,417.

Green, J., and J. Garton (1983), Vegetation lined channel design procedures, *Transactions of the American Society of Agricultural Engineers*, *26*(2), 437–439.

Haberl, R., R. Perfler, and H. Mayer (1995), Constructed wetlands in europe, *Water Science and Technology*, *32*(3), 305–316.

Haggerty, R., and S. M. Wondzell (2002), Power-law residence time distribution in the hyporheic zone of a 2nd-order mountain stream, *Geophys. Res. Lett.*, *29*(13), 1640.

Haggerty, R., S. A. McKenna, and L. C. Meigs (2000), On the late-time behavior of tracer test breakthrough curves, *Water Resour. Res.*, *36*(12), 3467–3479.

Hall, B. R., and G. E. Freeman (1994), Study of hydraulic roughness in wetland vegetation takes new look at manning's n, *US Army Corps of Engineers Waterways Experiment Station, Wetlands Research Program Bulletin*, *4*, 1–4.

Hart, D. R. (1995), Parameter estimation and stochastic interpretation of the transient storage model for solute transport in streams, *Water Resour. Res.*, *31*(2), 323–328.

Hervouet, J. M., J. L. Hubert, J. M. Janin, F. Lepeintre, and E. Peltier (1994), The computation of free surface flows with TELEMAC: an example of evolution towards hydroinformatics, *Journal of Hydraulic Research*, *32*(S1), 45–64.

Hill, R. J., D. L. Koch, and A. J. C. Ladd (2001), Moderate-reynolds-number flows in ordered and random arrays of spheres, *Journal of Fluid Mechanics*, *448*(2), 243–278.

Hocking, P. (1989), Seasonal dynamics of production, and nutrient accumulation and cycling by phragmites australis (Cav.) trin. ex stuedel in a nutrient-enriched swamp in inland australia. i. whole plants, *Marine and Freshwater Research*, *40*(5), 421–444.

Holland, J. H. (1992), *Adaptation in natural and artificial systems*, MIT Press, Cambridge, MA, USA.

Jenkins, G. A., and M. Greenway (2005), The hydraulic efficiency of fringing versus banded vegetation in constructed wetlands, *25*(1), 61–72.

Kadlec, R., and S. Wallace (2009), *Treatment wetlands*, CRC.

Kadlec, R. H. (1990), Overland flow in wetlands: vegetation resistance, *Journal of Hydraulic Engineering*, *116*(5), 691–706.

Kadlec, R. H. (2000), The inadequacy of first-order treatment wetland models, *Ecological Engineering*, *15*(1), 105–119.

Keefe, S. H., L. B. Barber, R. L. Runkel, J. N. Ryan, D. M. McKnight, and R. D. Wass (2004), Conservative and reactive solute transport in constructed wetlands, *Water Resour. Res.*, *40*(1), W01,201.

Koza, J. (1992), *Genetic Programming: On the Programming of Computers by Means of Natural Selection*, MIT Press.

Krenkel, P. A., and G. T. Orlob (1962), Turbulent diffusion and the reaereation coefficient, *J. Sanit. Eng. Div., ASCE*, *88*(SA2), 3079.

Lightbody, A. F., and H. M. Nepf (2006), Prediction of velocity profiles and longitudinal dispersion in emergent salt marsh vegetation, *Limnology and Oceanography*, pp. 218–228.

Marion, A., and M. Zaramella (2005), A residence time model for stream-subsurface exchange of contaminants, *Acta Geophysica Polonica*, *53*(4), 527.

Marion, A., M. Zaramella, and A. Bottacin-Busolin (2008), Solute transport in rivers with multiple storage zones: The STIR model, *Water Resour. Res.*, *44*, W10,406.

Martinez, C. J., and W. R. Wise (2003), Analysis of constructed treatment wetland hydraulics with the transient storage model OTIS, *Ecological Engineering*, *20*(3), 211–222.

Nepf, H. M. (1999), Drag, turbulence, and diffusion in flow through emergent vegetation, *Water resources research*, *35*(2), 479–489.

Nepf, H. M., J. A. Sullivan, and R. A. Zavistoski (1997), A model for diffusion within emergent vegetation, *Limnology and Oceanography*, pp. 1735–1745.

Nordin, C. F., and G. V. Sabol (1974), Empirical data on longitudinal dispersion in rivers, *U.S. Geological Survey*, pp. 20–74.

Nordin, C. F., and B. M. Troutman (1980), Longitudinal dispersion in rivers: The persistence of skewness in observed data, *Water Resour. Res.*

Parr, T. W. (1990), *Factors affecting reed (Phragmites australis) growth in UK reed bed treatment systems*, vol. 67, Pergamon Press, Oxford, UK.

Persson, J., N. Somes, and T. Wong (1999), Hydraulics efficiency of constructed wetlands and ponds, *Water Science & Technology*, *40*(3), 291–300.

Perucca, E., C. Camporeale, and L. Ridolfi (2009), Estimation of the dispersion coefficient in rivers with riparian vegetation, *Advances in Water Resources*, *32*(1), 78–87.

Petryk, S. (1969), Drag on cylinders in open channel flow, Ph.D. thesis, Colorado State University.

Raupach, M. R. (1992), Drag and drag partition on rough surfaces, *Boundary-Layer Meteorology*, *60*(4), 375–395.

Runkel, R. L. (1998), One-dimensional Transport with Inflow ans Storage (OTIS): A solute transport model of streams and rivers, *US Geol. Surv. Water Resour. Invest. Rep.*, pp. 98–4018.

Runkel, R. L., and R. E. Broshears (1991), *One-dimensional transport with inflow and storage (OTIS): A solute transport model for small streams*, CADSWES, Center for Advanced Decision Support for Water and Environmental Systems, Department of Civil Engineering, University of Colorado.

Sanchez, E., M. Schillaci, and G. Squillero (2011), *Evolutionary Optimization: the μGP toolkit*, 1st ed., 250 pp., Springer.

Sanchez, E., G. Squillero, and A. Tonda (2012), *Industrial Applications of Evolutionary Algorithms*, *Intelligent Systems Reference Library*, vol. 34, 114 pp., Springer.

Schwefel, H.-P. (1965), *Cybernetic Evolution as Strategy for Experimental Research in Fluid Mechanics (Diploma Thesis in German)*, Hermann Föttinger-Institute for Fluid Mechanics, Technical University of Berlin.

Somes, N. L., W. A. Bishop, and T. H. Wong (1999), Numerical simulation of wetland hydrodynamics, *Environment International*, *25*(6–7), 773–779.

Storn, R., and K. Price (1997), Differential evolution – a simple and efficient heuristic for global optimization over continuous spaces, *J. Global Optim.*, *11*, 341–359.

Tange, O. (2011), Gnu parallel - the command-line power tool, *;login: The USENIX Magazine*, *February 2011*, 42–47.

Tanino, Y., and H. Nepf (2008), Laboratory investigation of mean drag in a random array of rigid, emergent cylinders, *Journal of Hydraulic Engineering*, *134*(1), 34–41.

Tanner, C. (2001), Growth and nutrient dynamics of soft-stem bulrush in constructed wetlands treating nutrient-rich wastewaters, *Wetlands Ecology and Management*, *9*(1), 49–73.

Thackston, E. L., and K. B. J. Schnelle (1970), Predicting effects of dead zones on stream mixing, *J. Sanit. Eng. Div., ASCE*, *92*(2), 319–331.

Tritton, D. J. (1959), Experiments on the flow past a circular cylinder at low reynolds numbers, *J. Fluid Mech*, *6*(4), 547–567.

White, B., and H. Nepf (2003), Scalar transport in random cylinder arrays at moderate reynolds number, *Journal of Fluid Mechanics*, *487*(25), 43–79.

White, F. M. (1991), *Viscous fluid flow*, McGraw-Hill.

Wieselberger, C. (1921), Neuere feststellungen Über die gesetze des flüssigkeits luftwiderstands, *Physicalische Zeitschrift*, *22*, 321–328.

Wörman, A., and V. Kronnäs (2005), Effect of pond shape and vegetation heterogeneity on flow and treatment performance of constructed wetlands, *Journal of Hydrology*, *301*(1-4), 123–138.

Wörman, A., A. I. Packman, H. Johansson, and K. Jonsson (2002), Effect of flow-induced exchange in hyporheic zones on longitudinal transport of solutes in streams and rivers, *Water Resour. Res.*, *38*(1), 1001.

Wu, W. (2007), *Computational river dynamics*, CRC.

Yu, T., L. Davis, C. M. Baydar, and R. Roy (Eds.) (2008), *Evolutionary Computation in Practice*, *Studies in Computational Intelligence*, vol. 88, Springer.